THE EFFECTS OF SURFACE AGING ON NANOPARTICLE FATE AND TRANSPORT IN NATURAL AND ENGINEERED POROUS MEDIA

Dissertation

Submitted by Anjuliee M. Mittelman

In partial fulfillment of the requirements for the degree of

Doctor of Philosophy

in

Civil and Environmental Engineering

TUFTS UNIVERSITY

May 2015

DISSERTATION COMMITTEE:

Professor Kurt Pennell, Adviser (*Tufts University)*
Professor Linda Abriola (*Tufts University)*
Assistant Professor John Fortner (*Washington University of St. Louis)*
Assistant Professor Daniele Lantagne (*Tufts University)*
Associate Professor Douglas Matson (*Tufts University*)

ABSTRACT

Nanomaterials will be subjected to various surface transformations in the environment and within water and wastewater treatment systems. A comprehensive understanding of the fate and transport behavior of "aged" nanomaterials in both natural and engineered porous media is required in order to accurately quantify ecological and human health risks. This research sought to (1) evaluate the impact of ultraviolet (UV) light aging on nanoparticle transport in water-saturated porous media; and (2) assess the effects of influent water quality on silver nanoparticle retention and dissolution in ceramic water filters. Additionally, the value of quartz crystal microbalance (QCM-D) data in nanoparticle fate and transport studies was evaluated by comparing deposition behavior in complementary QCM-D and sand columns experiments. Silver (nAg) and iron oxide nanoparticles exposed to UV light were up to 50% more strongly retained in porous media compared with freshly prepared suspensions due to less negative surface charge and larger aggregate sizes. UV-aged nAg were more prone to dissolution in sand columns, resulting in effluent Ag^{+} concentrations as high as 1.2 mg/L. In ceramic water filters, dissolution and cation exchange processes controlled silver release into treated water. The use of acidic, high salinity, or high hardness water accelerated oxidative dissolution of the silver coating and resulted in effluent silver concentrations 5-10 times above international drinking water guidelines. Results support the recommendation for a regular filter replacement or silver re-application schedule to ensure ongoing efficacy. Taken in concert, these research findings suggest that oxidative aging of

nanomaterial surfaces (either through exposure to UV light or aggressive water chemistries) will alter the fate of nanomaterials in the environment and may decrease the effective lifetime of devices which utilize nanotechnology. Corresponding QCM-D and column experiments revealed that nanoparticles were generally more mobile in QCM-D due to reduced diffusive transport of larger aggregates to the sensor surface and high primary energy barriers to deposition. While QCM-D may be used to provide qualitative data, direct comparisons of deposition rates in QCM-D with attachment rates obtained from column experiments may prove difficult due to differences in flow geometry and surface characteristics between the two systems.

ACKNOWLEDGEMENTS

I would first like to express my gratitude to my adviser, Dr. Kurt Pennell, for his mentorship and guidance. There were a few moments when I questioned continuing my PhD, and I am grateful for his patience and support over these past few years. It really has been a gift to work under him at Tufts and I hope that this relationship will continue as I start my professional career. I am also thankful for the opportunity to work with Dr. Linda Abriola and learn from her wealth of knowledge. She has served as an invaluable role model during my time at Tufts. Thank you also to my other committee members, Dr. Daniele Lantagne and Dr. Douglas Matson for supporting my interests in public health, and Dr. John Fortner for his always-helpful advice, especially regarding experimental methods.

I would also like to thank Dr. Yonggang Wang for his support in the lab during my first few years at Tufts. My research would not have been possible without his groundwork and help with various analytical and experimental techniques. Thanks are also due to Dr. Amir Taghavy and Matthew Becker for their patience in modeling my sometime very difficult-to model experimental data, and to Wenlu Li for his efforts in running QCM experiments. Thank you also to Tyler Marcet, who has been a great friend through my entire time at Tufts (and always available to help calm my frustrations over tools and Swagelok fittings).

I am infinitely grateful to my parents for their constant support and advice. They inspired me to pursue a career in science and engineering and are always more than happy to talk through different research approaches and career goals. Special

thanks to my dad for reassuring me that I would not regret staying on for a PhD and to my mom for her regular calls to make sure that I was sleeping and eating enough of her Indian food.

Lastly, thank you to my wonderful network of family and friends across the U.S. and Canada. Their cross-country visits, phone calls, and texts never failed to put a smile on my face and keep my spirits up.

TABLE OF CONTENTS

LIST OF FIGURES

LIST OF TABLES

THE EFFECTS OF SURFACE AGING ON THE FATE AND TRANSPORT OF NANOMATERIALS IN NATURAL AND ENGINEERED POROUS MEDIA

CHAPTER 1: INTRODUCTION

Nanomaterials, defined as materials having at least one dimension in the range of 1 to 100 nm, possess unique chemical, optical, mechanical, magnetic, and electrical properties compared to their parent materials. For example, nano-scale silver is highly antimicrobial, displays improved electrical conductivity, and has distinctive optical properties when compared with bulk silver metal. The nanotechnology industry has seen rapid growth over the past two decades, and nanotechnology-enabled products are expected to exceed $3 trillion globally by 2018 (Lux Research 2014). While nanotechnologies hold great promise in fields such as cancer research and clean energy, the potential impacts of nanoscale materials on public health and the environment have not yet been fully characterized. Unintentional release of nanomaterials may occur throughout a product's lifecycle, including at the manufacturing, transport, use, and disposal stages (Mueller and Nowack 2008), raising concerns related to environmental fate, transport, and toxicity. Due to their high reactivity, small size, and large surface area, most nanomaterials in large scale production have demonstrated toxicity against soil microorganisms, mammalian cells, laboratory animals, and aquatic life (e.g., Choi et al. 2008; Navarro et al. 2008).

The probability that bare nanoparticles will be released into the environment is very low, as most nanoparticles are coated with inorganic or organic stabilizers to protect the core material from degradation and increase stability in aqueous suspensions (Labille et al. 2010). For example, titanium dioxide nanoparticles are

often coated with a thick layer of alumina or silica to control ultra-violet (UV) light reactivity and an amphiphilic polymer layer to improve dispersability, while silver nanoparticles are often stabilized with citrate or poly-vinylpyrrolidone. Engineered nanomaterials will be subjected to various transformations in aqueous environments, such as photodegradation, passivation by natural organic matter, biodegradation, and oxidation (Lin et al. 2010). The "aging" of particle surfaces or coatings through these processes could have important implications on nanomaterial fate and transport in the natural environment and in products and devices that utilize nanotechnology, including water filters, clothing, and food packaging. Breakdown of the protective coatings can also lead to the release of toxic byproducts, such as dissolved metal ions and reactive oxygen species (ROS) (Auffan et al. 2010).

Nanomaterial behavior in natural and engineered systems, particularly the fate and transport of aged nanomaterials, remains poorly understood. The transport of nanomaterials and nanomaterial residues is of interest due to both the potential for groundwater contamination and the need to better understand the performance of filters in water and wastewater treatment processes (Solovitch et al. 2010). Most prior transport studies with nanomaterials have utilized freshly prepared suspensions that fail to capture realistic aging processes that may occur in the environment. The effects of specific aging processes (e.g., exposure to UV light) on nanoparticle deposition behavior have not been previously explored. In addition, a more thorough understanding of nanomaterial aging in consumer and household products will allow for more accurate predictions of product lifetime.

For example, the fate of silver nanoparticles in ceramic water filters and the specific mechanisms responsible for silver release have received limited attention, despite obvious consequences on user safety and filter disinfection efficacy.

Nanoparticle mobility and deposition in the environment are traditionally evaluated through one-dimensional column studies. Recently, quartz crystal microbalance with dissipation (QCM-D) has been used to provide qualitative or relative comparisons of nanoparticle affinity for different surfaces (e.g., silicon dioxide, aluminosilicates) across a range of chemical conditions. Although QCM-D may provide a relatively rapid and cost-effective screening tool to assess nanoparticle deposition behavior prior to running more costly and time-intensive column studies, QCM-D data have not yet been related to attachment parameters derived from traditional column transport experiments. A more complete understanding flow geometry and surface area available for deposition in the two systems is necessary in order to establish the significance of QCM-D data.

The primary aim of this Ph.D. research was to assess the fate and transport behavior of metal and metal oxide nanomaterials (iron oxide and silver) in natural and engineered porous media systems following exposure to various aging scenarios. This thesis begins with a literature review (Chapter 2) which covers nanomaterial properties and applications, colloid-surface interactions, clean-bed filtration theory, nanomaterial aging and toxicity, and the role of silver and ceramic filters in point-of-use water treatment. Details of materials, experimental methods, and analytical techniques are provided in Chapter 3. Experimental results for specific research objectives are presented in Chapters 4-7 and

conclusions and recommendations for future research are provided in Chapter 8. The specific objectives of this research were to:

A. Investigate the effects of UV light exposure on silver nanoparticle fate and transport in water-saturated porous media. Citrate-coated silver nanoparticles (nAg) were exposed to UV light for up to 7 days and monitored for changes in aggregation kinetics, surface charge, surface chemistry, and dissolution kinetics. The transport, retention, and dissolution of fresh and 3-day UV-aged nAg were evaluated in columns packed with washed 40-50 mesh Ottawa sand as a function of ionic strength (10 and 20 mM $NaNO_3$) and flow rate (1.0, 1.5, and 2.0 mL/min) (Chapter 4).
B. Evaluate the impact of UV light aging on iron oxide nanoparticle (nMag) fate and transport in water-saturated porous media. Fresh and 3-day UV-aged nMag were introduced into columns packed with washed 40-50 mesh Ottawa sand or glass beads. Experiments were conducted with background electrolytes of NaCl (20 or 200 mM) or $CaCl_2$ (2 mM) at a flow rate of 1 mL/min (Chapter 5).
C. Evaluate the influence of dissolution, nanoparticle detachment, and cation exchange on silver release in ceramic water filters and determine the effective lifetime of the nAg coating following exposure to various water chemistries. Ceramic disks were painted with 0.03 mg Ag/g of casein-coated nAg or $AgNO_3$ and exposed to influent waters that possessed different pH (5, 7, 9), ionic strength (1, 10, 50 mM), and cation species (Na^+, Ca^{2+}, Mg^{2+}). The cation exchange capacity (CEC) of the ceramic was investigated through

Ca-Mg and Ag-Mg exchange experiments with crushed ceramic material and intact filter disks (Chapter 6).

D. Compare nanoparticle deposition behavior in QCM-D and sand columns and relate QCM-D deposition rates to fitted column attachment parameters. Corresponding QCM-D and sand column experiments were conducted under identical chemical conditions and linear velocities with three different nanoparticles: silver, iron oxide, and fullerene. The flow conditions and surface area available for nanoparticle deposition in the QCM system were estimated and used to derive scaling factors to predict attachment rates in porous media as a function of ionic strength, pH, and flow rate (Chapter 7).

CHAPTER 2: LITERATURE REVIEW

Nanomaterial Behavior in the Environment

Nanomaterial Applications and Toxicity

Silver, iron oxide, and carbon-based nanomaterials are among the most widely used nanomaterials in consumer and medical products. Silver nanoparticles (nAg) are commonly used in industrial, healthcare and commercial applications for their broad-spectrum antimicrobial properties. Biocidal nAg has been incorporated into a variety of products including paint, food packaging, cosmetics, medical devices, water filters, and socks. Both the particulate (nAg) and dissolved ion (Ag^+) have demonstrated unique bactericidal effects, necessitating a thorough understanding of nAg oxidative aging in consumer products and in the environment. Toxicity of nAg has been attributed to the pitting action of the small particles on cell membranes (Navarro et al. 2008) and silver ions disrupting cellular metabolism (Morones-Ramirez et al. 2013). Transmission electron microscopy (TEM) and scanning electron microscopy (SEM) images of bacterial cells treated with 5-10 mg/L of nAg show evidence of pitting, incorporation of nAg within the cytoplasm and leaking of intracellular substances. The silver ion has been shown to depress the activity of cytoplasmic membrane enzymes, leading to structural damage and inhibition of cellular respiration (Sondi and Salopak-Sondi 2004; Li et al. 2010). Specifically, Ag^+ is thought to bind to respiratory chain enzymes and interfere with the passage of electrons along the electron transport chain, leading to production of large quantities of ROS. These events render the cytoplasmic

membrane more permeable to protons and collapse the proton-pump machinery vital for energy production and membrane transport in the cell (Holt and Bard 2005).

Nano-sized iron oxides are another widely produced nanomaterial due to their ubiquitous applications in catalysis, magnetic data storage, biomedical imaging, targeted drug delivery, and medical diagnostics and therapy (Lu et al. 2007; Sahoo et al. 2003; Gupta and Gupta 2005). Iron oxide nanoparticles possess unique magnetic properties – for example, magnetite (Fe_3O_4) nanoparticles are super-paramagnetic (magnetism induced by an external electric field) and have been studied as novel contrast agents for use in magnetic resonance imaging (MRI). Iron oxide nanoparticles have a high sensitivity to oxidation and readily generate ROS in biological media, making them ideal candidates for biosensors and also potentially toxic to cells (Zhang et al. 2003; Jeng and Swanson 2006). Cytotoxicity assays have shown adverse effects of iron oxide nanoparticles (Fe_2O_3 and Fe_3O_4) related to ROS generation both *in vivo* and *in vitro* (Lewinski et al. 2008). In a normal biochemical cycle within a cell, continuously produced ROS such as $OH^{\cdot}$ are effectively neutralized by antioxidants like glutathione (Voinov et al. 2011). It has been suggested that the accumulation of iron oxide nanoparticles in biological systems could lead to increased free iron levels and disrupt the normal ROS-antioxidant balance. Ferrous iron (Fe^{2+}) participating in these reactions can either be released into aqueous media by bare particles (or particles with compromised coatings) or may be absorbed onto the surface (Arbab et al. 2003; Wehrli et al. 1989).

Nanoscale buckminsterfullerene (nC_{60}) and other carbon-based nanomaterials have garnered significant attention for their wide range of potential applications, particularly in the fields of drug delivery, electronics, and materials science. Fullerenes are also highly photoreactive and susceptible to ROS generation in aqueous media, raising concerns regarding effects on environment and human health. For example, prior research has shown that nC_{60} exhibits reproductive toxicity in aquatic organisms (Tao et al. 2009), possesses antimicrobial properties (Fortner et al. 2005), and can significantly enhance the mobility of other contaminants, such as PCBs (Wang et al. 2013).

Nanoparticle Aggregation and Deposition

The mobility, bioavailability and toxicity of nanoparticles in the environment are largely determined by suspension stability, which is a function of solution chemistry (e.g., pH, ionic strength). The electrostatic forces that control nanoparticle stability in aqueous systems can be described by Derjaguin, Landau, Verwey and Overbeek (DLVO) theory (Derjaguin and Landau 1941; Verwey and Overbeek 1948). In DLVO theory, colloidal stability is determined by the balance between attractive van der Waals forces and repulsive electrostatic forces.

DLVO theory can be used to describe both nanoparticle-nanoparticle and nanoparticle-surface interactions. The total interaction energy (E_{total}) for both types of interactions can be calculated from the sum of the electrical double-layer repulsion energy (E_{edl}) and van der Waals attraction energy (E_v) (Guzman et al.

2006). One of the key assumptions of DLVO theory is that the electrical double layer and van der Waals forces can be treated independently, and are additive.

$$E_{total} = E_{edl} + E_v \quad (1)$$

The electrical double layer repulsive energy between two nanoparticles, $E_{dl\text{-}NN}$ (J), is calculated using Equation 2 (Gregory 1975),

$$E_{edl-NN} = \frac{64\pi nkTa}{\kappa^2} \tanh^2\left(\frac{ze\psi_p}{4kT}\right) e^{(-\kappa d)} \quad (2)$$

where n is the number of cations in solution, k is the Boltzmann constant (1.38×10^{-23} J·K^{-1}), T is the absolute temperature (K), a is the particle radius (m), κ is the Debye-Huckel reciprocal length (m), z is the charge number (-), e is the electron charge (1.60×10^{-19} C), ψ_p is the surface potential of the particle (V), and d is the surface to surface distance between particles (m). At low ionic strengths, the surface potential of the particle can be approximated by the zeta potential, which is determined from electrophoretic mobility measurements. The Debye-Huckel reciprocal length parameter, κ, is calculated by:

$$\kappa = \left(\frac{2000e^2 N_A I_C}{\epsilon_0 \epsilon_r kT}\right)^{1/2} \quad (3)$$

where ε_0 is the permittivity of a vacuum (8.85×10^{-12} C·V^{-1}m^{-1}), ε_r is the relative dielectric constant of water (80.1 at 20°C), N_A is Avogadro's number (6.02×10^{23} mol^{-1}), and I_C is the ionic strength (mol L^{-1}). The electrical double layer repulsive energy between a nanoparticle and a grain of sand ($E_{edl\text{-}NS}$) can be calculated using Equation 4 (Bhattacharjee and Elimelech 1997; Guzman et al. 2006):

$$E_{edl-NS} = \pi\epsilon_0\epsilon_r\kappa\left(\psi_p^2 + \psi_s^2\right) \times \int_0^a \left\{ -\coth\left[\kappa\left(d + a - a\sqrt{1-\left(\frac{r}{a}\right)^2}\right)\right] + \coth\left[\kappa\left(d + a + a\sqrt{1-\left(\frac{r}{a}\right)^2}\right)\right]\right\} r\, dr + \int_0^a \frac{2\psi_s\psi_p}{\psi_s + \psi_p}\left\{\operatorname{csch}\left[\kappa\left(d + a - a\sqrt{1-\left(\frac{r}{a}\right)^2}\right)\right] - \operatorname{csch}\left[\kappa\left(d + a + a\sqrt{1-\left(\frac{r}{a}\right)^2}\right)\right]\right\} r\, dr \quad (4)$$

The van der Waals attraction energy between two nanoparticles, $E_{v\text{-}NN}$ (J), is calculated by:

$$E_{v-NN} = \frac{-A_{NN}a}{12d}\left[1 - \frac{bd}{\lambda}\ln\left(1 + \frac{\lambda}{bd}\right)\right] \quad (5)$$

where A is the Hamaker constant for nanoparticle-water-nanoparticle (e.g., A = 3.7 x 10^{-20} J for 70 nm diameter citrate-coated nAg; Huynh and Chen 2011), b is a constant with a value of 5.32, and λ is the characteristic wavelength of the interaction (often assumed to be 100 nm). The van der Waals attraction energy between a nanoparticle and a grain of sand, $E_{v\text{-}NS}$ (J), can be calculated by (Bhattacharjee and Elimelech 1997):

$$E_{v-NS} = -\frac{A_{NS}}{6}\left[\frac{a}{d} + \frac{a}{d+2a} + \ln\left(\frac{d}{d+2a}\right)\right] \quad (6)$$

where A_{NS} is the Hamaker constant for nanoparticle-water-porous media interactions (e.g., 5.05 x 10^{-20} J for a magnetite (Fe_3O_4) nanoparticle-water-silica system).

The Hamaker constants for nanoparticle-water-nanoparticle (A_{313}) and nanoparticle-water-sand grain (A_{132}) interactions can be calculated using the following relationships:

$$A_{313} = \left(\sqrt{A_{11}} - \sqrt{A_{33}}\right)^2 \quad (7)$$

$$A_{132} = \left(\sqrt{A_{11}} - \sqrt{A_{33}}\right)\left(\sqrt{A_{22}} - \sqrt{A_{22}}\right) \quad (8)$$

where A_{11} = Hamaker constant for sand grain collector (e.g. 7.2 x 10^{-20} J for silica), A_{22} = Hamaker constant for water (3.7 x 10^{-20} J) and A_{33} = Hamaker constant for nanomaterial (e.g., 2.1 x 10^{-19} J for magnetite, Fe_3O_4).

The sum of the two energy terms (E_{edl} and E_v) provides a net energy, E_{total}, which can be used to generate an interaction energy profile of net interaction energy versus particle-particle distance or particle-sand grain distance. Negative values indicate a net attractive energy, while positive values indicate a net repulsive energy. DLVO theory is often used to support experimental observations of nanoparticle aggregation and deposition behavior (e.g. Huynh et al. 2011; Guzman et al. 2006). Interaction energy profiles can be used to predict whether conditions are favorable for nanoparticle deposition on sand grains. As illustrated in Figure 1 for a nano-CeO_2-water-sand system, the energy barrier decreases as electrolyte concentration increases due to greater compression of the electrical double layer. As the net interaction energy decreases, nanoparticle deposition on sand is expected to become more favorable due to lower repulsive forces between the particle and sand surface.

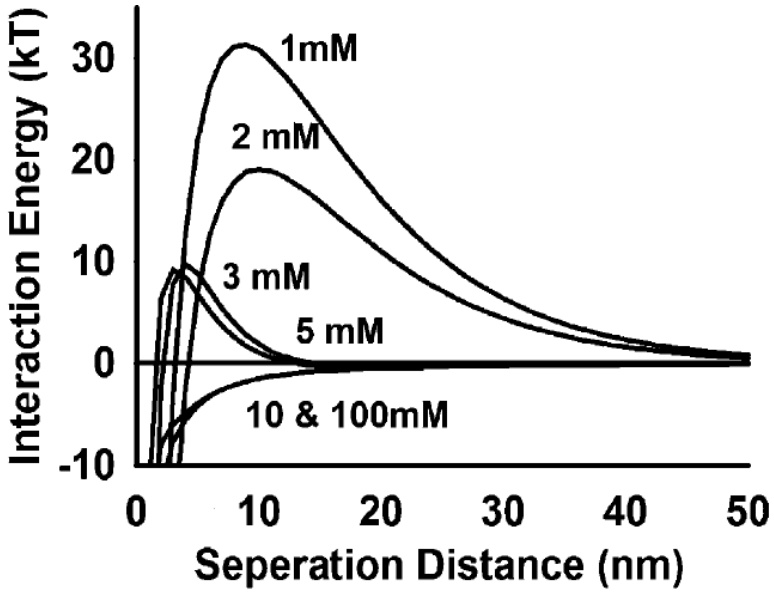

Figure 1. Nanoparticle-sand grain interaction energy profiles for nano-CeO_2 as a function of ionic strength (Li et al. 2011)

Deposition also becomes more favorable at certain pH ranges, depending on the nanoparticle point-of-zero charge (PZC). For example, nano-TiO_2-sand interaction profiles computed for a range of pH values (Figure 2) show that the lowest energy barriers occur at pH 3 and pH 7 for particles with a PZC of 6.2. As the pH was increased or decreased on either side of the PZC, positive interaction energy (net repulsion) was observed.

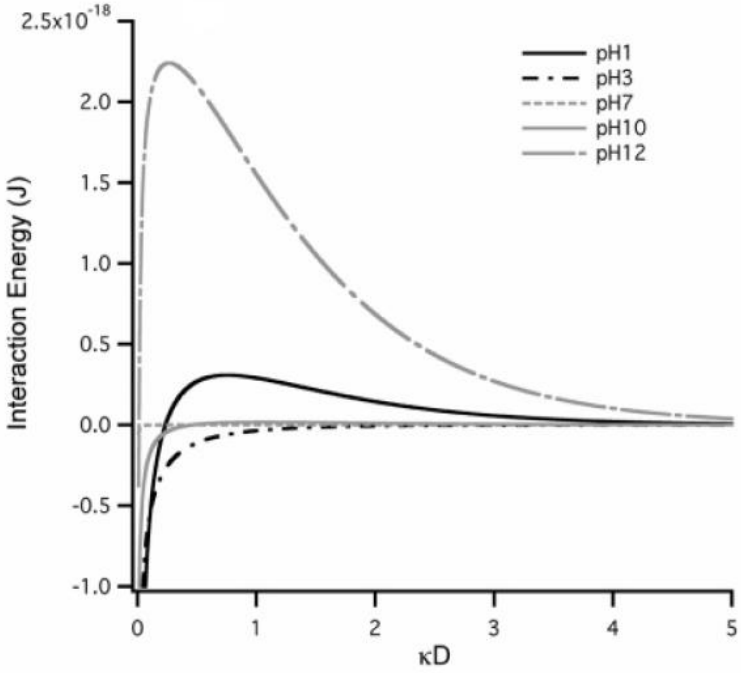

Figure 2. Nanoparticle-sand grain interaction energy profiles for nano-TiO2 (PZC = 6.2) as a function of pH (Guzman et al. 2006)

Aggregation Kinetics

DLVO theory can be used to quantitatively describe nanoparticle aggregation kinetics across a range of environmental conditions by considering the "fast" and "slow" aggregation schemes. The initial (fast) aggregation kinetics are derived from the initial rate of increase in the hydrodynamic radius (a_h). The increase in particle radius is linearly dependent on the primary particle concentration, N_0, as well as the initial aggregation rate constant, k_1 (Chen and Elimelech 2006).

$$\left(\frac{da_h(t)}{dt}\right)_{t\to 0} \propto k_1 N_0 \qquad (9)$$

The initial rate of increase is obtained by determining the initial slope (a_h vs. t) up to a point in time when the radius reaches a prescribed value (often taken to be 1.25 a_{h0}; Chen and Elimelech 2006). The critical coagulation concentration (CCC) is the point where aggregation kinetics transition from a rate-limited to a diffusion-limited regime, or the point at which the aggregation rate becomes independent of ionic strength. The aggregation attachment efficiency (α_A) (also referred to as the inverse stability ratio, *1/W*) is calculated for different electrolyte concentrations by normalizing slopes obtained under different solution chemistry to the slope obtained under fast (diffusion-limited) aggregation conditions (Chen and Elimelech 2006).

$$\propto_A = \frac{1}{W} = \frac{k_1}{k_{1,fast}} = \frac{\frac{1}{N_0}\left(\frac{da_h(t)}{dt}\right)_{t\to 0}}{\frac{1}{(N_0)_{\text{fast}}}\left(\frac{da_h(t)}{dt}\right)_{t\to 0,\text{fast}}} \qquad (10)$$

The stability ratio calculated using experimental data can be compared to DLVO theory predictions of aggregation behavior by (McGowan and Parfitt 1967)

$$W = \frac{\int_0^\infty \beta(h)\frac{exp[V_T(h)/kT]}{(2a+h)^2}dh}{\int_0^\infty \beta(h)\frac{exp[V_A(h)/kT]}{(2a+h)^2}dh} \qquad (11)$$

where h is the surface-to-surface separation distance between two particles, a is the particle radius, k is the Boltzmann constant and T is the absolute temperature. The total interaction energy between two particles, $V_T(h)$ is the sum of the van der Waals attraction, $V_A(h)$, and the electrical double layer interaction, $V_{edl}(h)$. The

dimensionless function, β, corrects for the hydrodynamic interaction between two approaching particles (Honig et al. 1971):

$$\beta_h = \frac{6\left(\frac{h}{a}\right)^2 + 13\left(\frac{h}{a}\right) + 2}{6\left(\frac{h}{a}\right)^2 + 4\left(\frac{h}{a}\right)^2} \qquad (12)$$

Many studies have documented the effect of solution chemistry (e.g. pH, ionic strength, electrolyte species) on nanoparticle aggregation and deposition kinetics though dynamic light scattering (DLS) studies. For example, French et al. (2009) evaluated the impact of ionic strength and ionic composition (Na^+ or Ca^{2+}) on nano-TiO_2 aggregation kinetics, and observed increased nano-TiO_2 aggregation in the presence of Ca^{2+} and with increasing ionic strength. Chen and Elimelech (2006) observed similar aggregation trends for fullerene nanoparticles in NaCl and $CaCl_2$ solutions. Plots of attachment efficiency versus ionic strength (Figure 3) were used to calculate CCC values of 0.12 M and 0.008 M in NaCl and $CaCl_2$, respectively.

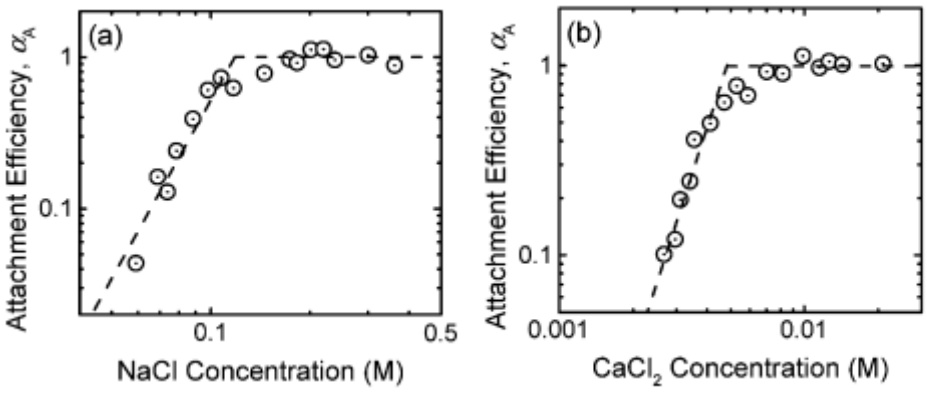

Figure 3. Attachment efficiency plots for fullerene nanoparticles in (a) NaCl and (b) $CaCl_2$ solutions (Chen and Elimelech 2006)

The combined effects of ionic strength, pH, ionic composition, NOM and other constituents of aqueous media can result in either aggregation or stabilization of colloidal system (Keller et al. 2010). While the formation of a protective layer of adsorbed polymer often stabilizes a colloid system, adsorbed polymers of higher molecular weight can also destabilize nanoparticle suspensions by causing polymer chains of adjacent particles to intertwine (Liufu et al. 2005). Several studies have examined the aggregation kinetics of nanoparticle systems in more complex environmental media containing NOM plus a combination of electrolyte species. For example, Huynh and Chen (2011) compared the aggregation kinetics of citrate- and polyvinylpyrrolindone (PVP)-coated silver nanoparticles in NaCl and $CaCl_2$ solutions and in the presence and absence of humic acid. The authors found that PVP-coated particles were significantly more stable in all solutions due to steric repulsion imparted by the non-ionic polymer. Divalent electrolytes were more efficient at destabilizing suspensions, while the adsorption of humic acid improved the stability of both types of coated particles, except at higher $CaCl_2$ concentrations, where interparticle Ca^{2+} bridging by humic acid aggregates occurred.

In another study, Keller et al. (2010) evaluated the stability of three nanoparticles (TiO_2, ZnO and CeO_2) in different water samples (seawater, artificial seawater, brackish lagoon, groundwater, stormwater and wastewater). The authors observed that the electrophoretic mobility (EPM) of nanoparticles in natural waters is controlled to a large extend by NOM and modulated by ionic strength. As the surface of the nanoparticle becomes coated with NOM, the particle charge is

dominated more and more by the charge of the NOM (Keller et al. 2010). Chowdhury et al. (2012) assessed the impact of NOM and bacteria on the aggregation and deposition of TiO_2 nanoparticles in aquatic systems, and found that the presence of both constituents imparted stability. The presence of NOM and bacteria increased stability at higher electrolyte concentrations and also increased the mobility of nano-TiO_2 in sand column experiments.

Zhang et al. (2008) evaluated the fate of commercial nanoparticles (TiO_2, $Fe2O_3$, ZnO, NiO, and silica) in DI water and tap water. Experimental results demonstrated that anionic functional groups and NOM in tap water adsorb onto nanoparticle surfaces and impart negative charge, regardless of whether surfaces were originally negatively or positively charged. Previous stability studies have clearly shown that NOM plays an important role in the fate of nanomaterials in the environment, primarily acting to reduce the size of aggregates and limit deposition through increased steric effects.

Nanoparticle Transport in Porous Media

Column Transport Studies

Nanomaterial transport in porous media has received attention in recent years as regulating agencies have struggled with the management of potential water and soil contamination originating from the growing nanotechnology industry. Transport studies with a variety of nanoparticles, including fullerene, titanium dioxide and single-walled carbon nanotubes, have shown that nanoparticle

transport behavior in water-saturated sands is highly sensitive to solution chemistry (e.g., Wang et al. 2008; Torkzaban et al. 2012; Lecoanet et al. 2004; Jaisi et al. 2008; Chen et al. 2011; Guzman et al. 2006). For example, Torkzaban (2012) reported that increasing ionic strength results in increased deposition of CdSe quantum dots, and Guzman (2006) demonstrated that deposition of nano-TiO_2 increases at pH values close to the particle PZC of 6.2.

Another study by Solovitch et al. (2010) evaluated the concurrent aggregation and deposition of nano-TiO_2 in sand columns as a function of pH. Effluent breakthrough curves for pH values on either side of the PZC (pH 5.5 for this system) are shown in Figure 4.

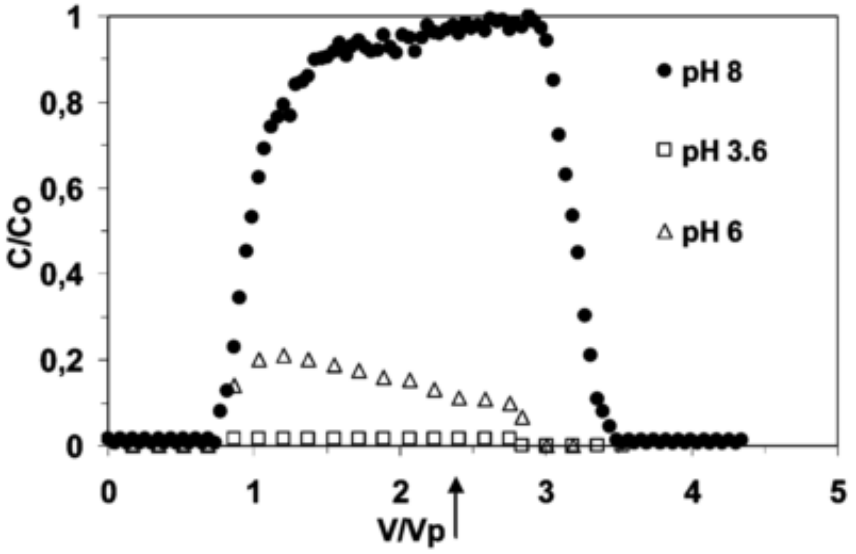

Figure 4. Effluent breakthrough curves for TiO_2 nanoparticles in silica sand as a function of pH (Solovitch et al. 2010).

The authors observed a slow decrease in the plateau of some TiO2 effluent breakthrough curves near the PZC due to particle aggregation and filter ripening,

where previously deposited particles and aggregates serve as preferential sites for subsequent deposition. Aggregation kinetic experiments show that particles at pH 6 were approximately double in size compared with particles at pH 8. Although aggregated nanoparticles will deposit more easily on sand grains due to their larger size, aggregates also have lower drag coefficients than individual, smaller particles, allowing them to travel at a higher velocity through preferential flow paths (Solovitch et al. 2010).

Several studies have examined the impact of stabilizing agents, such as polymer coatings or natural organic matter (NOM), on nanomaterial transport in porous media. For example, Joo et al. (2009) studied the influence of carboxylmethyl cellulose, an additive in pharmaceutical, medical, and food applications, on nano-TiO_2 nanoparticle transport in silica sands. The authors found that polymer-coated nano-TiO_2 exhibited earlier breakthrough than uncoated particles, which was attributed to pore exclusion or preferential flow promoted by increased viscosity of the solution (Joo et al. 2009). Chen et al. (2011) evaluated the impact of humic acid on the transport and retention of nano-TiO_2 across a range of ionic strength and pH conditions, and observed that the transport of nano-TiO_2 was greatly enhanced in the presence of humic acid due to adsorption of NOM to both nanoparticle and sand surfaces. A study by Godinez and Darnault (2011) found that the presence of either a non-ionic surfactant (Triton X-100) or anionic surfactant (SDBS) induced up to a 50% reduction in aggregate size, which allowed for greater transport of nano-TiO_2 in sand columns.

Despite the importance of deposition in nanoparticle transport, very few nanoparticle transport studies report the solid-phase concentrations along the length of the column or provide a retention (deposition) profile. Several studies that provide retention data include Bradford et al. (2011), Chen et al. (2011) and Wang et al. (2008). For example, Chen et al. (2011) provided retention and breakthrough data for sand column experiments with nano-TiO_2 conducted at different ionic strengths (Figure 5).

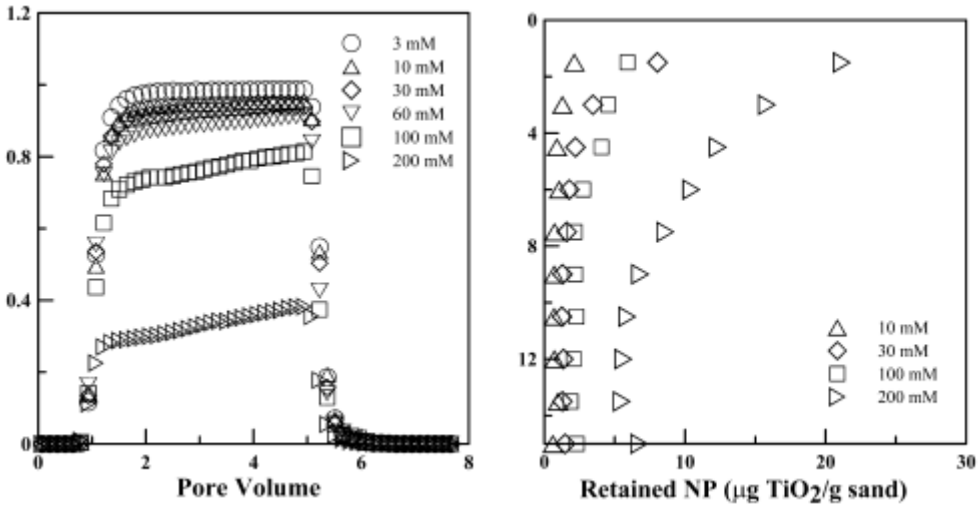

Figure 5. Effluent breakthrough curves and corresponding retention profiles for nano-TiO*2* transport in sand columns as a function of ionic strength (Chen et al. 2011)

The combination of both effluent breakthrough and retention data provides a more complete assessment of transport and deposition mechanisms than breakthrough curves alone. Asymmetrical breakthrough curves suggest blocking of attachment sites and a limited retention capacity, whereas hyperexponential retention profiles

may indicate physical straining or filter ripening. Colloid retention mechanisms are discussed in more detail in the following section.

Filtration Theory Models

Filtration models are regularly used to predict the transport behavior of colloids as a function of suspension characteristics, porous media properties and flow conditions. Classical colloid filtration theory (CFT) was first presented by Yao et al. (1971). Based on CFT, the transport and deposition of colloids in porous media can be described by the one-dimensional advection-dispersion equation,

$$\frac{\partial C}{\partial t} + \frac{\rho_b}{\theta}\frac{\partial S}{\partial T} = D_h \frac{\partial^2 C}{\partial t} - v_p \frac{\partial C}{\partial x} \quad (12)$$

where C is the aqueous phase concentration, ρ_B is the bulk density of the porous medium, θ is the volumetric water content, S is the solid-phase concentration, D_h is the hydrodynamic dispersion, v_p is the pore water velocity and x is distance.

The kinetics of attachment to the solid phase can be described by a first order decay rate (k_{att}):

$$\frac{\rho_b}{\theta}\frac{\partial S}{\partial T} = k_{att} C \quad (13)$$

The filtration of suspended particles by a porous medium is often thought to involve two distinct steps: (1) transport of suspended particles to the collector surface (e.g., sand grain), and (2) attachment of particles to the collector surface. In CFT, transport to the collector occurs via three mechanisms: sedimentation by gravitational force, interception along the streamlines and random motion due to

Brownian diffusion (Yao et al. 1971). These three mechanisms are controlled by physical factors, such as flow velocity, grain size and porosity, and are described by a single term, η_0, the single collector efficiency (ie., ratio between the rate at which particles strike the collector divided by the rate at which particles flow towards the collector). Particle attachment to the collector is governed by the interaction forces between particles and collector surfaces (e.g., DLVO theory) and is described by the attachment efficiency term, α. The attachment efficiency represents the fraction of particle collisions with the solid phase (e.g., individual sand grains) that result in attachment. When the value of α approaches 1, conditions for attachment are considered "favorable" for attachment. In practice, collision efficiencies less than ca. 0.5 fall within the unfavorable deposition region (Elimelech et al. 1995).

The removal efficiency of filter media is determined empirically using correlations for α and η_0 (e.g. Yao et al. 1971; Tufenkji and Elimelech 2004). Yao et al. (1971) proposed one such correlation for α,

$$\alpha = -\left(\frac{2d_c}{3(1-\theta)\eta_0 L}\right)\ln\left(\frac{C}{C_0}\right) \qquad (14)$$

where L is the depth of the filter media and C/C_0 is the normalized effluent concentration.

Equation 14 is an analytical solution to Eq. 12 with several assumptions: 1) steady-state conditions ($\delta C/\delta t = 0$); 2) the advective term is represented by Stokes equations for laminar flow around a sphere; 3) Einstein equation is used to

estimate the diffusion coefficient of suspended colloids; 4) boundary conditions assume that $C = C_0$ at an infinite distance from the collector and $C = 0$ at a distance of $(d + d_p)/2$ from the center of the collector; 5) deposition within the pores has not significantly altered the flow or porous medium characteristics (clean bed assumption) (Yao et al. 1971).

Tufenkji and Elimelech (2005) showed that CFT may be valid for highly idealized systems (e.g., latex microspheres and glass beads). In most natural systems, however, physical-chemical non-idealities (e.g., limited number of sites for attachment, depth-dependent deposition) contribute to significant deviations from CFT. Nonetheless, CFT is frequently used to interpret nanoparticle transport results under many different conditions, even when observed breakthrough and retention data are inconsistent with the assumptions of clean-bed filtration theory described previously (e.g. Lecoanet and Wisner 2004; Li et al. 2011; Epinasse et al. 2007).

To account for deviations from CFT, several modified filtration theory models have been developed. One such modification to CFT was proposed by Wang et al. (2008) and includes a maximum retention capacity term (S_{max}) and a detachment rate (k_{det}). In MFT, the attachment term is modified by a Ψ term, which considers a finite retention capacity.

$$\frac{\rho_b}{\theta}\frac{\partial S}{\partial T} = k_{att}\Psi C - k_{det}\frac{\rho_b}{\theta}S \qquad (15)$$

$$\Psi = \frac{S_{max} - S}{S_{max}} \qquad (16)$$

where S_{max} is the maximum solid-phase capacity and S is the solid-phase concentration. The blocking term, Ψ, implies that retention decreases with time and that the retention profile becomes uniform with depth as S approaches S_{max}. Note that when $\Psi = 1$, retention behavior is similar to classical filtration theory.

Maximum retention capacity models have been shown to more accurately model transport and deposition behavior of nanoparticles such as C_{60} aggregates (Wang et al. 2008; Li et al. 2008) and CdSe quantum dots (Torkzaban et al. 2010) in glass beads and silica sands. For example, Li et al. (2008) used a S_{max}-modified filtration theory (MFT) to model nC_{60} transport and retention in different sized fractions of Ottawa sand (Figure 6). MFT accurately captured the asymmetrical, late breakthrough and decreasing retention along the column length (from inlet to outlet).

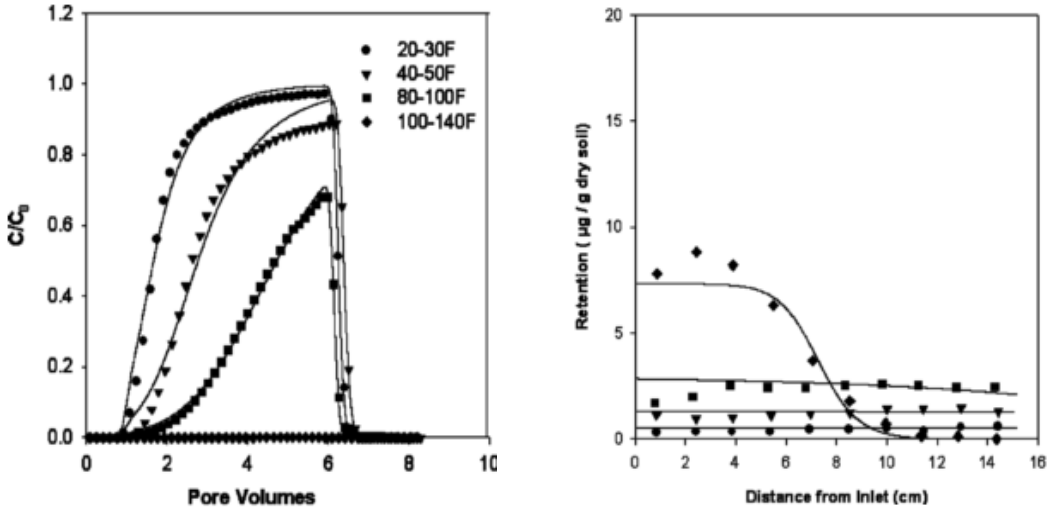

Figure 6. MFT model fits to nC_{60} effluent breakthrough and retention data in different sized fractions of Ottawa sand (Li et al. 2008)

Some nanoparticle-porous media systems display hyper-exponential retention behavior (higher-than-predicted retention at the column inlet), which cannot be described by CFT or MFT (Figure 7). Hyper-exponential behavior has been attributed to physical straining (Bradford et al. 2003), sand surface charge heterogeneity or roughness (Li et al. 2006; Song et al. 2004) and particle population heterogeneity (Tong and Johnson 2006). Physical straining occurs when the suspended particle diameter is larger than the pore throats of the porous medium. Hyperexponential retention behavior has been described by modifying the blocking function adding a depth dependent power law to the blocking function, Ψ:

$$\frac{\rho_b}{\theta}\frac{\partial S}{\partial t} = k_{str}\Psi_{str}C \qquad (17)$$

$$\Psi_{str} = \left(1 - \frac{S}{S_{max}}\right)\left(\frac{d_{50} + z}{d_{50}}\right)^{-\beta} \qquad (18)$$

where d_{50} is the mean grain size of the porous media, z is bed depth and β is a particle- and system-specific fitting parameter. In this modification of CFT, the first term describes an MFT-type blocking function and the second term contains a depth-dependent power law to describe straining (Bradford et al. 2003; 2006).

Equations 17 and 18 are empirical formulations without a mechanistic basis. Experiments conducted by Xu et al. (2006) suggest that straining can be observed at particle diameter to sand grain diameter ratios as low as 8 x 10^{-3}. The ratio of diameters of many nanoparticles (e.g., 10-100 nm) to medium-grain sands (e.g., 300-500 μm) are more than two orders of magnitude smaller than the proposed

threshold value for straining. Nonetheless, the "S_{max}-straining" modification of CFT presented by Bradford et al. (2006) is still used to represent nanoparticle systems that display hyperexponential retention behavior. For example, Liang et al. (2013) used a S_{max}-straining formulation to model nAg (d_p = 50 nm) transport in silica sands of varying grain size (240 – 600 µm) (Figure 7).

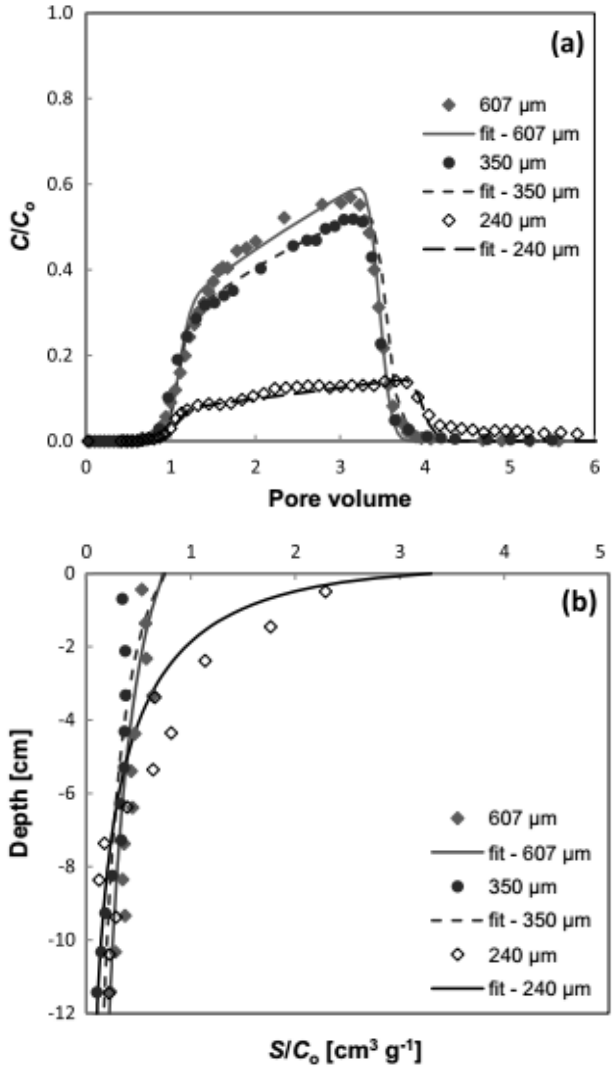

Figure 7. Maximum retention capacity/straining model fits to observed (a) effluent breakthrough curves and (b) retention profiles for nAg transport in different size fractions of quartz sands (Liang et al. 2013)

An MFT model (S_{max}-modification) accurately represents the asymmetrical breakthrough curves, while the S_{max}-straining model is able to capture the general shape of the hyperexponential retention profiles. It is important to note that most particle straining work was based on systems with micron-sized particles (e.g., Xu et al. 2006), rather than colloids in 1-100 nm range.

Parameters derived from the application of filtration theory models to experimental column data, such as α, η_0 and β, can be used to examine relationships between physical-chemical system parameters (e.g., grain size, cation species) and nanoparticle transport and deposition in porous media. Using an S_{max}-modified model, Wang et al. (2008) reported that collision efficiency values for nC_{60} transport were two orders of magnitude smaller in glass beads compared with Ottawa sand, consistent with the transport and retention behavior observed in column experiments. Li et al. (2008) reported that k_{att} (3.21 – 33.6 h^{-1}) and S_{max} (0.44 – 11.45 µg/g) values for nC_{60} transport in Ottawa sand increased and collision efficiency values (0.134 – 0.150) decreased as grain size was decreased. Velocity was also observed to have an impact on model parameters (e.g., values of S_{max} approximately doubled when velocity was decreased from ca. 8 m/d to 1 m/d) in all size fractions of Ottawa sand (Figure 8).

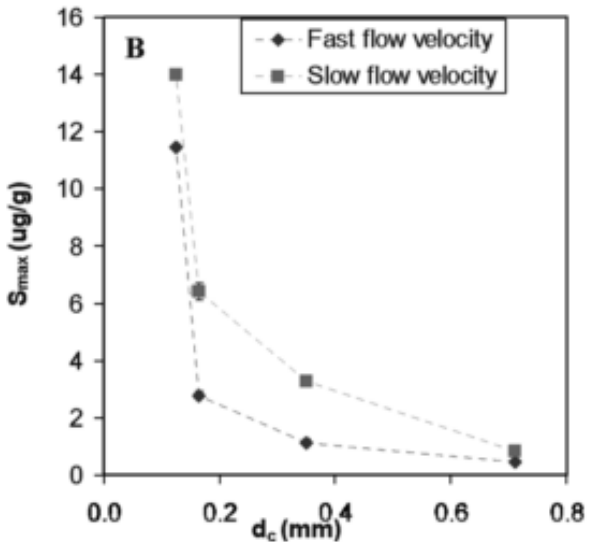

Figure 8. Comparison of simulated maximum retention capacities (S_{max}) as a function of sand grain size at two flow velocities (fast flow = 8m/d and slow flow = 1 m/d) (Li et al. 2008)

QCM-D and Nanoparticle Deposition

Quartz crystal microbalance with dissipation (QCM-D) can also be used to explore deposition behavior of nanoparticles across a range of solution chemistry conditions. QCM-D has traditionally been used in the biological sciences to measure deposition rates of proteins, polymers, surfactants and cells onto biologically relevant surfaces in different aqueous media. It has recently seen increased use as a tool for examining interactions between colloids and environmental surfaces (e.g., Chen and Elimelech 2006; Jiang et al. 2010; Thio et al. 2011). In the QCM-D system, a thin quartz disk is located between a pair of electrodes. When AC voltage is applied across the electrodes, the crystal is excited and oscillates, and when a solution containing the constituent of interest

flows over the disk, depositing mass causes changes in oscillation of the sensor. Sensors can be fabricated with a broad range of substrates depending on the application, including ceramic, polymers and metal oxides (Q-Sense 2013).

The kinetics of structural and mass changes in the adsorbed layer can be obtained simultaneously by monitoring changes in the frequency and dissipation, respectively (Q-Sense 2013). The mass of the adsorbed layer is calculated using the Sauerbrey relation (Sauerbrey 1959),

$$\Delta m = -\frac{C \cdot \Delta f}{n} \qquad (19)$$

where m is the mass deposited per area, C is the crystal constant (17.7 ng/Hz cm^2 for a 5 MHz quartz crystal), f is the frequency of the oscillating crystal, and n is the dimensionless overtone number (1, 3, 5…). Frequencies above the fundamental frequency (n = 1, e.g., 5 MHz) of the oscillating crystal are called overtones.

A quantitative nanoparticle deposition rate (Hz t^{-1}) can be obtained by monitoring the rate in frequency shift at the third overtone (Chen and Elimelech 2006):

$$k_{QCM} = {}^{d\Delta f_3}/_{dt} \qquad (20)$$

An estimation of the thickness of the deposited layer (d_{eff}) can also be calculated:

$$d_{eff} = \frac{\Delta m}{\rho_{eff}} \qquad (21)$$

where p_{eff} is the effective density of the layer.

In most cases, the adsorbed layer is not rigid; "soft" or viscoelastic films will not fully couple to the oscillation of the crystal, causing the Sauerbrey equation (Eq. 21) to underestimate the mass deposited on the surface. The damping or energy dissipation (*D*) in the oscillation provides insight into the adsorbed layer's viscoelasticity,

$$D = \frac{E_{lost}}{2\pi E_{stored}} \qquad (22)$$

where *D* is the dissipation factor (-), E_{lost} is the energy dissipated during one oscillation cycle (V) and E_{stored} is the total energy stored in the sensor (V). By measuring at multiple frequencies (e.g., 3rd, 5th or 7th overtone, or 15, 25 or 35 MHz), information related to the viscosity, elasticity and thickness of the adsorbed layer can be collected for non-rigid layers (QSense 2013; Chen and Elimelech 2006).

Several studies have examined nanomaterial deposition on silica and other environmentally-relevant surfaces (Chen & Elimelech 2006; Liu et al. 2011; Liu et al. 2012; Fatisson et al. 2009; Quevedo et al. 2014; Thio et al. 2011). Chen and Elimelech (2006) evaluated fullerene deposition on a quartz QCM-D sensor in NaCl and $CaCl_2$ solutions of varying ionic strength (Figure 9). The quartz surface represents an "unfavorable" surface with net positive interaction energy (an energy barrier to fullerene deposition). A favorable deposition surface was obtained by coating the QCM sensor with positively charged poly-L-lysine (PLL) The slope of frequency shift vs. time becomes steeper as ionic strength increases,

indicating that deposition rate increases with increasing ionic strength, consistent with DLVO theory.

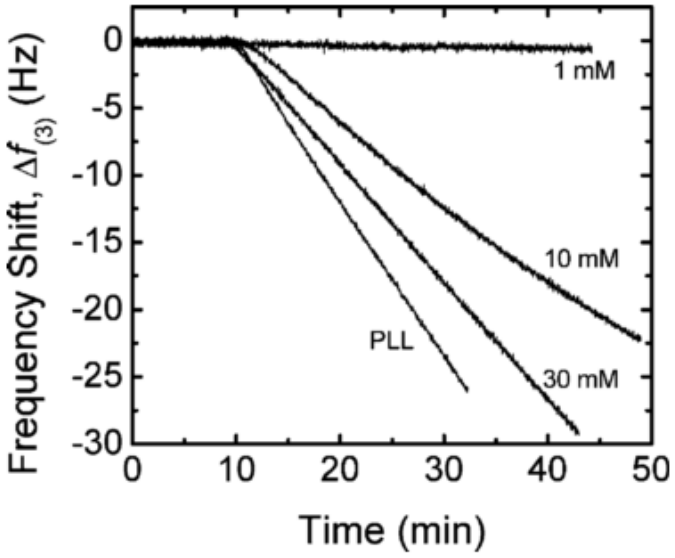

Figure 9. Deposition of fullerene nanoparticles onto a silica-coated quartz surface in the presence of 1, 10 and 30 mM NaCl (Chen and Elimelech 2006)

In another QCM-D deposition study, Fatisson et al. (2009) found that nano-TiO_2 deposition increased with increasing ionic strength, and as the pH moved farther from the point of zero charge (pH 5). Jiang et al. (2010) compared the deposition kinetics of ZnO nanoparticles on silica surfaces and surfaces pre-coated with humic acid over a range of ionic strengths in monovalent and divalent electrolyte solutions. Deposition increased with increasing ionic strength on the bare silica surfaces, while surfaces coated with humic acid hindered the deposition of ZnO nanoparticles in both monovalent and divalent solutions, consistent with steric repulsion imparted by NOM (Jiang et al. 2010). Thio et al. (2011) also evaluated the influence of NOM on the aggregation and deposition of nano-TiO_2 using QCM-D, and found that deposition rates decreased in the presence of humic acid.

Prior studies have noted some limitations of QCM-D in measuring nanoparticle deposition at higher ionic strengths due to aggregate formation (Chen & Elimelech, 2006; Fatisson, et al., 2009; Quevedo, et al., 2014). For example, Quevedo (2014) observed a decrease in nano-silicon deposition on silica-coated sensors when aggregates grew to >700 nm in diameter, and Chen and Elimelech (2006) report decreased attachment of nC_{60} at ionic strengths near the CCC (120 mM NaCl). It was suggested that rapid aggregate formation led to a sharp decrease in the diffusion coefficient of the nanoparticles, and thus resulted in reduced convective-diffusive transport of the aggregates toward the sensor surface.

Liu et al. (2012) and Quevedo et al. (2014) conducted complementary column studies in conjunction with QCM experiments, and observed some inconsistencies between the different experimental approaches. In particular, the greater retention observed in sand columns was attributed to the effects of nanoparticle aggregation, physical straining, and differences in surface heterogeneity between the porous media and silica sensors. It is important to note that all prior QCM deposition experiments were conducted at flow rates of 0.1-0.4 mL/min, while corresponding column studies were conducted at pore-water velocities of 9-11 m/d. There have been no efforts to date to equate linear velocities between the two systems or consider differences in surface area available for deposition. In addition, deposition rates obtained from QCM-D experiments have not yet been related to attachment parameters derived from sand column studies.

Nanoparticle Surface Transformations

Aging Mechanisms

Inorganic and organic coatings are widely used to stabilize nanoparticles in aqueous systems. Nanoparticle coatings will be exposed to a wide variety of physical and chemical transformations when released into the natural environment. Redox processes may induce breakdown of organic coatings on nanoparticle surface and can promote dissolution of metallic species (Metz et al. 2009). Ultra-violet (UV) light can catalyze radical reactions, which in turn can cause degradation of coatings. Exposure to NOM and to organic acids (e.g., citric or oxalic acid) can further alter the surface chemistry of nanomaterials, directly affecting their fate and mobility in the environment (e.g. Johnson et al., 2006; Di Palma and Mecozzi 2007). Previous studies have evaluated the aging of nanoparticles exposed to natural waters (Li and Lenhart 2012; Sarathy et al. 2008; Reinsch et al. 2010), swimming pool water (Virkutyte et al. 2012), organic acids (Mudukotuwa et al. 2011), clay and dissolved organic matter (Coutris et al. 2012; Scheckel et al. 2010), and ultra-violet light (Labille et al. 2010; Auffan et al. 2010; Li and Lenhart 2012; Gorham et al. 2012; Hou and Jafvert 2012; Lee et al. 2009; Cheng et al. 2011).

Exposure to sunlight is a particularly interesting aging mechanism, as ultra-violet (UV) light can catalyze radical reactions, which in turn can cause surface degradation and the production of potentially toxic byproducts. For example, Hou and Jafvert (2009) found that aqueous nC_{60} clusters, when exposed to sunlight,

lost their characteristic yellow-brown color, decreased in size, and formed water soluble byproducts. Auffan et al. (2010) investigated surface coating degradation of an aluminum oxide-poludimethylsiloxane (PDMS)-coated nano-TiO_2 used in cosmetics. The authors monitored the release of Si and Al from coated nano-TiO_2 in aqueous batch systems with and without UV light illumination, and observed that release of Si due to desorption of the PDMS layer was time-dependent and sensitive to illumination, whereas dissolution of Al from the $Al(OH)_3$ layer was consistently low (< 5 wt%) under both light and dark conditions (Auffan et al. 2010). The same study showed that nano-TiO_2 became more hydrophilic (dispersed) and formed aggregates in aqueous solutions overtime due to desorption and oxidation of the amphiphilic polymer coating. UV light has also been shown to accelerate the oxidative aging of citrate-coated nAg. When nAg of different mean diameters (20, 40, 60 and 80 nm) were irradiated with UV light, Gorham et al. (2012) found that the rate of loss of peak surface plasmon resonance (SPR) absorbance in UV-vis spectra corresponded with an increase in free citrate concentrations, production of silver ions, and the appearance of a core-shell structure (Ag^0 core/Ag_2O shell).

Several previous studies have reported that aging of the silver nanoparticle surface results in the formation of a silver oxide coating (Ag_2O) (Chen et al. 2006; Li et al. 2010; Schmidt et al. 2003). The presence and growth of oxide layers on the surface of nAg can be confirmed using UV-vis spectroscopy (Henglein 1998; Mulvaney et al. 1991). Surface oxidation has been observed to cause slight red

shifts in spectra, a decrease in spectra peak maxima and broadening of the spectra over time (Mittelman et al. 2013; Henglein 1998).

Aging of nAg has also been linked to a reduction in dissolution (Coutris et al. 2012; Scheckel et al. 2010; Mittelman et al. 2013). For example, Coutris et al. (2012) reported a reduction in the water soluble and ion exchangeable fractions of citrate-stabilized nAg from 37 ± 4.8% after 2 hours to 1.8 ± 0.1% after 70 days. Mittelman et al. (2013) observed a decrease in the dissolution of nAg retained in water-saturated sand overtime, which was attributed to particle aging and the formation of an oxide layer on the attached particle surfaces. Scheckel et al. (2010) assessed the influence of aging on the speciation and chemical stability of silver and zinc oxide nanoparticles in kaolin suspensions over periods up to 18 months. The authors found that nAg in NaCl solutions formed a silver chloride surface coating, but otherwise remained stable, while oxide nanoparticles underwent rapid loss of stability and dissolution and were converted to Zn^{2+} complexes within one day of aging.

Natural organic matter, including humic acid, has been shown to passivate the surface of metallic nanoparticles by forming a protective coating. Several studies have reported that humic acid interferes with silver dissolution reactions in aqueous systems and imparts greater stability to nanoparticle suspensions (Zhang et al. 2012; Liu and Hurt 2010). Organic acids, like citric and oxalic acid, can either inhibit or promote dissolution and/or aggregation. For example, organic acids can promote dissolution of metals through chelation by polarizing the surface and weakening surface metal-oxygen or metal-metal bonds (Johnson et al.

2007). Mudunkotuwa et al. (2012) investigated the impact of citric and oxalic acid on the behavior of three different types of copper-based nanoparticles (new Cu, aged Cu and CuO). Surface interactions between Cu nanoparticles and organic acids were highly sensitive to pH, since it determines the speciation and charge of the acid. The authors found that citric acid shifted the particle surface charge to more negative values and promoted dissolution of Cu and CuO nanoparticles, resulting in the formation of Cu^{2+} and smaller nanoparticles. Oxalic acid on the other hand was observed to increase aggregation and inhibit dissolution of Cu and CuO nanoparticles (Mundunkotuwa et al. 2012).

Aging and Nanomaterial Toxicity

Nanomaterials may exhibit different toxicity following exposure to environmental or biological media, due to processes such as dissolution, reactive oxygen species (ROS) production, or alteration in surface charge. ROS in particular play an important role in the reactivity and toxicity of many nanomaterials. When metallic nanomaterials are exposed to aqueous media, ROS may be produced at the metallic nanomaterial surface or in solution. The surface of nanomaterials is highly active and electron transfers can lead to generation of hydroxide peroxide (H_20_2) and ROS (Kühn et al. 2003; Zhang et al. 2009). Radical species can attack organic coatings on the nanoparticle surface and cause damage to cellular organisms through oxidative stress (Metz et al. 2009). Nanomaterials can directly enter the cell membrane due to their small size and cause a cascade of damage related to ROS production. ROS can oxidize proteins, damage DNA and interfere with energy production in mitochondria. Metal ions released from nanomaterials

through dissolution reactions can also trigger ROS production and directly interfere with cellular function. ROS production, dissolution, and other aging-related events can have important implications in the antimicrobial efficacy and observed toxicity of nanomaterials.

A limited number of studies have examined the role aging plays in nanomaterial toxicity in environmental and biological systems (Lee et al. 2009; Cheng et al. 2011; Mahendra et al. 2008; Phenrat et al. 2009a; Yang et al. 2011; Song et al. 2010). For example, Mahendra et al. (2008) observed a significant increase in the microbial toxicity of quantum dots (QDs) upon aging under acidic or alkaline conditions. Toxicity was attributed to loss of the organic coating and release of toxic cadmium and selenite ions from the heavy metal core and shell. In an *in vitro* toxicity study, Phenrat et al. (2009a) found that fresh (non-aged) nZVI particle exhibited significantly greater oxidative stress in mouse neurons than aged nZVI, indicating that surface oxidation rendered nZVI less toxic over time. Lee et al. (2009) evaluated the toxicity of quantum dots against the freshwater macroinvertebrate *Daphnia magna*, and found that toxicity increased in the presence of UV light. The authors hypothesized that toxicity increased due to decreasing size of the particles due to coating degradation and dissolution, release of toxic ions, and the generation of ROS.

The degree of dissolution of various metallic nanoparticles (e.g., nAg, nano-ZnO, quantum dots) is often directly correlated with observed toxicity to aquatic organisms and bacteria (Hardman 2006; Xia et al. 2008; Song et al. 2010; Choi et al. 2008). For example, Song et al. (2010) evaluated the cytotoxicity of ZnO

nanoparticles in mouse macrophage cells and observed a significant correlation between Zn^{2+} concentration released into growth media and cell viability. Uptake of ZnO nanoparticles by cells was also reported to cause rapid dissolution, with a release of Zn^{2+} ions. Humic acid has been observed to mitigate the toxicity of dissolvable particles like nAg against aquatic organisms, primarily by hindering dissolution reactions and binding Ag^{+} in solution (Dasari and Hwang 2010; Gao et al. 2012; Liu and Hurt 2010). Another nAg toxicity study by Yang et al. (2011) found that particle coating type impacted both the extent of dissolution and observed toxicity to the nematode *C. elegans*. The authors attributed reduced toxicity in citrate-coated nAg to sorption of Ag^{+} onto the citrate coating and complexation of Ag^{+} in solution by free citrate.

The few toxicity studies that account for aging have shown that nanomaterial biocompatibility and ecotoxicity tests should consider *in vivo* and/or in situ transformations to more fully characterize potential risks to environmental health.

Impact of Aging on Nanomaterial Transport

Aging can also have important implications on nanoparticle fate and transport in porous media. While previous research has demonstrated that nanomaterials exhibit changes in size, surface chemistry, stability, and toxicity following exposure to environmental or biological media, these transformations have rarely been accounted for in traditional groundwater transport experiments. With the exception of one study by Kim et al. (2009), prior transport studies have utilized freshly prepared suspensions that fail to capture realistic aging processes that may

occur in the environment. Kim et al. (2009) evaluated the mobility of polymer-coated nZVI in sand columns after aging, and found no significant difference in mobility between aged particles and fresh particles, but note that polymer-coated nZVI remained more mobile than their unmodified counterparts even after aging.

Silver Nanoparticles and Ceramic Water Filters

It is also important to consider the effects of aging on the fate of nanomaterials in engineered porous media, such as water filtration devices. The second part of this research focused on the fate of silver nanoparticles used in household water treatment devices and their role in reducing water-borne disease burden.

Point-of-Use Water Treatment

According to the latest progress report by the World Health Organization (WHO) and the UNICEF Joint Monitoring Program (JMP) on global sanitation and drinking water, an estimated 768 million people relied on unimproved drinking water sources and 2.5 billion people lacked access to an improved sanitation facility in 2011 (WHO and UNICEF 2013). JMP has designated drinking water sources as either improved and unimproved (Figure 10). Improved drinking water sources are protected from outside contamination, in particular from contamination with fecal matter (JMP 2013), and include public taps and protected dug wells. Unimproved drinking water sources include tanker trunks and surface water.

Figure 10. Drinking water sources designated as improved or unimproved by the WHO and UNICEF (WHO and UNICEF 2013)

Worldwide, approximately 2 million people die every year as a result of diarrheal diseases, most of who are under the age of five. The disease burden is concentrated in sub-Saharan Africa, where the WHO estimates that approximately 115 people die every hour from diseases linked to poor sanitation, hygiene and contaminated water (WHO and UNICEF 2013; WHO 2013a). Most diarrheal deaths in children are a result of malnutrition, concurrent diseases such as malaria and HIV, and a lack of access to proper medical care. A fraction of water-related diseases can also be attributed to the method in which water resources are developed and managed. In many parts of the developing world, industrial water pollution, dam construction, agricultural development and flood control can exacerbate the disease burden (WHO 2013a, 2013b). In addition, lack of

sanitation facilities force people to defecate in the open, in surface water bodies and in close proximity to areas where children play and food is prepared. In areas where wastewater collection systems exist, a lack of treatment facilities can lead to raw sewage directly entering receiving bodies. For example, an estimated 1.1 million liters of raw sewage are dumped into the Ganges River in India every minute (WHO 2013b, 2013c).

In order to realize the greatest improvements in human health, improvements in water supply, water treatment and sanitation infrastructure, and hygiene education are needed in developing countries. Improved drinking water sources, such as piped supplies on premises, are often associated with the best health outcomes (UNICEF and WHO 2013). The percentages of the population by country that have access to improved drinking water resources are shown in Figure 11. Sub-Saharan Africa and Oceania have the lowest drinking water coverage.

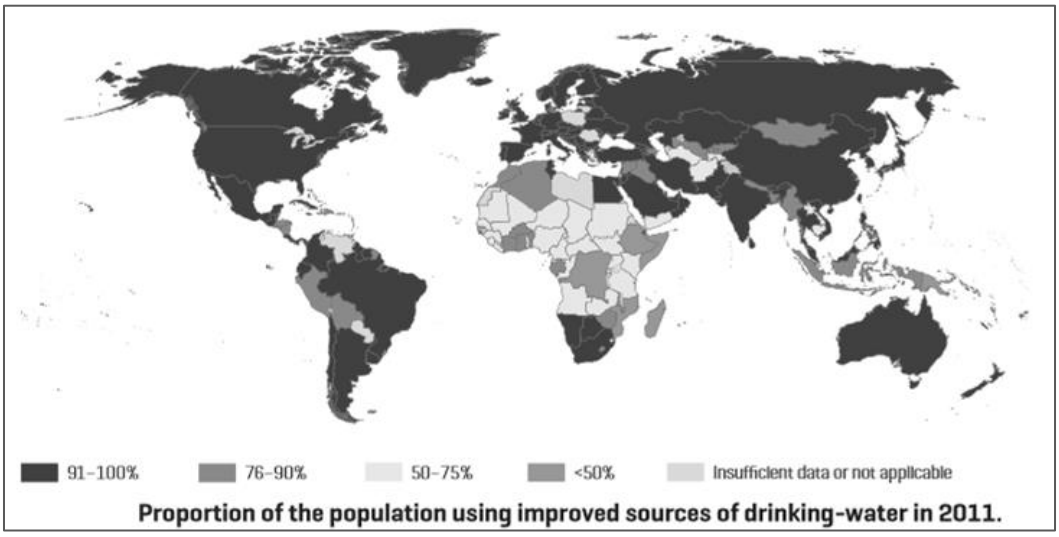

Figure 11. Percentages of global population using improved drinking water resources in 2011 (WHO and UNICEF 2013)

An estimated 1.5 billion people have gained access to piped supplies since 1990; however, supplies can often be intermittent, untreated or insufficiently treated, which increases contamination risks. In rural areas, 1.7 billion people still rely on non-piped supplies, such as public taps, hand pumps, protected wells, protected springs and rainwater. In areas without piped drinking water networks and where existing water resources are untreated, insufficiently treated or become contaminated during distribution or storage, household water treatment and safe storage (HWTS) options, such as chlorine or filtration methods, can play an important role in providing safe drinking water (UNICEF and WHO 2013).

Point of use (POU) treatment technologies can be employed at the household level or in other settings, such as schools and hospitals, and can be also a key component of emergency response to floods or other extreme events (WHO 2011). Five approaches have been shown to reduce diarrheal disease in users and improve the quality of stored household water: chlorination, sand filtration, ceramic filtration, PuR Purifier of Water flocculent/disinfectant, and Solar Disinfection (SODIS). Each of these options has benefits and drawbacks, and locations where the option is more appropriate. For example, chlorination and boiling of water can be convenient and inexpensive options; however, chlorination is often performed incorrectly and water is boiled for an insufficient amount of time to ensure disinfection (Lantagne 2001).

The ceramic water filter (CWF), promoted by Potters for Peace and other organizations, and manufactured locally in more than 50 factories in developing countries worldwide provides high efficiency contaminant removal in an easily

adoptable format. Filters are shaped like an inverted-cone flower pot and sit inside a receptacle (e.g., plastic bucket) fitted with a spigot (Figure 12). Water is poured into the ceramic pot and allowed to flow through the filter by gravity. A plastic or ceramic lid is used to cover the filter during use and storage (CMWG 2011). Filters reduce contaminant load in water by trapping small particles and microorganisms larger than the pore size of the filter (ca. 1 μm) and through action of colloidal silver (nAg), which is applied to the filters to prevent bacterial growth in the filter itself, and possibly provide additional antimicrobial activity (CMWG 2011).

Figure 12. Potters for Peace ceramic water filter and plastic receptacle (Potters for Peace 2013)

The filters do not impart an objectionable taste to treated water and are considered a socially acceptable technology that can be used year around in different climates (Oyanedel-Craver and Smith 2008). The Potters for Peace ceramic filter can be

manufactured using primarily local materials and labor. The average wholesale price of a complete filter unit (ceramic filter element and receiving receptacle) is $15.71 USD, and the average retail price is $16.68 (Rayner 2009). Overall, field studies have found high user acceptability of ceramic filters and the potential for long term use in a community setting. Drawbacks include breakage of the ceramic element, clogging over time, and the inability to meet family potable water needs. Contamination of filtered water can also occur during maintenance or by dispensing water through a contaminated tap (CMWG 2011).

Ceramic Water Filter Manufacturing Process

CWFs are produced by mixing clay and a combustible organic burnout material (e.g., sawdust or corn husks) with water. Filters are formed either by hand, on a potting wheel, or in a press-mold, and then fired in a kiln at high temperature (ca. 900 °C) (Figure 13). Combustion of the burnout material forms small pores that retain microorganisms (bacteria and protozoa) and other contaminants.

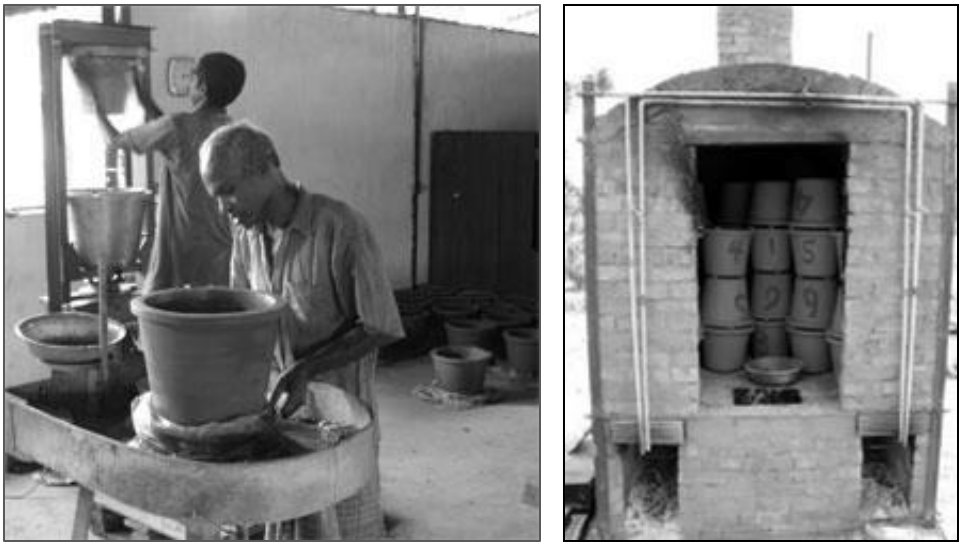

Figure 13. Ceramic filter manufacturing process: forming of filters using a press-mold (left) and filters stacked in a brick kiln (right) (Potters for Peace 2013)

Fabrication of filters is a complicated manufacturing process for a factory in a developing country; the selection of appropriate clay, burnout material, firing profile, and silver application method are all key factors in ensuring effectiveness (CMWG 2011). The clay quality and choice of burnout material directly influence filter strength and pore size distribution, and consequently the microbiological efficacy. The choice of firing temperature profile is also important, as it affects filter strength, chemical composition, and pore structure. Filter drying should be even and consistent to prevent cracks and warping. The typical stages in a firing profile are outlined in Table 1.

Table 1. Typical firing profile for ceramic pot filters (adapted from CMWG 2011)

Stage	Temperature (°C)	Purpose
Water smoking	20-120	Pore water evaporates
Decomposition	120-350	Temperature ramping, up to 100 °C per hour
Combustion	350-450	Combustion of burnout material, important to control this step and raise temperature slowly
Ceramic change	350-700	Clay becomes ceramic, chemically combined water leaves filter and quartz in clay rearranges and sinters together
Burning out (oxidation step)	700-900	Carbon and sulfur in clay are burned out, requires sufficient oxygen and careful control to fully oxidize carbon
Vitrification	800+	Sodium and potassium oxides combine with free silica, strength added to ceramic
Cooling	100	Kiln should be left to cool for 12-24 hours, opened when internal temperature reaches ca. 100 °C

After firing is complete, silver is applied by painting or dipping the filters in colloidal silver or a silver nitrate solution. A small number of factories also apply silver by introducing it to the clay mixture prior to firing (CMWG 2011). Silver nanoparticles represent a small fraction of the total cost of CWFs (about $0.20 per $5-20 filter) (Rayner 2009). Approximately 83% of factories surveyed by Rayner (2013) report using colloidal silver, while 17% use $AgNO_3$, presumably because it is cheaper and/or locally available. Most factories obtain colloidal silver stabilized with casein from Argenol Laboratories in Spain in either liquid or powder form (CMWG 2011). The amount of silver applied to filters varies by factory;

concentrations applied with the brushing technique typically range from ca. 100 to 300 mg/L. When filters are submerged in silver solution, factories typically prepare a 200 mg/L solution in a soaking tub (CMWG 2011).

There is currently no standard recipe or operating procedure for manufacturing of ceramic filters or for the application of silver, and establishing quality control standards in decentralized production facilities remains a major challenge of ceramic filter projects (CMWG 2011). A minimum flow rate when the filter is full of water (between 1 and 2 L/hr) is the sole design criterion, other than the physical dimensions of the ceramic filter (Oyanedel-Craver and Smith 2008; CMWG 2011). Prior to flow rate testing, most factories soak the filters for 2-24 hours. A small number of factories also perform regular microbiological testing, such as plate counts. Manufacturing and safety practices are widely varied, and filters produced different factories can have different characteristics. Only limited data are available regarding the link between specific manufacturing practices and filter quality (CMWG 2011). In addition, there is little information on the influence of different production variables on filter characteristics. For example, the quality of water used for production and flow rate testing is highly variable – contaminated water could leave behind residual toxins that could potentially leach into filtered water (CMWG 2011).

Silver Dissolution Kinetics

One particular concern in the filter manufacturing process is the application of silver and the release of ionic or colloidal silver over the filter lifetime. Leaching

of silver from a filter may lead to undesirable health effects for users and a reduction in disinfection efficiency. In the case of dissolvable nanoparticles such as nAg, it is important to understand the behavior of both the particulate and dissolved forms in porous media systems, including ceramic filters. The form of silver released from filters could have implications related to disinfection performance, as the biological activity of nAg results primarily from release of silver ions, with the degree of nAg dissolution correlated with antimicrobial activity (Tolaymat et al. 2010; Choi et al. 2008).

During silver oxidation, protons and dissolved oxygen are required for dissolution to occur.

$$Ag_{(s)} + \frac{1}{4}O_2 + H^+_{(aq)} \leftrightarrow Ag^+_{(aq)} + \frac{1}{2}H_2O \quad (23)$$

The dissolution reaction can be complicated by particle aging that results from the formation of a silver oxide coating (Ag_2O_3), which then dissolves to slowly to release Ag^+ over time (Li et al. 2012; Chen et al. 2006; Schmidt et al. 2003). Li et al. (2012) provide a schematic representation of the oxidation/dissolution process (Figure 14).

$$Ag_{(s)} + \frac{1}{4}O_2 \rightarrow \frac{1}{2}Ag_2O_{(s)} \quad (24)$$

$$Ag_2O_{(s)} + H_2O \rightarrow 2OH^- + 2Ag^+ \quad (25)$$

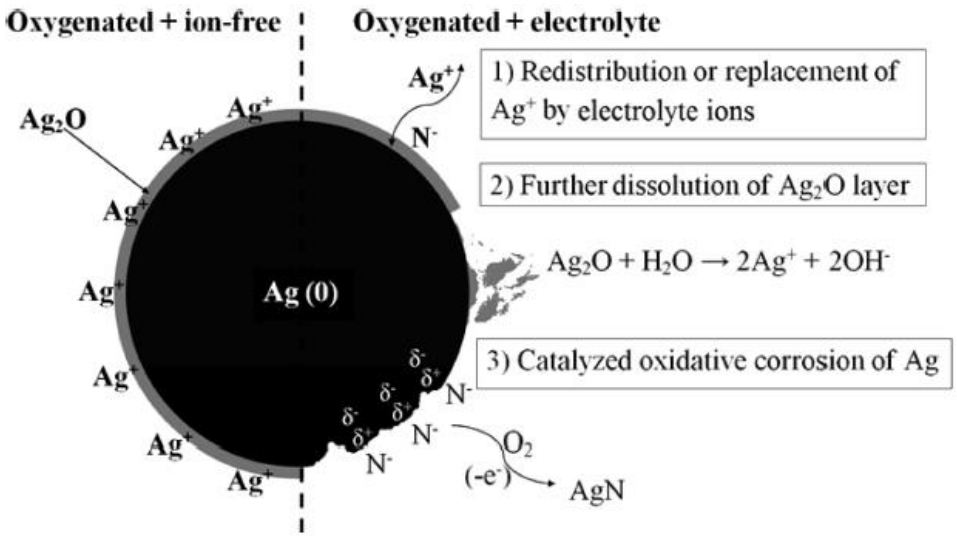

Figure 14. Schematic representation of surface oxidation of nAg and dissolution of the oxide layer (Li et al. 2012).

Recent research pertaining to nAg fate in aqueous systems has focused on assessing dissolution kinetics as a function of solution chemistry in batch reactors (Zhang et al. 2011a, 2011b; Li et al. 2010; Kittler et al. 2010; Liu and Hurt 2010). These studies demonstrated that nAg dissolution rates are dependent on pH, temperature, ionic strength, coating type, initial concentration, initial particle size, electrolyte type and organic matter content. For example, in a batch dissolution study with citrate-coated nAg, Liu and Hurt (2010) observed an increase in Ag^+ release with decreasing pH (Figure 15), consistent with the overall silver oxidation reaction (Eq. 23).

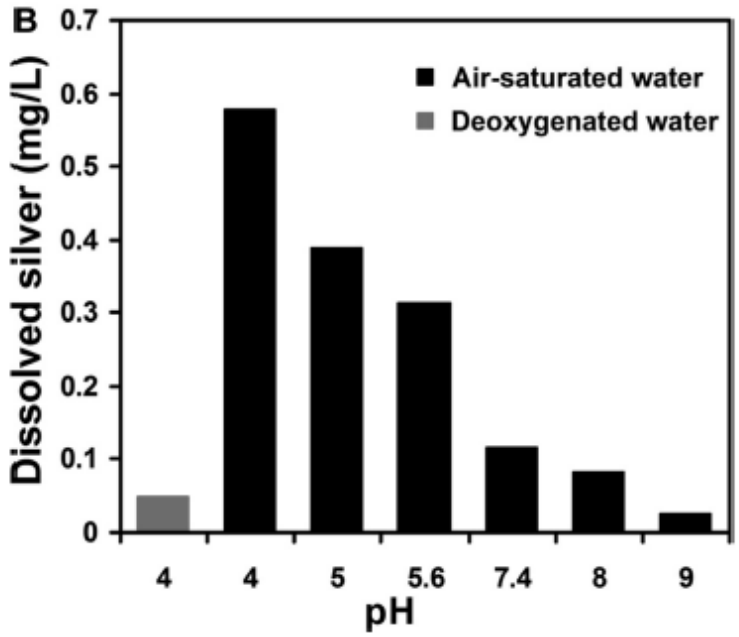

Figure 15. One day release of Ag^{+} as a function of pH in buffered, air-saturated solutions at 20°C (initial concentration = 2 mg/L) (Liu and Hurt 2010)

Certain water properties can inhibit nAg dissolution and reduce the antibacterial effectiveness of nAg. For example, the presence of divalent cations such as calcium and magnesium can cause particles to aggregate and reduce antimicrobial activity (Zhang et al. 2009). Natural organic matter, including humic acids can coat particle surfaces, thereby reducing dissolution reactions and preventing physical interaction between nAg and microorganisms (Zhang et al. 2012; Liu and Hurt 2010).

In previous nAg dissolution studies, a modified first order rate model was used to describe nAg dissolution (Liu and Hurt 2010; Kittler et al. 2011; Li et al. 2012).

$$y(t) = y_{final}[1 - \exp(-kt)] \quad (26)$$

where *y(t)* is the concentration of silver ions in time, y_{final} (mg/L) is the final concentration of released silver ions and *k* is the dissolution rate constant (1/h). Model fits (using Eq. 26) to time release data (Ag^+ release over 48 hr) obtained from citrate-coated nAg solutions at two different initial concentrations are shown in Figure 16 (Kittler et al. 2010).

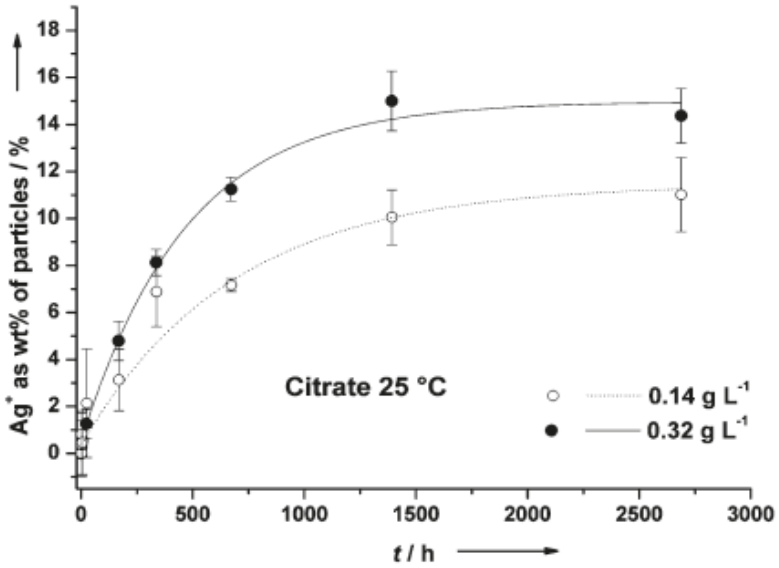

Figure 16. Release of Ag^+ from citrate-coated nAg at two different initial concentrations. Modified first order model predictions yielded rate constants of 0.0021 h^{-1} and 0.0017 h^{-1} for 0.32 g/L and 0.14 g/L of initial nAg content, respectively (Kittler et al. 2010).

Values for y_{final} and *k* were obtained using a non-linear least squares fitting routine. Although more mechanistic kinetic models of nAg dissolution are preferred, this type of approach allows for an assessment of the effect of experimental variables on dissolution rates.

Microbiological Effectiveness of Filters

The removal of microorganisms in CWFs containing nAg is achieved through three mechanisms: retentive sorption due to pore size exclusion, physical-chemical sorption of bacteria and protozoa to the ceramic surface, and the bactericidal action of silver. Colloidal silver has been shown to improve the microbial removal effectiveness of CWFs (Oyanedel-Craver and Smith 2008), inhibit biological growth within filters and plastic receptacles, and reduce the potential for filter clogging (Oyanedel-Craver and Smith 2008; Bloem et al. 2009). In order to conform to safe drinking water standards prescribed the WHO, drinking water must contain less than 1 *E. coli* CFU per 100 mL sample. Low-risk water contains less than 10 CFU/100mL, intermediate risk 10-100 CFU/mL, and high risk 100+ CFU/mL (WHO 1997).

Several studies have evaluated the microbiological effectiveness of CWFs in field and laboratory settings. In a study by Roberts (2004), field tests with 1000 ceramic filters in Cambodia showed that 99% of filters produced water in the low-risk range (< 10 CFU/100mL) after 1 year of use. Another field study in Cambodia found that water samples from 80 household filter users contained 95.1-99.99% lower *E. coli* counts compared to non-filter users (Brown et al. 2007). Forty percent of filtered water samples treated with these filters conformed to WHO guidelines for safe drinking water and the remainder fell under the low risk classification. A study by Johnson et al. (2008) in Ghana found that filters containing nAg reduced *E. coli* in feed water by 99.7%, with average *E. coli* counts falling within the low-risk range. In terms of actual health outcomes for

filter users, Brown et al. (2008) report that filter use in Cambodia resulted in a 49% reduction in diarrheal episodes when compared with non-filter users, and filter users in households in Ghana reported 70% fewer episodes of diarrheal diseases (Johnson et al. 2008).

Kallman et al. (2011) evaluated the performance of ceramic water filters impregnated with nAg using laboratory tests and field studies within a Guatemalan community. Experiments were conducted to determine the effects of sawdust content used in filter manufacturing on the transport and removal of *E. coli*. Disks of varying porosity (20-45%) were submerged in an 800 mg/L colloidal silver solution for 45 seconds and the uptake volume of the silver solution was recorded for each disk. Consistent with previous findings, the authors reported that a higher porosity (higher sawdust content) results in higher bacterial removal. In the field study with full-sized filters containing nAg, the average percent reduction of total coliforms and *E. coli* from influent water was 87% and 92%, respectively.

Bielefeldt et al. (2010) evaluated the removal performance of full-size filters for particles in the size range of 0.02 to 4.5 micron using carboxylate-coated polystyrene fluorescent microspheres, natural particles and clay. The study used filters from a Potters for Peace factory in Nicaragua that had been subjected to several years of either laboratory or field use. Microspheres ($10^4 – 10^{10}$ #/mL) were spiked into dechlorinated tap water and poured into the filters. Particle removal efficiency generally increased with increasing particle size, and was greater than 95% for most sizes. The removal efficiency of virus-sized 0.02 and

0.1 µm spheres was highly variable (ca. 0.8 - 2.5 log removal or 85.0 – 99.7%) among the different filters tested, suggesting that filters are not a reliable method of virus removal (Bielefeldt et al. 2010). It should be noted that the study was limited by a small sample size (n = 6) and a lacked replicate filter experiments.

Several studies have evaluated bacterial transport and removal by ceramic filters in controlled laboratory studies with cylindrical filter disks. Oyanedel-Craver and Smith (2008) compared *E. coli* transport in disks produced from commercial pottery clay or natural clay sourced from Guatemala or Mexico, and treated with colloidal silver either by brushing or submerging. Tracer experiments conducted on selected filters before and after silver application did not show any significant differences in flow characteristics (e.g., dispersion coefficient). Bacterial transport data for CWFs without silver showed that steric rejection or size exclusion chromatography is the primarily removal mechanism for microorganisms. Filter disks without silver removed 97.86–99.97% of *E. coli*, with disks comprised of smaller pores showing a higher rejection of bacteria. Colloidal silver treatment was shown to improve filter performance to greater than 99.99% *E. coli* removal (an additional log reduction can significantly reduce risk for filter users, especially when water contains microorganisms with a low minimum infective dose, such as *Shigella*, *Cryptosporidium* or *Campylobacter*). Minimal differences in *E. coli* reduction were found between the paint and submerge methods of silver application.

Rayner et al. (2013) also evaluated the bacterial removal performance of ceramic filter disks painted with different concentrations of nAg or Ag^{+} and found that

disks impregnated with either nAg or Ag^+ resulted in similar bacterial reductions when the same total silver concentration was applied. Filters containing 0.03 and 0.3 mg/g of silver showed high microbial removal efficiency (4-6 log reduction), but filters containing the lower amount of silver (0.003 mg/g) did not produce water of significantly better quality when compared with control filters (no applied Ag). The effect of silver on microbial removal efficiency appears to depend primarily on the mass of silver than remains in the filter following the water saturation period, rather than the method of application or the type of silver (Lantagne 2011).

Silver Fate and Transport in Filters

Several laboratory and field studies have evaluated the fate of silver in CWFs following painting, dipping, or firing-in of either nAg or $AgNO_3$. In general, silver concentrations measured in filter effluent samples fall below 0.1 mg/L after 8-24 hours of flushing with de-ionized (DI) water or a buffer solution (Bielefeldt et al. 2009; van Halem 2009; Oyanedel-Craver and Smith 2008; Rayner et al. 2013a; Ren and Smith 2013). For example, Rayner et al. (2013) evaluated silver release from ceramic disks manufactured from different clays and burnout materials and found that silver effluent concentrations dropped below the US EPA standard after 24 hours. Higher concentrations of silver were measured in effluent samples from disks coated with higher concentrations of silver (i.e. 0.3 vs. 0.03 mg/g) and for disks coated with Ag^+ compared with nAg. The filter disks were also found to retain nAg more efficiently than Ag^+, and desorption of silver from nAg and Ag^+ disks ranged from 5-10% and 10-40% of the total applied mass,

respectively. The same study found that variations in influent water characteristics (buffer alone, 5 mg/L humic acid, 150 mg/L Na^+ or 150 mg/L Ca^{2+}) resulted in small differences (5-10%) in the percent of silver retained in nAg-coated disks after 24 hours of use. Silver effluent data for Tanzanian/sawdust filters painted with nAg and saturated with a 10% phosphate buffer solution are shown in Figure 17. Here, the authors report total silver concentration, equivalent to Ag^+ plus nAg.

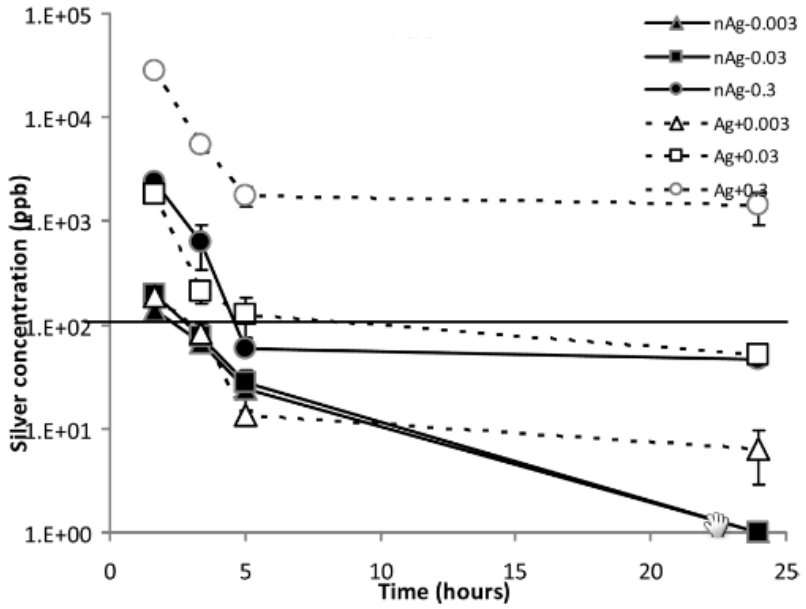

Figure 17. Silver release from ceramic filter disks (Tanzanian clay) coated with different concentrations (mg/g) of either nAg or Ag^+. The horizontal line represents the US EPA drinking water limit of 1ppb for silver (Rayner et al. 2013).

Ren and Smith (2013) present research on nAg transport in ceramic porous media, with a focus on the effects of nAg size, coating type, flow rate and ionic strength on effluent silver concentrations. In transport experiments, a pulse injection of nAg was introduced into silver-free filter disks and effluent silver concentrations

were monitored over time to generate breakthrough curves. These types of experiments (as opposed to release experiments after silver painting) can provide insight into flow conditions and attachment-detachment processes in porous media. The authors observed that citrate-coated nAg were slightly less mobile (5% more retained in disks) than proteinate-coated nAg, and that nAg retention increased with increasing ionic strength, increasing nAg diameter and decreasing flow rate (Figure 18).

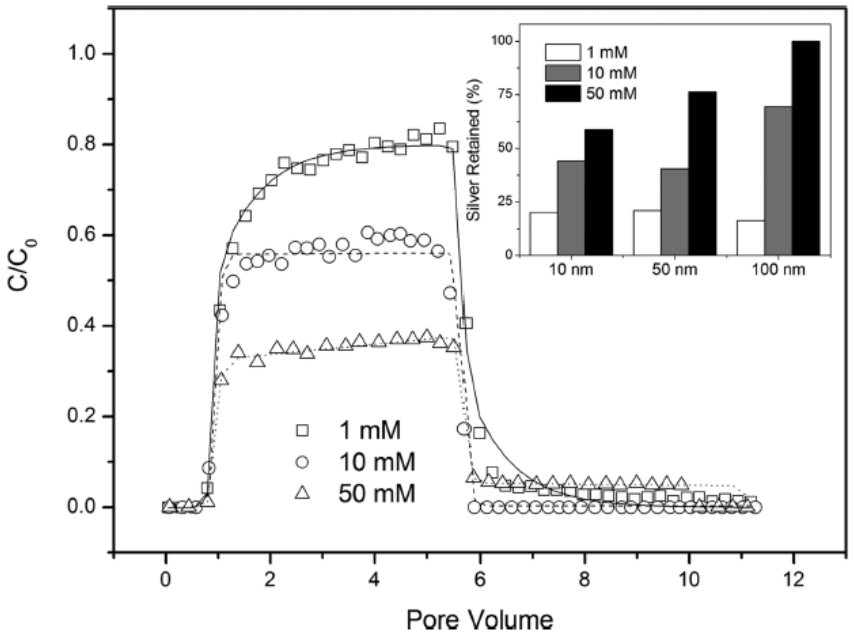

Figure 18. Effluent breakthrough curves obtained for pulse injections of nAg into ceramic filter disks at different ionic strengths. Inset shows the effect of mean nAg particle size on the percentage of nAg retained within the filter (Ren and Smith 2013)

The asymmetrical shape of the breakthrough curves indicates maximum retention capacity behavior, and tailing at later times may indicate either nAg detachment

or dissolution of nAg retained in the ceramic disk (only total silver concentrations were reported). From the inset of Figure 22, transport experiments conducted with different mean particle sizes (10, 50 and 100 nm) indicate that larger nAg are more easily retained by filters, particularly at higher ionic strengths.

The application of silver to filters, either as nAg or as $AgNO_3$, leads to both benefits and concerns. Although silver released into the treated water may provide additional disinfection properties during water storage, the potential release of ionic or particulate forms of silver may lead to undesirable health effects for users and a reduction in filter disinfection efficacy. Both the particulate (nAg) and dissolved ion (Ag^+) forms have been shown to exhibit antimicrobial effects. Toxicity of nAg has been attributed to the pitting action of the small particles on cell membranes (Navarro et al. 2008) and the disruption of cellular metabolism by silver ions (Morones-Ramirez et al. 2013; Li et al. 2010). WHO guidelines stipulate that silver levels up to 0.1 mg/L can be consumed by humans without adverse health effects (WHO 2011), consistent with the US EPA secondary standard for silver in drinking water of 0.1 mg/L (US EPA 2014).

The quality of source waters used with CWFs can vary widely, particularly in areas with underdeveloped treatment and distribution systems and in drought-prone regions which can experience large seasonal variations in groundwater. A limited number of studies have examined the impact of different water chemistries on silver fate in filters (Rayner et al. 2013a, Ren and Smith 2013; Bielefeldt et al. 2013), and shown that pH, ionic strength, dissolved organic matter, and chlorine content can influence silver retention. No studies to date have

examined the impact of transient water chemistry on silver retention, the mechanism of silver transport and release (e.g., nanoparticle detachment, dissolution, or cation exchange) under different influent chemistries, or consistently distinguished between Ag^+ and nAg particles in effluent samples.

CHAPTER 3: MATERIALS AND METHODS

Nanomaterials

Iron oxide nanoparticles (magnetite, Fe_3O_4) were synthesized by the Fortner group at Washington University at St. Louis (WUSL). Particles were coated with oleic acid, a non-ionic, negatively-charged surfactant. Magnetite nanoparticles (nMag) were synthesized via controlled thermal decomposition of iron carboxylate salts in the presence of oleic acid. This method produced particles that were highly uniform in size (e.g., spherical 16 nm particles with <10 nm size distribution).

Nanoscale fullerene (nC60) nanoparticles were prepared using previously developed methods (Wang et al. 2008, 2012; Fortner et al. 2005; Deguchi et al. 2001). Briefly, tetrohydrofuran (THF) was sparged with high-purity nitrogen and saturated with excess fullerene powder. The solution was filtered through a 0.22 um nylon membrane (Osmotics Corp., Minnetonka, MN). An equal volume of DI water was added to 250 mL of rapidly stirring C60-THF solution at a rate of 1 L/min. The resulting solution (1 L after two cycles) was poured into a round bottom flask and loaded onto a rotary evaporator (Rotovapor Model R210, Buchi, New Castle, DE). THF removal was accomplished by heating at 75 – 80 °C and three evaporation/dilution steps. The resulting suspension (ca. 500 mL) was vacuum filtered through a 0.45 um cellulose acetate membrane (Corning Inc., Corning, NY). To remove residual THF, three water exchange cycles using a pressurized stirred cell (Amicon Model 8200, EMD Millipore) fitted with a

regenerated cellulose membrane (10 kDa NMWL, EMD Millipore) were conducted. This method produced a ca. 5.8 mg/L (total carbon basis) suspension. The mean diameter (intensity-weighted) and zeta potential of nC_{60} in suspensions buffered to pH 7.0 with 0.065 M $NaHCO_3$ were 92 ± 0.5 nm and -52.0 ± 1.9 mV, respectively.

For ceramic filter experiments, casein-coated silver nanoparticles (nAg) were obtained from Argenol Laboratories (Spain) in powder form (71-75% silver by weight). Argenol nAg have a mean diameter of ca. 45 nm as determined by TEM (Kallman et al. 2012).

Porous Media

Column transport experiments were conducted with Federal Fine Ottawa sand. Ottawa sand is a round grain silica sand that contains >99.5% SiO_2 and relatively low levels of iron and aluminum oxides (<0.05%) and manganese oxide (<0.008%). Federal Fine was obtained from U.S. Silica (Frederick, MD), sieved to obtain the 40-50 mesh size fraction, and then acid-washed following the methods of Wang et al. (2008). Briefly, sand was soaked overnight in 1 M HNO_3, rinsed with DI water to achieve a pH > 5, and ultra-sonicated in DI water until the solution was visually clear.

Glass beads (40-50 mesh, soda lime glass) from AGSCO Corporation (Wheeling, IL) were used for some column experiments with nMag due to relatively high and variable background iron levels in Ottawa sand which interfered with solid phase analysis. Glass beads were thoroughly cleaned using a series of solvent and acid

washes (Wang et al. 2008). Beads were sequentially rinsed with acetone, hexane, and DI water, and then ultra-sonicated for 20 min each in baths containing 1M HNO_3, 0.1 M NaOH, and DI water.

Ceramic Material

Ceramic filter disks (11.5 cm diameter x 3.8 cm thickness) were obtained from Advanced Ceramics Manufacturing (Tucson, AZ). A cylindrical filter design was chosen to simplify the geometry relative to the pot shape and facilitate one-dimensional transport experiments. Clay for disks was imported from a ceramic filter factory in Tanzania, and pine sawdust was purchased from Pallet Recyclers (Tucson, AZ). Sawdust was sieved through US number 30 and 60 sieves prior to mixing with clay; the ratio of clay to sawdust was approximately 4%. Disks were formed using a hydraulic press and then fired to 950°C in a brick oven kiln followed by a 60 minute soak to saturate. All disks had flow rates that fell in the range of 1.3-2 mL/min (this range translates to a flow rate of approximately 2-3 L/hr for a full sized filter).

Disks received from Advanced Ceramic Manufacturing were reduced in size to 5.1 cm in diameter using a hole saw in order to fit existing filter holders obtained from Vinka Craver's lab at the University of Rhode Island. Prior to use in transport experiments, disks were heat-treated for 30 minutes at 550°C to remove any residual organics. High pressure mercury porosimetry (Micromeritics, Norcross, GA) were used to determine the porosity and pore size distribution of

the ceramic matrix. The average porosity and pore volume of the filter disks (n=4) were 0.53 and 16.2 mL, respectively, based on gravimetric measurements.

UV Exposure Studies

Aqueous nMag suspensions were aged at WUSL and then shipped overnight to Tufts for use in next-day column transport experiments. Light exposure experiments were conducted in a variable intensity, fan cooled photoreactor equipped with interchangeable bulbs (UVB, 280-175 nm, Fortner lab). To control the extent of aging, nMag solutions were buffered with phosphate and exposure time was limited to 3 days.

UV light exposure studies with nAg were conducted in a fan-cooled photo-reactor (LZC-4X, Luzchem Research, Gloucester, ON). The photo-reactor was operated at an intensity of ca. 2.5 mW/cm^2, typical of sea level solar radiation exposure in Boston, MA (42.3 °N), using combinations of top and side irradiation from eight-30.5 cm lamps. UVA and UVB lamps had spectral bands centered at 350 nm and 300 nm, respectively, and were rated at 8 Watts each. Fused quartz 50 mL Erlenmeyer flasks (Technical Glass Products, Painesville, OH) were used in place of borosilicate glassware to achieve maximum UV light transmittance (> 90%). Flasks containing a total Ag concentration of 3 mg/L (zero ionic strength) were prepared in triplicate by combining 2.7 mL of nAg stock with 42.3 mL DI water, and adjusting the pH to 7.00 ± 0.05 with dilute NaOH or HNO_3. The flasks were placed on a rotary platform shaker (DOS-20S, ELMI, San Diego, CA) operated at 80 rpm to ensure uniform mixing and light exposure. Dark control flasks (denoted

as “fresh”) were prepared under identical conditions and wrapped in aluminum foil in the photo-reactor. Batches were sampled daily and characterized by DLS and UV-vis and analyzed for total and dissolved silver content.

Column Transport Experiments

Transport experiments were conducted in borosilicate glass columns (12.5 cm length x 2.5 cm inside diameter) packed with dry sand or glass beads and saturated with background electrolyte solution following the methods of Wang et al. (2008). Nanoparticle solutions were prepared in the following order: electrolyte addition, nanoparticle stock addition and pH adjustment using dilute hydrochloric acid or sodium hydroxide. Prior to nanoparticle introduction, a non-reactive tracer test was conducted for each column experiment. Three pore volumes of NaBr was introduced (at the same ionic strength as background electrolyte in transport experiment), followed by 3 pore volumes of background electrolyte. Effluent samples were collected using a fraction collector (CF-2, Spectrum Laboratories) and analyzed for bromide concentration. The CXTFIT program (ver. 2.0, Toride et al. 1995) was used to determine the hydrodynamic dispersion and pore volume for each column tracer test. Bromide BTC’s were fit to the dimensionless form of the advective-dispersive transport equation:

$$R_F \frac{\partial C^*}{\partial PV} = \frac{1}{Pe}\frac{\partial^2 C^*}{\partial X^2} - \frac{\partial C^*}{\partial X} \qquad (27)$$

$$R_F = 1 + \frac{K_D \rho_b}{\theta_w};\ C^* = \frac{C}{C_0};\ PV = \frac{v_p t}{L};\ Pe = \frac{v_p L}{D_H};\ X^* = \frac{x}{L} \qquad (28)$$

where R_F is the solute retardation factor (fixed at 1.0 for a non-reactive tracer), ρ_b is the bulk density of the matrix, C is the aqueous concentration, C_0 is the influent or applied aqueous concentration, PV is the dimensionless pore volume, v_p is the pore-water velocity, t is time, L is the length of the domain in the direction of flow (i.e., filter disk thickness), Pe is the Peclet number, D_H is the hydrodynamic dispersion coefficient, X^* is dimensionless distance, and x is the distance parallel to flow.

Following the tracer test, a three pore volume pulse of nanoparticle suspension (ca. 5 mg/L) was introduced into each column, followed by 3 pore volumes of nanoparticle-free solution (identical chemical conditions to the injection suspension). A syringe pump was used to deliver both the nanoparticle solution and background electrolyte to the column in upflow mode at a flow rate of 1 mL/min. This flow rate corresponded to a pore-water velocity of ca. 7.6 m/d, and provides a column residence time of ca. 25.5 minutes. The influent solution was sampled at the beginning and conclusion of the pulse injection and analyzed for metal concentration, particle size, and zeta potential. Effluent samples were collected continuously at a resolution of 5 samples per pore volume and analyzed for total and/or dissolved metal content to generate effluent breakthrough curves (C/C_0 vs. dimensionless pore volume). At the conclusion of each column experiment, the columns were dissected into 1.25 cm increments. Each section was homogenized by vortexing for 30 seconds, after which a 5g aliquot was analyzed to quantify solid-phase concentrations along the length (retention profile) using methods described previously.

Existing mathematical models (e.g., Li et al. 2008) were used to derive attachment parameters from column breakthrough and retention data. Parameters were used to quantitatively describe the impact of solution chemistry, porous media, and aging on transport and retention behavior.

QCM-D Experiments

QCM-D experiments were conducted with three different nanoparticle systems (silver, fullerene, and iron oxide) in order to compare deposition behavior in corresponding sand column experiments. QCM-D studies were conducted by the Fortner group at WUSL using a Q-Sense E4 unit (Q-Sense AB, Sweden). Deposition data was collected by simultaneously monitoring changes in frequency and dissipation of a 5 MHz silica or 5 MHz polystyrene-coated QCM-D crystal at room temperature (22.00 ± 0.02 °C). Deposition rates measured in QCM-D experiments were scaled by the specific surface area (area exposed to flow/volume of fluid) of different porous media. The QCM-D deposition rate (Hz t^{-1}) was obtained by monitoring the rate in frequency shift at the third overtone.

Ceramic Filter Experiments

Prior to silver application, the ceramic material was characterized through pore size distribution analysis, non-reactive tracer tests, and cation exchange capacity (CEC) experiments. DLVO theory calculations were performed to qualitatively predict how changes in solution chemistry may influence nAg attachment and detachment behavior in the ceramic. After silver application, silver release was

quantified in disks treated with different application methods and exposed to variable influent water chemistries. These data were analyzed to predict the lifetime of the silver application under different source water compositions.

Disk Fabrication and Pore Size Distribution

Ceramic disks (~10-cm diameter, 1.5-cm thick), manufactured by Advanced Ceramics Manufacturing (ACM, Tucson, AZ), were used to facilitate one-dimensional transport experiments. Clay was imported from a Tanzanian factory and pine sawdust was purchased from Pallet Recyclers (Tucson, AZ). Sawdust was sieved between US no.30 and no.60 mesh (0.595- and 0.251-mm openings, respectively) sieves before mixing with clay. The mass ratio of sawdust to clay was ~4%, which provided an initial flow rate equivalent to 2-3 L/hr in a full-sized filter. Disks were formed using a hydraulic press and fired to a temperature of 900°C. Upon receipt from ACM, disks were reduced to 5.1-cm in diameter using a hole saw blade to fit existing holders.(Oyanedel-Craver & Smith 2008)

Porosity and pore size distribution of fragments from two disks were measured in duplicate using mercury intrusion porosimetry (MIP) (Micromeritics Instrument Corp., Norcross, GA). Before placement in holders, disks were sterilized by heating at 550°C for 30 min. After cooling, disks were placed in modified polycarbonate membrane holders (Model 420400, Whatman, UK),(Zhang et al. 2012) and sealed with silicone and neoprene O-rings (McMaster-Carr, Elmhurst, IL) at disk top and bottom to ensure influent solutions flowed vertically.

Water Flow and Modeling

Two non-reactive tracer tests were performed on water-saturated disks to confirm the total pore volume (PV), characterize water flow and hydrodynamic dispersion in each disk, and evaluate variation in disks from the same batch. Filters were saturated with a minimum of 30 PV of pH 7 10mM $NaNO_3$ electrolyte solution prepared with degassed DI water. A pulse of either 0.1 or 3.7 PV of non-reactive tracer solution (10mM NaBr, pH 7) was introduced using a syringe pump operated at 0.6 mL/min; this corresponds to a pore-water velocity of ~1 m/d, and a CWF flow rate of ~3.6 L/hr. After bromide injection, disks were flushed with 6 PV of pH 7 10mM $NaNO_3$. Effluent samples were collected every 5-7 minutes in 15-mL polypropylene vials (VWR, Radnor, PA) using a Spectrum CF-2 fraction collector (Spectrum Laboratories, Houston, TX). Bromide concentrations were measured using an ion-specific probe (Cole Parmer, Vernon Hills, IL). The detection limit for bromide was determined to be 0.02 mg/L based on the method of Hubaux and Vos.(Hubaux & Vos 1970) After tracer tests, disks were removed from holders and dried at 35°C for 12 hr.

The CXTFIT program was used to simulate effluent BTC data and determine the fraction of pore space available for flow (mobile water). To account for non-equilibrium mass transfer processes, the solute transport equations (Eq. 27) can be reformulated to include a “two-site” model that describes rate-limited chemical reactions (e.g., adsorption-desorption) or a “two-region” model that accounts for physical mass transfer limitations (e.g., solute diffusion between regions of mobile and immobile water) (Gamerdinger & Wagenet 1989; van Genuchten &

Wagenet 1989). In the case of physical nonequilibrium due to diffusional mass transfer of a non-reactive solute between regions of mobile and immobile water, the following dimensionless parameters β and ω, are incorporated into the analytical solution for Eq. 27:

$$\beta = \frac{\theta_{w,m} + f\rho_b K_D}{\theta_w + \rho_b K_D} \qquad (29)$$

$$\omega = \frac{\alpha_1 L}{\theta_{w,m} v_{p,m}} \qquad (30)$$

In Eq. 29, $\theta_{w,m}$ and θ_w represents the mobile and total volumetric water content, respectively, while f refers to the fraction of solid phase in contact with mobile water. For a non-reactive tracer, the value of $K_D = 0$, and β reduces to $\theta_{w,m}/\theta_w$ or simply the fraction of mobile water.

Thus, when the value of β approaches 1 all of the pore water is considered to be "mobile," whereas, when the value of β approaches 0 all of the pore water is considered to be "immobile." In Eq. 30, α_1 represents the first-order mass transfer rate between mobile and immobile water, and $v_{p,m}$ is the velocity of the mobile pore water.

Cation Exchange Capacity

The CEC of the disk material was determined using both crushed and intact disks. A disk segment was crushed using an agate mortar and pestle and CEC was determined using the methods of Pennell.(Pennell et al. 1991) Approximately 0.5-

g of crushed material was added to a 50-mL polypropylene centrifuge tube (VWR, Radnor, PA), washed five times with 200-mL of 1M $CaCl_2$ to saturate the negatively charged exchange sites with Ca^{2+}. Tubes were placed on a LabQuake shaker (ThermoScientific, Waltham, MA) for 5 min to disperse the crushed material, mixed for 30 s using a vortex mixer, and centrifuged at $1500 \times g$ for 5 min. The supernatant was decanted and discarded, and samples were washed five times with 95% ethanol to remove excess salt. Exchangeable Ca^{2+} was extracted by washing samples with 10-mL of 0.5M $Mg(NO_3)_2$ solution following the procedure above; supernatant was composited in a 100-mL volumetric flask, diluted with deionized (DI) water, and analyzed for Ca^{2+}.

Concentrations of Mg^{2+} and Ca^{2+} in aqueous samples obtained from the CEC experiments were analyzed by inductively-coupled plasma-optical emission spectroscopy (ICP-OES) (7300 DV, Perkin Elmer, Waltham, MA) in axial view mode. Samples were introduced without further modification through a cross-flow nebulizer at 0.5 mL/min, and Mg and Ca were detected at wavelengths of 279.07-nm and 317.93-nm, respectively.

CEC of the intact disk was tested by introducing 25 PV of 1M $Ca(NO_3)_2$ to saturate exchange sites with Ca^{2+}, followed by a 10 PV ethanol rinse to remove excess salt, and displacement of bound Ca^{2+} with 60 PV of 0.5M $Mg(NO_3)_2$. Additionally, the disk capacity for Ag^{+} was determined using a similar procedure to intact disk CEC testing, but with $AgNO_3$ instead of $CaCl_2$, and a DI water wash instead of ethanol ($AgNO_3$ is reduced by ethanol to produce precipitates). Silver concentrations were analyzed by ICP-OES (328.068-nm).

Silver Dissolution and Release Experiments

A 200 mg/L (total Ag) silver solution or suspension was prepared as follows: 1) $AgNO_3$ (AlfaAesar, Ward Hill, MA) or casein-coated nAg (Argenol Laboratories, Spain) was diluted in DI water; 2) adjusted to pH 7.00 ± 0.05 using dilute HNO_3 or NaOH; and 3) brushed with 3 mL of silver on each of the top and bottom disk surfaces using a paintbrush with Teflon-coated bristles (Shur-Line, Mooresville, NC). Select silver release experiments were also conducted in which disks were brushed with 6 mL of silver on only the top surface. These application methods result in the currently recommended silver application of 0.03 mg/g (Rayner et al. 2013). Disks were dried at room temperature for 12 hr and re-sealed into holders.

Nine separate disk experiments were conducted to assess the impact of influent water chemistry on silver dissolution and transport in filter disks with $AgNO_3$ or casein-nAg applied to the top and bottom surfaces (Table 1). Each silver release experiment began with 12-15 hr (36-45 PV) of flushing with a pH 7 10mM $NaNO_3$ background solution, followed by the introduction of aqueous solutions of varying pH, IS, and cation species. Filter effluent samples were collected every 30-60 min (18-36 mL per sample) and analyzed for total Ag and Ag^+.

Longevity Analysis

Time to silver depletion was estimated based on the silver mass remaining in the disk (mass applied less cumulative effluent mass) after the initial flushing period (~30 PV) using a constant flow rate of 0.6mL/min under two general conditions: 1) baseline case of pH=7 10mM $NaNO_3$; and, 2) worst or best case concentration

for each chemical condition (e.g., peak concentration at pH=7 50mM $NaNO_3$ or minimum concentration at pH=9 10mM $NaNO_3$). The water volume to silver depletion in disks was converted to full-sized filter volume (10-L capacity) by scaling by surface area exposed to flow and equating pore volumes (i.e., ~12-mL in disk and ~1.2-L in pot). Water volume was converted to years assuming a constant flow rate of 3.6 L/hr and 1 full filter/day.

Analytical Methods

Nanoparticle Morphology and Surface Chemistry

The particle size distribution and electrophoretic mobility (EPM) of nAg suspensions at various IS and pH were measured by dynamic light scattering (DLS) and laser Doppler micro-electrophoresis, respectively, using a Zetasizer NanoZS (Malvern Instruments, UK). All DLS measurements were carried out in triplicate at 25°C with a measurement angle of 173° (backscatter), and a refractive index of 1.330 and viscosity of 0.8872 cP for the dispersant (DI water). The DLS was calibrated using a standard solution of polymer microspheres (Duke Scientific, Palo Alto, CA).

EPM was converted to zeta potential using Henry's Equation and the Smoluchowski approximation, which assumes that the thickness of the electrical double layer is very small compared to the mean diameter of the particles:(Hunter 1981)

$$\xi = U\frac{\eta}{\varepsilon} \qquad (31)$$

where U is the electrophoretic mobility, η is the viscosity and ε is the dielectric constant of the solvent (80.4 for water at 25°C).

The EPM of the ceramic was measured by crushing a disk segment into fine powder with a mortar and pestle and suspending the sample in solution (Ren & Smith 2013) (25g ceramic/L). Fumed silica powder (0.2-0.3 µm, Sigma Aldrich) suspended in solution was used as a surrogate to determine the EPM of the QCM silica sensors. This method was similar to those used by Jiang et al. (2012) and Thio et al. (2011).

Elemental Analysis

Aqueous concentrations of silver and iron were determined by ICP-OES (Perkin Elmer, 7000DV). Graphite furnace-atomic adsorption spectroscopy (GF-AAS) was also used for solution containing metal concentrations below ca. 10 µg/L). The detection limits for the ICP-OES and GF-AAS methods for Ag^+ were 0.09 mg/L and 0.8 µg/L, respectively (Hubaux and Vos 1978). Dissolved silver was separated from nAg by centrifugation at 2500×g in ultrafiltration units (Amicon 3k, Millipore, Billerica, MA).

Aqueous nC_{60} concentrations were determined with UV-vis spectroscopy by scanning over the wavelength range of 190 to 500 nm. The absorbance response at 344 ± 1 nm was used for nC_{60} quantification based on a 5-point calibration curve prepared by serial dilution of a known C_{60} stock solution (9.5 mg/L).

Solid-phase extraction of silver and iron in porous media was achieved through acid digestion procedures described previously (Mittelman et al. 2013). Briefly,

5g of solid sample was digested in 10mL of concentrated nitric acid (15.9 M) at 190°C using a microwave digester unit (SP-D, CEM). The digest was diluted 4X in DI water and then analyzed for metal content by ICP-OES. Fullerene was extracted from sand by sonication in water and UV-vis analysis of extract solutions, following methods described previously (Wang et al. 2012).

Concentrations of Mg^{2+} and Ca^{2+} in aqueous samples obtained from cation exchange experiments were analyzed by inductively-coupled plasma-optical emission spectroscopy (ICP-OES) (7300 DV, Perkin Elmer, Waltham, MA) run in axial view mode. Samples were introduced without further modification through a cross-flow nebulizer at 0.5 mL/min, and Mg and Ca were detected at wavelengths of 279.07 nm and 317.93 nm, respectively.

For the non-reactive tracer tests, bromide concentrations were measured using an ion-specific probe (Cole Parmer, Vernon Hills, IL). The detection limit for bromide was determined to be 0.02 mg/L based on the method of Hubaux and Vos (1978).

CHAPTER 4: EFFECT OF UV LIGHT AGING ON THE MOBILITY AND DISSOLUTION OF SILVER NANOPARTICLES

Introduction

Over the course of their life cycle, engineered nanomaterials will be subjected to various transformation processes, including as photodegradation, passivation by natural organic matter, biodegradation, and oxidation (Lin et al. 2010b). These processes are likely to modify or "age" nanomaterials, resulting in changes to nanoparticle surface properties, which may in turn alter their fate and transport in aqueous systems. The transport of nanomaterials and nanomaterial residues is of interest due to both the potential for water contamination and the need to better understand the performance of filters used in water and wastewater treatment processes (Auffan et al. 2010). Additionally, the breakdown of the protective surface coating and dissolution of the nanoparticle core could lead to the release of toxic byproducts, such as dissolved metal ions and reactive oxygen species.(Lee et al. 2007; Lee et al. 2009)

Previous studies have evaluated the aging of nanoparticles exposed to natural waters (Li & Lenhart 2012; Sarathy et al. 2008; Reinsch et al. 2010), swimming pool water (Virkutyte et al. 2012), organic acids (Mudunkotuwa et al. 2011), clay and dissolved organic matter (Coutris et al. 2012; Scheckel et al. 2010), and ultra-violet light (Auffan et al. 2010; Labille et al. 2010; Gorham et al. 2012; Hou & Jafvert 2009; Jaesang Lee et al. 2009; Cheng et al. 2011; Li & Lenhart 2012). Exposure to sunlight is a particularly interesting aging mechanism, as ultra-violet

(UV) light can catalyze radical reactions, which in turn can cause surface degradation and the production of potentially toxic byproducts. For example, UV light was shown to accelerate degradation of the $Al(OH)_3$-polydimethylsiloxane (PDMS) coating of nano-TiO_2 used in cosmetics, resulting in increased concentrations of Si and Al (Auffan et al. 2010). Hou and Jafvert (2009) found that aqueous nC_{60} clusters, when exposed to sunlight, lost their characteristic yellow-brown color, decreased in size, and released water soluble byproducts. UV light has also been shown to accelerate the oxidative aging of citrate-coated silver nanoparticles (nAg). When nAg were irradiated with UVB light, Gorham (2012) found that the rate of surface plasmon resonance (SPR) loss in UV-vis spectra corresponded to an increase in free citrate concentrations, production of silver ions (Ag^+), and the appearance of a core-shell structure (Ag^0 core/Ag_2O shell).

Several studies have also examined the role that aging plays in nanomaterial toxicity in environmental and biological systems (Mahendra et al. 2008; Phenrat, et al. 2009a; Jaesang Lee et al. 2009; Yang et al. 2011; Song et al. 2010; Cheng et al. 2011). Following aging under acidic or alkaline conditions, Mahendra et al. (2008) observed a significant increase in quantum dot (QD) microbial toxicity due to loss of the organic coating and release of cadmium and selenite ions from the metal core. Lee et al. (2009) found that the toxicity of QDs against the freshwater macroinvertebrate *Daphnia magna* increased in the presence of UV light, which was attributed to the decreasing size of the particles due to coating degradation and dissolution, release of toxic ions, and the generation of reactive oxygen

species. In contrast, Cheng et al. (2011) reported that polymer-coated nAg were less toxic following sunlight exposure due to aggregate formation.

While previous research has demonstrated that nanomaterials exhibit changes in size, surface chemistry, stability, and toxicity following exposure to environmental or biological media, the potential effects of transformations have rarely been accounted for in nanoparticle transport experiments. With the exception of one study by Kim et al. (2009) prior transport studies have utilized freshly prepared suspensions and did not account for aging processes that may occur in the environment. Thus, the objective of this study was to evaluate the transport behavior of citrate-coated nAg in water-saturated sand following exposure to either UVA (320-400 nm) or UVB (280-320 nm) light in a photo-reactor. In a 7 day exposure study, the particle size and surface charge of nAg suspensions were characterized using dynamic light scattering (DLS), changes surface chemistry was evaluated using spectroscopy, and the total and dissolved silver ion content were measured. Transport experiments were conducted with 3-day aged nAg in columns packed with water-saturated 40-50 mesh Ottawa sand at two ionic strengths (10 and 20 mM $NaNO_3$) and at three flow rates (0.5, 1.0, and 1.5 mL/min). Column influent and effluent samples were monitored for total and dissolved silver content and mean particle size, while the solid phase was destructively sampled at the conclusion of each experiment to obtain nAg retention profiles.

Results and Discussion

Exposure of nAg to UVA and UVB light

A series of batch experiments were conducted to investigate the effects of UVA and UVB light exposure on citrate-stabilized nAg (pH 7, zero ionic strength). Over the 7 day exposure period, the mean diameter and zeta potential of fresh nAg (i.e., un-aged control) remained constant at 10.2 ± 0.6 nm and -44.8 ± 1.1 mV, respectively (Figure 19). The diameter of UVA-aged nAg also remained relatively stable, ranging from ca. 9 -12 nm with a slight increase in mean diameter (14 nm) observed on day 7. In contrast, exposure to UVB light produced a much greater effect on the mean diameter of nAg, which increased rapidly from 10 nm to 45.4 ± 0.6 nm after 48 hr, and then slowly increased to 53.8 ± 1.8 nm by day 7 (Figure 19a). The zeta potential of UVA-and UVB-aged nAg steadily became less negative over the 7-day exposure period, approaching values of -30.1 ± 1.1 mV and -26.7 ± 1.2 mV at the conclusion of the batch experiment (Figure 19b). Thus, exposure to both UVA and UVB light resulted in substantial changes in the zeta potential of nAg, while only UVB light yielded a significant increase in mean diameter.

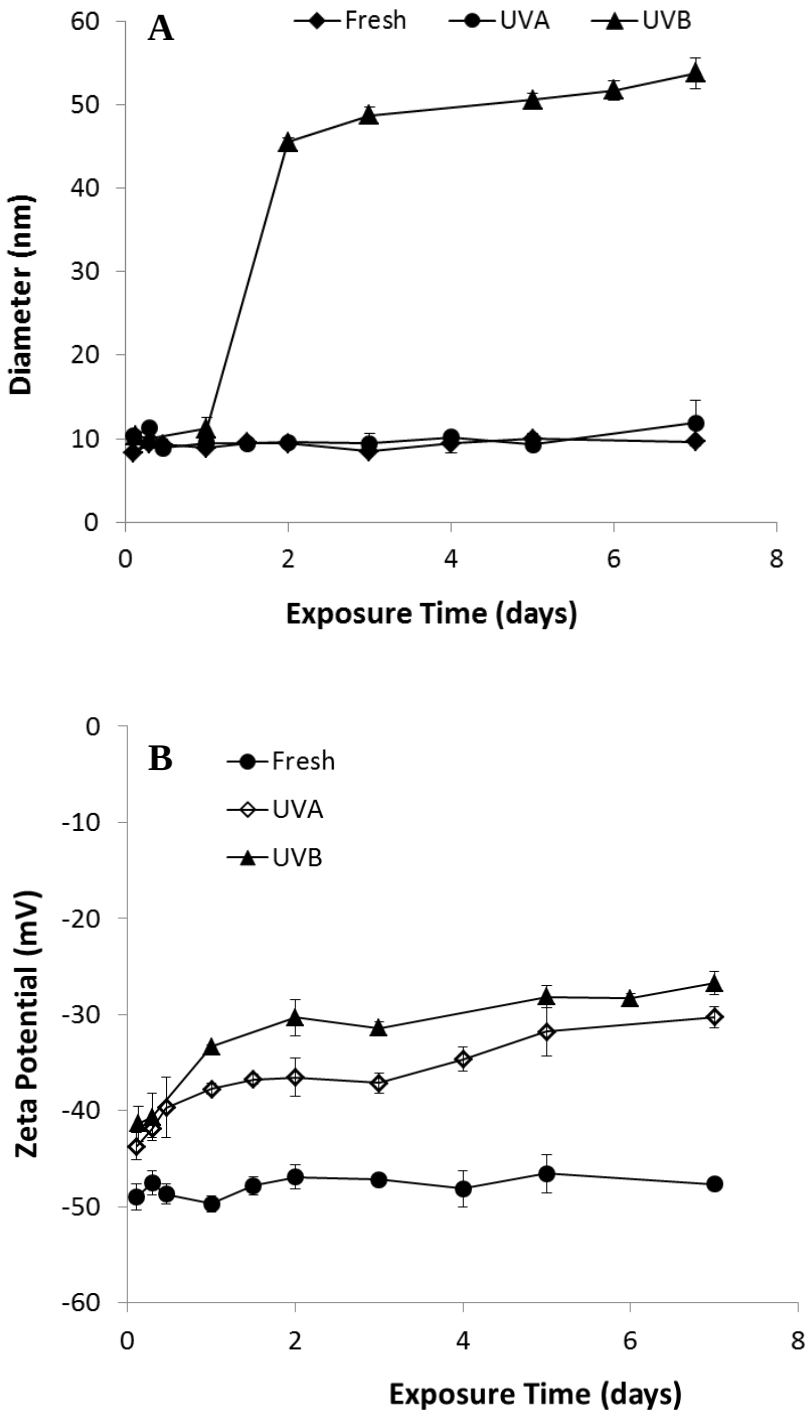

Figure 19. Change in (a) mean diameter and (b) zeta potential of nAg exposed to UVA or UVB light for 7 days. Diameter and zeta potential at time 0 were 9.7 ± 2.1 nm and -44.6 ± 1.4 mV, respectively.

Aggregation kinetic studies were conducted with fresh and UV-aged nAg suspensions containing $NaNO_3$ at concentrations ranging from 5 to 300 mM (pH 7.00 ± 0.05). The critical coagulation concentration (CCC) for each system was determined by accounting for reaction- and diffusion-limited aggregation based on the method of Chen and Elimelech (2006). Plots of attachment efficiency (α) versus $NaNO_3$ concentration (Figure 20) yielded two distinct aggregation regimes, where the extrapolated intersection yields the CCC value. Aggregation of nAg was consistent with behavior predicted by Derjaguin, Landau, Verwey, Overbeek (DLVO) theory.(Derjaguin & Landau 1993; Verwey et al. 1999) The transition to a diffusion-limited regime ($\alpha = 1$) occurred more rapidly in aged suspensions compared with fresh nAg. The resulting CCC values for fresh, UVA- and UVB-aged nAg (3d) were 161.4, 37.8, and 24.1 mM, respectively, indicating that UV exposure significantly reduced nAg stability. CCC values did not follow a specific trend with exposure time (Table 2), suggesting that the most significant impact on nAg aggregation kinetics and attachment efficiency occurred during the initial 24 hr of aging.

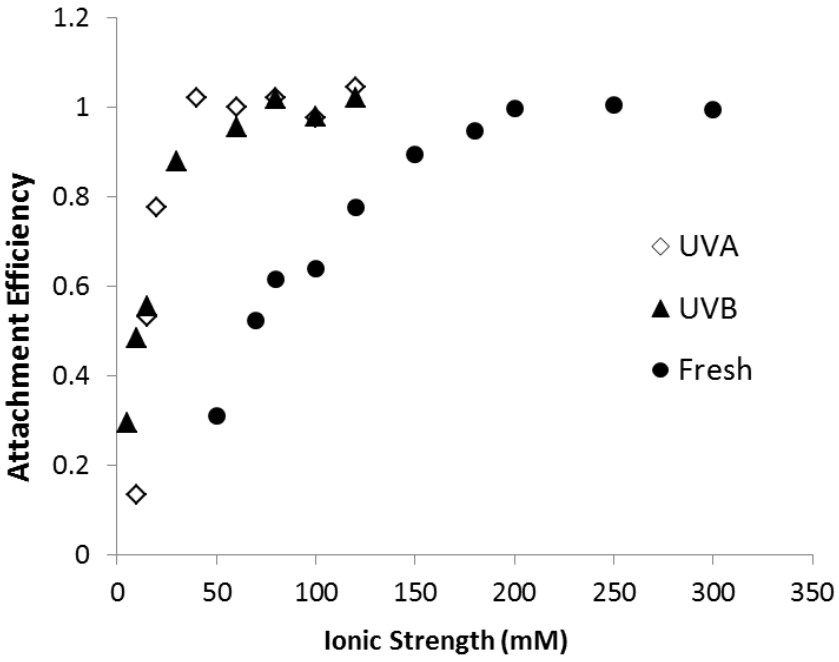

Figure 20. Attachment efficiency as a function of ionic strength for fresh and UV-aged nAg following a 3 day exposure

Table 2. Critical coagulation concentration (CCC) for fresh and UVA- and UVB-aged nAg as a function of exposure time

Aging Time (d)	Fresh CCC (mM)	UVA CCC (mM)	UVB CCC (mM)
1	161.4	37.8	21.4
3	182.4	25.5	15.1
7	175.9	23.8	34.8

UV-vis spectroscopy was used to monitor the growth of oxide layers (Ag_2O) on the particle surface during UV exposure. Results from UV-vis spectroscopy studies revealed evidence of chemical and morphological changes as a result of UVA (Figure 21) and UVB (Figure 22) light exposure. UV-vis spectra for fresh and aged nAg display characteristic peaks in absorbance at ca. 400 nm, consistent

with results from previous nAg batch studies.(Chen et al. 2006; Gorham et al. 2012) UVA and UVB light exposure caused broadening of the spectra, a decrease in surface plasmon resonance (SPR), and 5-6 nm shifts in the peak maximum towards the red region. Changes in spectra of UV-aged nAg are suggestive of oxidative corrosion and consistent with results reported by previous studies (Henglein 1998; Chen et al. 2006; X. Li et al. 2010; Schmidt et al. 2003; Li & Lenhart 2012; Cheng et al. 2011). A decrease in SPR is also characteristic of aggregation (J. Lee et al. 2007; X. Li et al. 2010) and the decrease in SPR over 7 days observed for UVB-aged suspensions (ca. 0.2 absorbance units) coincided with an increase in particle diameter (ca. 40 nm).

The UVA and UVB wavelengths used to age nAg overlap with the UV-vis adsorption band measured for nAg, and it is likely that UV irradiation disturbed electrons at the nAg surface, in turn driving dipole-dipole interactions and the formation of aggregates (Lu et al. 2009; Tang et al. 2002; Li & Lenhart 2012). These same surface energy phenomena also disturb the equilibrium of silver in the oxide layer, leading to enhanced silver dissolution (Li & Lenhart 2012). It is also possible that low levels of reactive oxygen species (ROS) were generated as a result of UV exposure and contributed to surface oxidation. However, production of significant quantities of ROS is unlikely in the absence of an oxidant, such as H_2O_2 or ozone (Garoma and Gurol 2004).

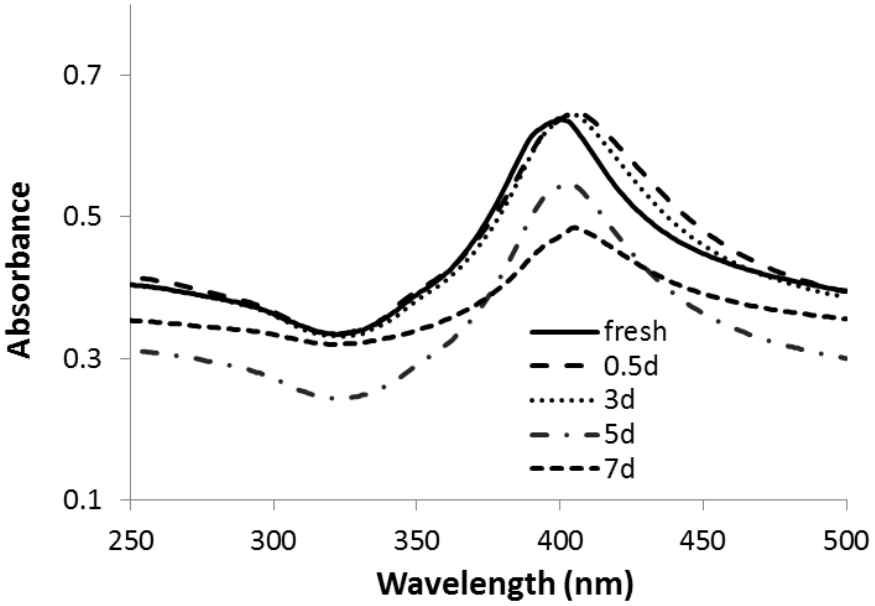

Figure 21. UV-vis spectra of nAg in DI water during exposure to UVA light

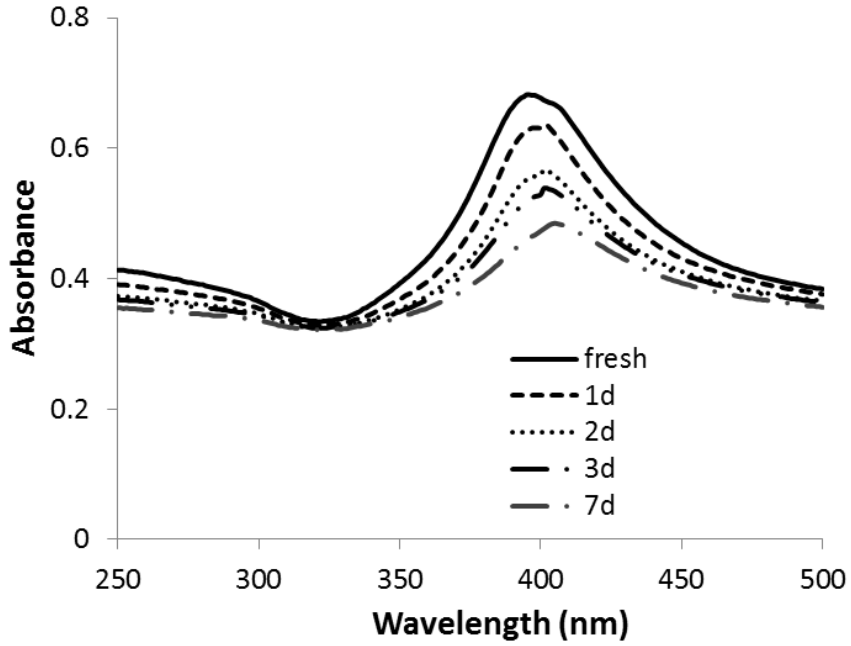

Figure 22. UV-vis spectra of nAg in DI water during exposure to UVB light

The dissolution kinetics of fresh and aged nAg over the 7-day UVA and UVB exposure period are shown in Figure 23. Fresh nAg suspensions exhibited

minimal dissolution, with dissolved silver levels only reaching a maximum value of 0.06 mg/L after 7 days. In comparison, Ag^+ concentrations in UVA-aged suspensions increased to 0.6 mg/L after 7 days, while the concentration of Ag^+ in UVB-exposed nAg suspensions steadily increased to a maximum value of 1.25 mg/L after 7 days. The relative larger rate of nAg dissolution observed for UVB exposure compared to UVA exposure (equivalent intensity of 2.5 mW/cm^2) is consistent with the higher energy of shorter UVB wavelengths.

Silver ion concentrations in UVA-aged nAg suspensions were variable over the first four days of exposure, with cyclical decreases, followed by increases in Ag^+ release. Li and Lenhart (2012) also observed a similar initial decrease in Ag^+ concentrations, which was attributed to re-sorption of released silver onto particle surfaces. Other studies have suggested that an initial decrease in dissolution may be due to sorption of silver ions onto the citrate coating and complexation of Ag^+ in solution by free citrate (Yang et al. 2011; Liu & Hurt 2010). It is also likely that some photoreduction of Ag^+ to Ag (0) occurred in the presence of citrate, a process that has been widely used to synthesize nAg and manipulate the size and shape of prepared particles (Maillard et al. 2003; Ahern & Garrell 1987). These processes may have occurred in UVB-aged suspensions as well, but were likely masked by the much greater rates of dissolution (2-fold higher compared with UVA) during the first few days of aging.

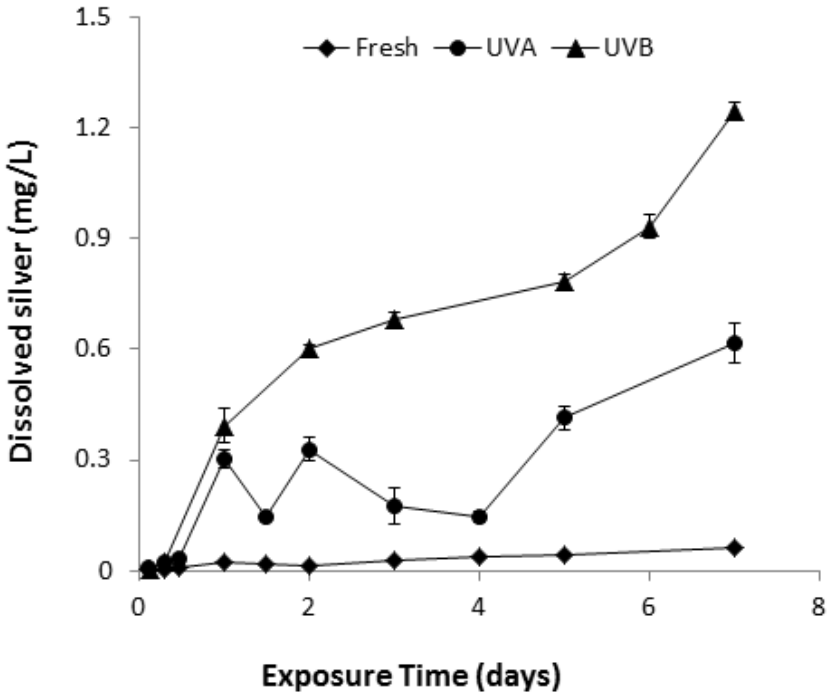

Figure 23. Silver ion release from nAg exposed to UVA or UVB light for 7 days

Complex physical and chemical changes in nAg following UV irradiation are likely the result of a number of processes, including aggregation, dissolution, and secondary precipitation and reduction. Particle dissolution may not go to completion, particularly in solutions that are exposed to UV light or contain multiple electrolyte ions and organic matter, due to aggregation or the reduction of Ag^+ to Ag(0) via light or organic ligands (e.g., citrate) (Li & Lenhart 2012). Gorham (2012) reported that UV-exposed nAg reached equilibrium in cation exchange cells after 70 hr, with approximately 76% of total Ag in the form of Ag^+. The same study also reported a reduction in dissolution when the citrate concentration was increased, presumably due to blocking of oxidation sites and reduction of Ag^+ by citric acid.

Behavior of UV-Aged nAg in Electrolyte Solutions

Prior to transport experiments, changes in size, zeta potential, and dissolution of 3 day-aged nAg were monitored for 180 min in 10 mM and 20 mM $NaNO_3$ solutions. These conditions were representative of the initial conditions and residence time of the nanoparticle suspensions used in sand columns. The size and zeta potential of fresh (un-aged) nAg in 10 mM and 20 mM $NaNO_3$ solutions remained constant at 10.7 ± 0.7 nm and 11.3 ± 1.2 nm and -45.6 ± 0.7 mV and -40.9 ± 0.8 mV, respectively, over the 180 min study (Figure 24 and 25). In contrast, the addition of $NaNO_3$ to aqueous suspensions of 3d-aged nAg resulted in considerable changes to the mean diameter of nAg. UVA-aged nAg aggregated upon addition of 10 mM and 20 mM $NaNO_3$, reaching mean diameters of 86.2 ± 2.1 nm and 298 ± 5 nm respectively, after 180 min. Similarly, the size of UVB-aged nAg increased rapidly, reaching mean diameters of 245 ± 6 nm and 270 ± 6 nm in 10 mM and 20 mM $NaNO_3$ solutions, respectively (Figure 24). The zeta potential of UVA-aged nAg in $NaNO_3$ solutions ranged from ca. -37 to -33 mV, while the zeta potential UVB-aged nAg became slightly less negative after $NaNO_3$ addition, steadily decreasing from an initial value of -31.3 mV to ca. -29 mV and -25 mV at 10 mM and 20 mM, respectively (Figure 25). These batch results are consistent with those of El Badawy et al. (2010) and Li et al. (2010) who reported an increase in aggregation and zeta potential of nAg with increasing $NaNO_3$ concentration.

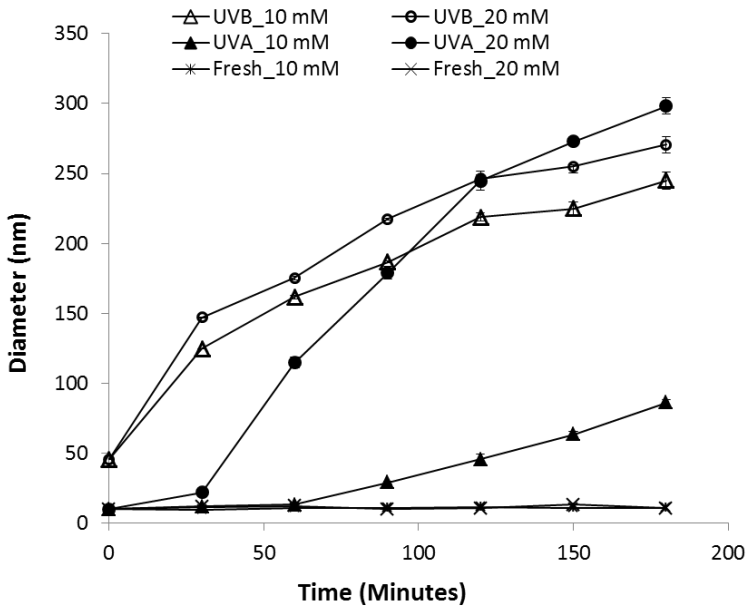

Figure 24. Change in mean diameter of 3 day-UV aged nAg in 10 mM and 20 mM $NaNO_3$ solutions (x-axis represents time after electrolyte addition)

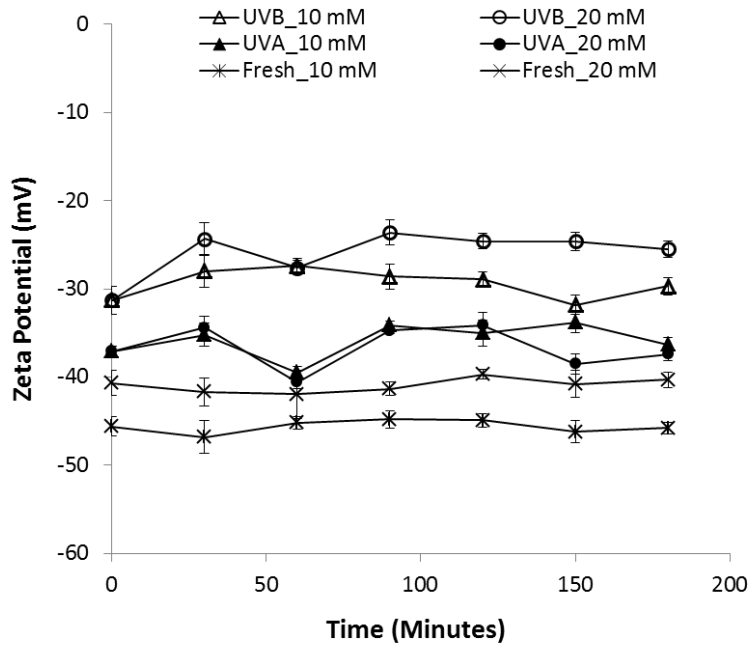

Figure 25. Change in zeta potential of 3 day-UV aged nAg in 10 mM and 20 mM $NaNO_3$ solutions (x-axis represents time after electrolyte addition)

The addition of $NaNO_3$ had a negligible effect on the dissolution of fresh and UVA-aged nAg over 180 min, but accelerated dissolution of UVB-aged nAg (Figure 26). Fresh nAg displayed very minimal dissolution (< 0.04 mg/L) in 10 or 20 mM $NaNO_3$ solutions (pH 7), while Ag^+ concentrations in UVA-aged nAg suspensions remained stable at ca. 0.3 mg/L 180 min after $NaNO_3$ addition. Dissolution in UVB-aged solutions containing 10 mM or 20 mM $NaNO_3$ increased from ca. 0.7 mg/L to 1.1 and 1.4 mg/L, respectively, within 30 min of $NaNO_3$ addition, and then remained constant for the next 150 min. Enhanced dissolution of nAg at higher electrolyte concentrations (i.e., 10 versus 20 mM $NaNO_3$) has been reported previously (X. Li et al. 2010; Huynh & Chen 2011) and can be attributed to destabilization of the electrical double layer surrounding particles and competitive exchange of Ag^+ for Na^+ or other cations in solution (X. Li et al. 2010).

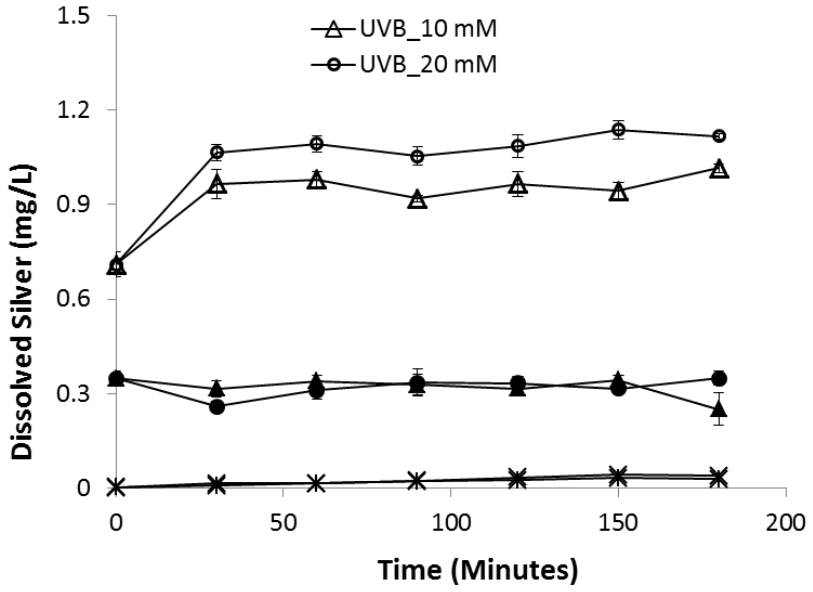

Figure 26. Dissolved silver (Ag^+) release from 3 day-aged silver nanoparticles in $NaNO_3$ solutions (x-axis represents time after electrolyte addition)

Transport and Dissolution of UV-Aged nAg

A series of column experiments was performed to quantify the effects of UV light exposure (3 day) on coupled mobility and dissolution of nAg in water-saturated Ottawa sand. Total and nAg breakthrough curves, expressed as normalized effluent concentration (C/C_0) versus dimensionless pore volumes (PV), obtained from column experiments conducted at 10 mM $NaNO_3$ are shown in Figure 27a. Concentrations of Ag^+ in effluent samples, calculated from the difference between total Ag and nAg, are presented in Figure 27b. Breakthrough of fresh nAg began at ca. 1 PV, gradually climbed to a maximum C/C_0 value of 0.9 and then decreased sharply 1 PV after introduction of nanoparticle-free 10 mM $NaNO_3$ solution (Figure 27a). The shape of the fresh nAg breakthrough curve was asymmetrical, suggesting the existence of a limited retention capacity and consistent with behavior observed in previous nAg transport studies (Liang et al. 2013; Mittelman et al. 2013). The diameter of fresh nAg remained stable at ca. 10 nm in the influent chamber and in effluent samples (Table 3). Minimal dissolution occurred under these experimental conditions (pH 7.0, 10 mM $NaNO_3$), with effluent samples containing less than 0.02 mg/L of Ag^+ (Figure 27b).

UVA- and UVB-aged (3 days) nAg were considerably less mobile compared to fresh nAg, with 45-50% less nAg mass recovered in the column effluent. UVA-aged nAg displayed asymmetrical breakthrough behavior at 10 mM $NaNO_3$, and were strongly retained in the Ottawa sand, reaching a maximum C/C_0 value of only 0.19 (Figure 29a). The observed reduction in mobility is consistent with the less negative zeta potential of UVA-aged nAg (-36.5 mV) compared to fresh nAg

(-45.0 mV). UVB-aged nAg exhibited a downward-sloping effluent concentration plateau, first reaching a maximum relative concentration of 0.29 at 1.5 PV and then gradually declining to 0.05 after ca. 4 PV. This decrease in effluent concentrations may be attributed to physical straining (Bradford et al. 2007) or filter ripening (i.e., preferential attachment of particles or aggregates onto previously deposited particles) (Darby & Lawler 1990). Rapid aggregation of UVB-aged nAg occurred in the influent chamber, with the mean diameter increasing from 96.5 to 214.8 nm over the course of the 75 minute injection period.

Table 3. Column conditions and mass balances for experiments with fresh and UV-aged nAg

Preparation	Flow Rate (mL/min)	Ionic Strength (mM)	% Retained	Mass Balance	Size-start/end (nm)	Zeta Potential (mV)	Ag^+ start/end (mg/L)
Fresh	1.0	10	15.0	97.5	9.21/10.13	-42.7	<D.L./0.002
UVA-aged	0.5	10	80.5	97.2	12.28/199.0	-37.1	0.19/0.42
UVA-aged	1.0	10	67.2	94.6	11.18/170.2	-36.5	0.25/0.33
UVA-aged	1.5	10	39.8	103.0	12.17/130.7	-35.3	0.23/0.38
UVB-aged	1.0	10	58.1	101.5	96.53/214.8	-32.1	0.58/0.93
Fresh	1.0	20	28.6	98.9	10.17/9.98	-39.8	<D.L./0.004
UVA-aged	1.0	20	73.0	93.9	11.01/288.3	-27.8	0.27/0.38
UVB-aged	1.0	20	50.3	98.1	137.5/280.4	-22.4	0.48/1.21

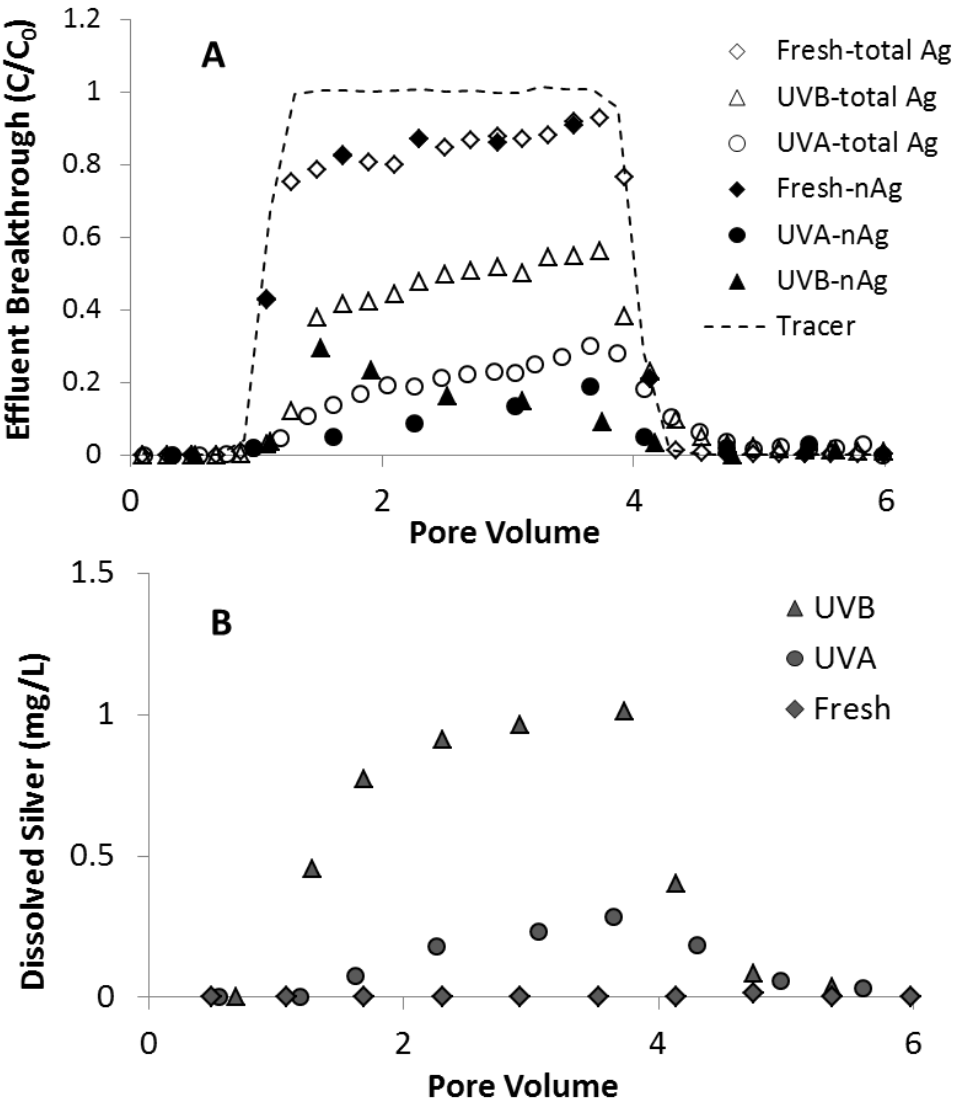

Figure 27. Effluent breakthrough of (A) total silver and nAg and (B) Ag^{+} from column experiments (1.0 mL/min) with fresh and UV-aged nAg in 10 mM $NaNO_3$ solutions.

Experiments conducted by Xu (2006) suggest that straining can be observed at particle diameter to sand grain diameter ratios as low as 8×10^{-3}. The ratio of diameters (215 nm) to 40-50 mesh Ottawa sand (355 μm) is 6.1×10^{-4}, which is more than one order of magnitude smaller than the proposed threshold value for

straining. Therefore, filter ripening is the more likely cause of the down-ward sloping breakthrough curve plateau observed with UVB-aged nAg, and has been previously observed in transport experiments with unstable, aggregating zinc oxide (Jiang et al. 2010) and titanium dioxide (Chen et al. 2012; Godinez et al. 2013) suspensions.

The percentage of injected (or applied) fresh, UVA- and UVB-aged nAg mass that was retained in sand columns at 10 mM $NaNO_3$ was 15.0, 67.2 and 58.1 percent, respectively (Table 3). UVB-aged nAg displayed a less negative zeta potential (-32.1 mV) in 10 mM $NaNO_3$ compared to UVA-aged nAg (-36.5 mV), suggesting that UVB-aged nAg should be more strongly retained on negatively-charge Ottawa sand (Wang et al. 2008). However, a substantial amount of UVB-aged nAg eluted from the column as dissolved ions, with Ag^+ effluent concentrations reaching as high as 0.98 mg/L. Approximately 30% and 65% of effluent silver was in the form of Ag^+ in columns experiments with UVA- and UVB-aged nAg, respectively. These observations are consistent with nAg behavior in electrolyte solutions (Figure 26) in which 3 day UVB-aged nAg dissolved more readily compared to UVA-aged nAg. Although no nanoparticles were detected in effluent samples after ca. 4 PV, tailing was observed in total Ag effluent breakthrough curves for columns with aged nAg, indicating that retained particles were dissolving over time (Figure 27a). A reduction in dissolution of retained particles is likely due to oxidation of the particle surface and the slower dissolution of the Ag_2O layer relative to faster oxidation of the bare Ag core (Li & Lenhart 2012).

The effect of ionic strength on UV-aged nAg transport and dissolution was evaluated by comparing results from column experiments conducted at 10 and 20 mM $NaNO_3$. Effluent breakthrough curves for total Ag and nAg for 20 mM $NaNO_3$ experiments using 3-day aged nAg are shown in Figure 28a, and concentrations of Ag^+ in effluent samples are shown in Figure 28b. Similar to results obtained at 10 mM, the breakthrough curve obtained for fresh nAg at 20 mM $NaNO_3$ was asymmetrical in shape with minimal dissolution (< 0.04 mg/L) (Figure 28a) and no changes in particle diameter in influent or effluent samples were observed. Both UVA- and UVB-aged nAg exhibited a gradual decrease in plateau effluent concentrations at 20 mM $NaNO_3$, consistent with increased aggregation measured in the influent chambers (Figure 24). The size of 3-day UVA- and UVB-aged nAg increased from 11.01 to 288.3 nm and from 137.5 to 280.4 nm, respectively, during the injection period. The amount of nAg in effluent samples at 20 mM $NaNO_3$ was considerably lower compared to 10 mM $NaNO_3$, with breakthrough of UVA- and UVB-aged nAg reaching maximum C/C_0 values of 0.16 and 0.14, respectively. This behavior is consistent with the less negative zeta potential of UVA- (-27.8 mV) and UVB-aged nAg (-22.4 mV) in 20 mM $NaNO_3$ solutions (Table 3). The percentage of applied fresh, UVA- and UVB-aged nAg mass that was retained in sand columns at 20 mM $NaNO_3$ was 28.6, 73.0 and 50.3 percent, respectively.

Effluent silver mass breakthrough at 20 mM $NaNO_3$ was primarily in the form of dissolved ion, with approximately 50% and 80% eluting as Ag^+ in columns with UVA- and UVB-aged nAg, respectively. Maximum Ag^+ concentrations of 0.34

and 1.3 mg/L were measured in effluent samples. These levels are 15-20% higher compared to values obtained from 10 mM $NaNO_3$ columns, which is consistent with increased dissolution of nAg observed in batch experiments at 20 mM compared to 10 mM (Figure 26).

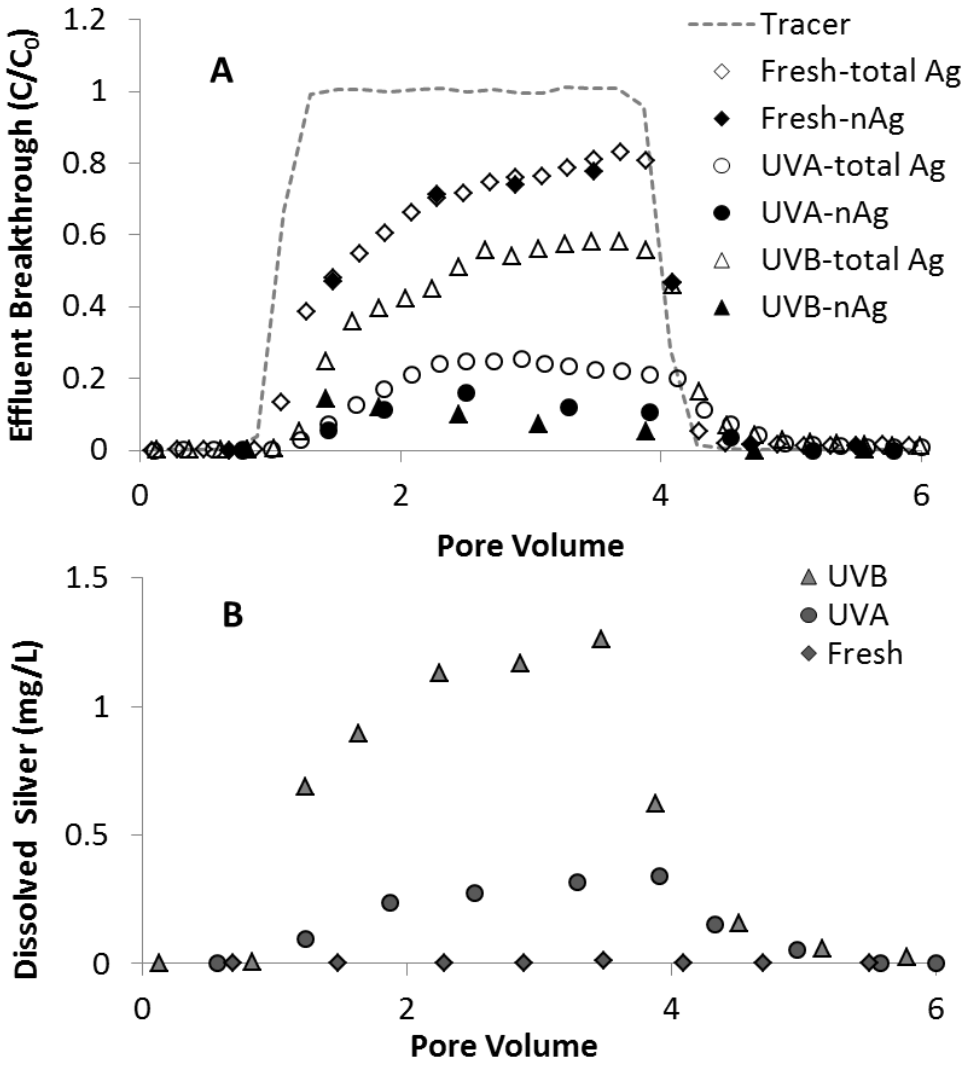

Figure 28. Effluent breakthrough of (A) total silver and nAg and (B) Ag^+ from column experiments (1.0 mL/min) with fresh and UV-aged nAg in 20 mM $NaNO_3$ solutions

The effect of flow rate on the transport and dissolution UVA-aged nAg in sand columns (10 mM $NaNO_3$, pH 7.0) is shown in Figure 29. Results from column studies at three different flow rates show that effluent mass breakthrough of nAg decreased as flow rate was decreased, with maximum C/C_0 values of 0.05, 0.11, and 0.56 measured at flow rates of 0.5, 1.0 and 1.5 mL/min, respectively (Figure 31a). Increasing retention with decreasing flow rate is consistent with findings from prior nanoparticle transport studies and with behavior predicted by filtration theory (Li et al. 2008). Dissolution of nAg in sand columns was strongly dependent upon flow rate, with ca. 75%, 40%, and 20% of silver mass eluting as dissolved ion at flow rates of 0.5, 1.0, and 1.5 mL/min, respectively. Increased Ag^+ release at lower flow rates was attributed to the increased contact time (column residence time) between background flow and attached particles which acts to enhance dissolution reactions. The percentage of input mass retained in the sand with increasing flow rate was 67.2, 80.5, and 39.8%, respectively. Although the lowest nAg breakthrough was observed at 0.5 mL/min, increased dissolution resulted in lower retention compared with the 1.0 mL/min column. Tailing in total Ag and Ag^+ breakthrough curves was observed at all three flow rates tested, and was most pronounced at the lowest flow rate of 0.5 mL/min. After the pulse injection was terminated, Ag^+ continued to elute from the 0.5 mL/min column at relatively high levels, increasing from ca. 0.5 mg/L at 4 PV to 0.7 mg/L at 6 PV (Figure 29b).

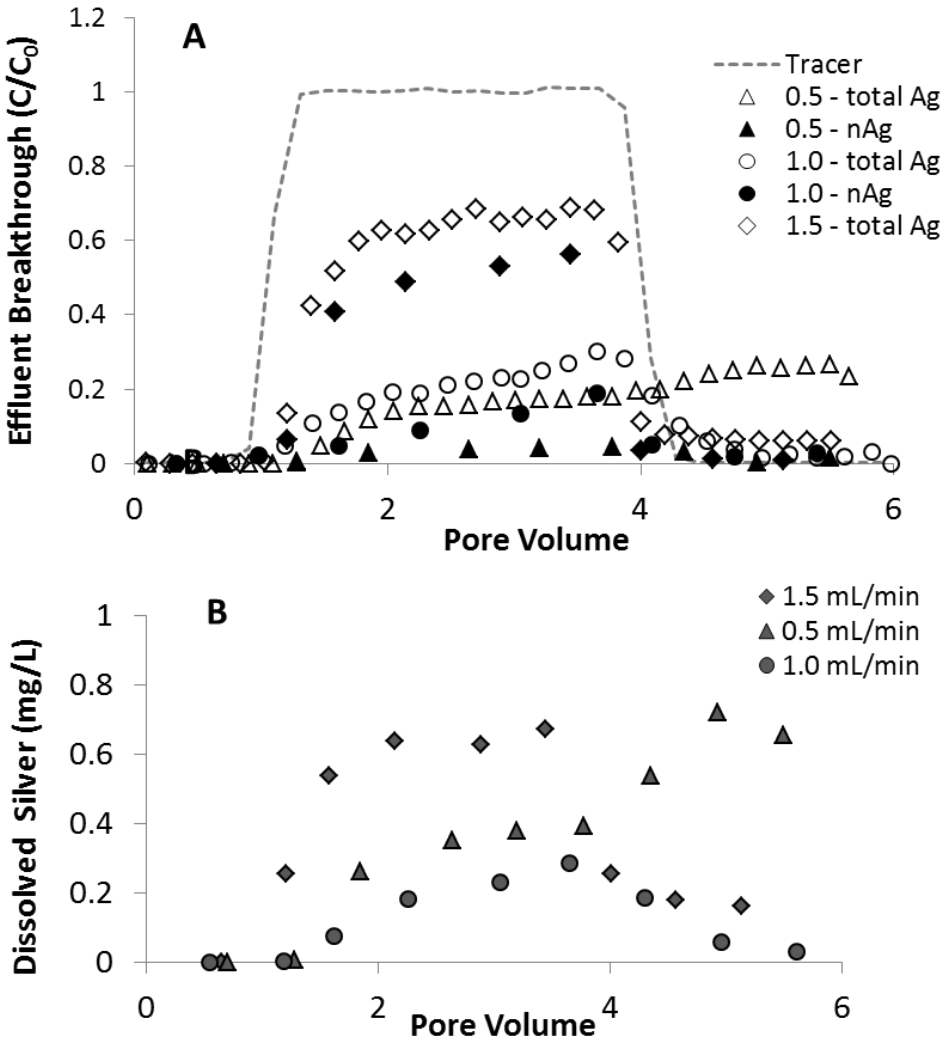

Figure 29. Effect of flow rate on breakthrough of (A) total silver and nAg and (B) Ag^+ in column experiments with UVA-aged nAg in 10 mM $NaNO_3$

Retention profiles obtained at the conclusion of column experiments are shown in Figure 30. The majority of retained mass was in the form of nAg, as the dissolution of retained particles was relatively low (< 0.06 mg/L at 6 PV) at the conclusion of most experiments. Assuming this concentration was also present in the pore water, Ag^+ sorption would account for < 0.2 % of retained mass. In the 0.5 mL/min column, Ag^+ levels were 0.7 mg/L after 6 PV, meaning that up to 2%

of retained mass could exist in the dissolved form. Although UVB-aged nAg were retained more strongly in Ottawa sand compared with UVA-aged nAg at the different ionic strengths tested, they also dissolved more readily resulting in lower overall retention. Retention profiles obtained from all fresh and UV-aged columns were hyper-exponential in shape, with the highest attachment measured near the column inlet. Such retention behavior is consistent with hyper-exponential profiles reported in prior transport studies with nAg(Liang et al. 2013) and other nanoparticle systems (Chowdhury et al. 2011; Jiang et al. 2010; Kasel et al. 2013). High deposition at the inlet has been attributed to filter ripening[40], physical straining (Bradford et al. 2007), sand surface charge or roughness heterogeneity (Li et al. 2006; Song et al. 1994), and particle population heterogeneity (Tong & Johnson 2006) .

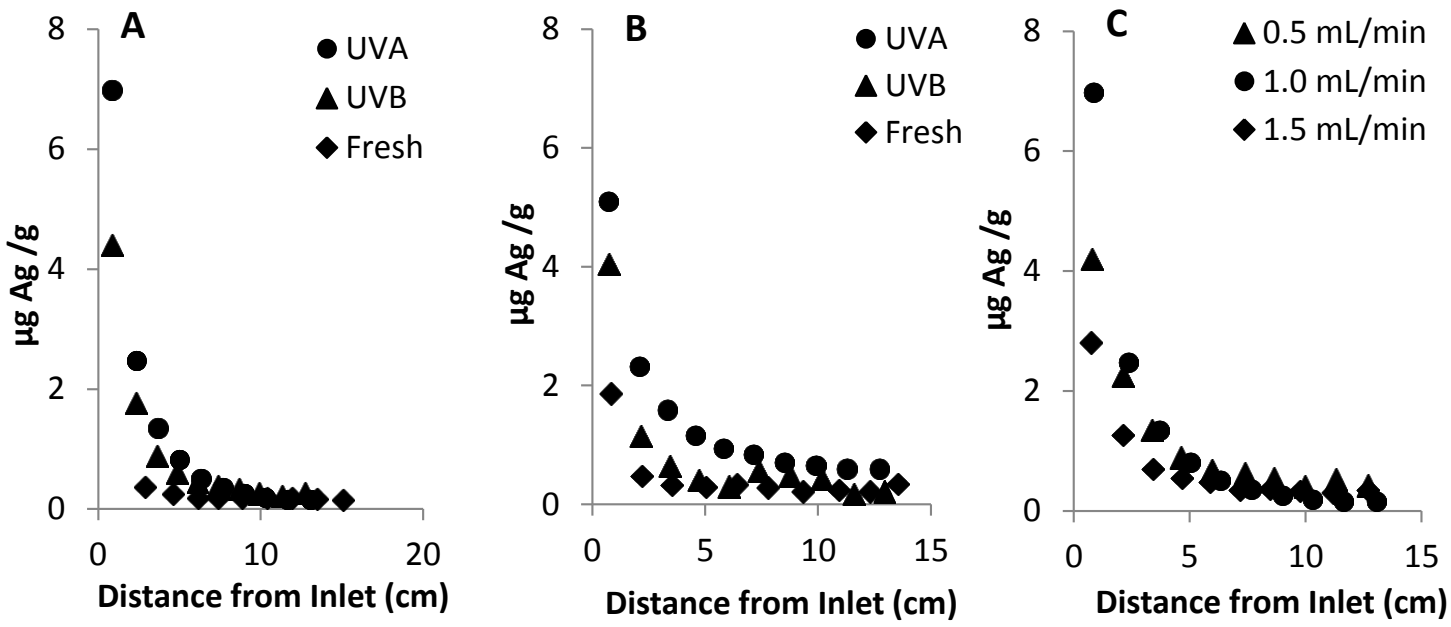

Figure 30. Retention profiles for fresh and UV-aged nAg columns (1.0 mL/min) conditioned with (A) 10 mM $NaNO_3$ and (B) 20 mM $NaNO_3$ and for UVA-aged columns (C) as a function of flow rate in 10 mM $NaNO_3$)

Summary and Conclusions

Nanomaterials are subjected to various physical, chemical and biological transformations in aqueous systems, necessitating a better understanding of "aging" processes on nanoparticle fate and transport in engineered and natural porous media. The objective of this study was to evaluate the mobility and dissolution of citrate-coated silver nanoparticles (nAg) in water-saturated sand following exposure to either ultraviolet (UV)A (320-400 nm) or UVB (280-320 nm) light for up to 7 days. A 3-day exposure resulted in up to a 5-fold increase in nAg mean diameter, a 10-15 mV increase in zeta potential, red-shifts in surface plasmon resonance, and enhanced nAg dissolution, with Ag^+ concentrations increasing from 0.002 mg/L up to 1.2 mg/L. Transport experiments conducted in columns packed with water-saturated 40-50 mesh Ottawa sand revealed that UV-aged nAg were 25-50% more strongly retained compared with fresh nAg. When UV-aged nAg suspensions were introduced to columns, up to 80% of eluted mass was in the form of Ag^+, while less than 1% of mass eluted as Ag^+ in columns with fresh nAg. UVB light exposure resulted in higher amounts of dissolved silver release and greater nAg retention in sand columns compared with UVA exposure, consistent with the less negative zeta potential of UVB-aged nAg (-31 mV) compared to UVA-aged nAg (-37 mV) observed in batch experiments.

This research presented herein provides a comprehensive evaluation of the effects of surface aging on nAg fate and transport in porous media. Batch studies have shown that exposure to UVA and UVB light can significantly alter the size,

surface charge, surface chemistry, and dissolution of nAg. Results from column studies demonstrated that UV-aged nAg may be retained up to 50% more strongly in water-saturated sand compared with freshly prepared suspensions. Although UV-aged nAg were less mobile, column results indicate that aged particles more readily dissolve in porous media, releasing Ag^+ at levels as high as 1.2 mg/L. The oxidation of nAg and subsequent dissolution of the Ag_2O layer to form Ag^+ have been shown to play a key role in observed toxicity to different organisms.(Lok et al. 2006; Gunawan et al. 2009) Both the particulate (nAg) and dissolved ion (Ag^+) forms exhibit antimicrobial effects, with toxicity of nAg attributed to both the pitting action of the small particles on cell membranes(Navarro et al. 2008) and disruption of cellular metabolism by silver ions.(Morones-Ramirez et al. 2013; W.-R. Li et al. 2010) Results presented herein demonstrate that surface aging may alter the toxicity of nAg in natural and engineered porous media, such as membranes and filters.

CHAPTER 5: EFFECT OF UV LIGHT EXPOSURE ON NANO-MAGNETITE TRANSPORT IN WATER-SATURATED POROUS MEDIA

Introduction

Nano-sized iron oxides are one of the most widely produced nanomaterials due to their ubiquitous applications in catalysis, magnetic data storage, biomedical imaging, targeted drug delivery, and medical diagnostics (Lu et al. 2007; Sahoo et al. 2003; Gupta and Gupta 2005). Iron oxide nanoparticles possess unique magnetic properties – for example, magnetite (Fe_3O_4) nanoparticles are super-paramagnetic and have been studied as novel contrast agents for use in magnetic resonance imaging (MRI). Iron oxide nanoparticles have a high sensitivity to oxidation and readily generate ROS in aqueous media, making them ideal candidates for studying the consequences of oxidative aging on fate and transport in the environment.

The objective of this study was to evaluate the impact of UV light exposure on the transport and deposition behavior of oleic-acid coated iron oxide nanoparticles (nMag) in monovalent (NaCl) and divalent ($CaCl_2$) electrolyte solutions in water-saturated porous media. Column experiments were conducted with fresh or 3 day UV-aged nMag in water-saturated 40-50 mesh glass beads conditioned with NaCl (40 and 200 mM) and $CaCl_2$ (2 mM). Columns were destructively sampled at the conclusion of transport experiments in order to quantify the amount of retained mass along the column length. The column influent and effluent were sampled

regularly (1-2 samples/pore volume) and analyzed for mean particle diameter, zeta potential, and iron concentration.

Results and Discussion

A total of ten column experiments were conducted with fresh and aged nMag in 40-50 mesh glass beads (Table 4). nMag suspensions were received from the Fortner group at WUSL and the mean diameter and zeta potential of nMag in DI water were measured by DLS and laser Doppler velocimetry as 18.3 ± 1.8 nm and -48.6 ± 1.4 mV, respectively. These size and zeta potential measurements corroborated with data obtained by the Fortner group prior to shipping fresh and aged nMag, indicating that the samples were not considerably altered during shipping.

At 40 mM NaCl, both fresh and aged nMag suspensions remained stable (< 2 nm increase in size) during the injection time (ca. 75 minutes). The size of particles increased from ca. 44 nm to 49 nm after a 3 day exposure to UV light, while zeta potential became slightly less negative (ca. 1 mV change) following aging. Breakthrough and retention profiles obtained from columns experiments with fresh and aged nMag at 40 mM NaCl were similar in shape and magnitude (Figure 31). Time of breakthrough occurred at 1 pore volume in line with the non-reactive tracer and sharply increased to a C/C_0 value of ca. 0.8 in in experiments with fresh and aged suspensions. The shape of the breakthrough curve was asymmetrical with fresh nMag, while effluent concentrations plateaued and then slightly decreased from 3-4 PV in columns with aged nMag (Figure 31a).

Retention profiles were hyperexponential in shape (Figure 31b), with the highest deposition measured at the inlet (ca. 2-2.5 μg/g). The percentage of mass retained for both fresh and aged nMag suspensions was ca. 15%. Mean diameters of nMag in influent and effluent samples were within ±2 nm, suggesting that aggregation did not occur within the porous media. Minimal changes in nanoparticle size and zeta potential, along with minor differences in the percentage of mass retained between fresh and aged columns, indicate that the aging process did not significantly affect nMag transport behavior at 40 mM NaCl.

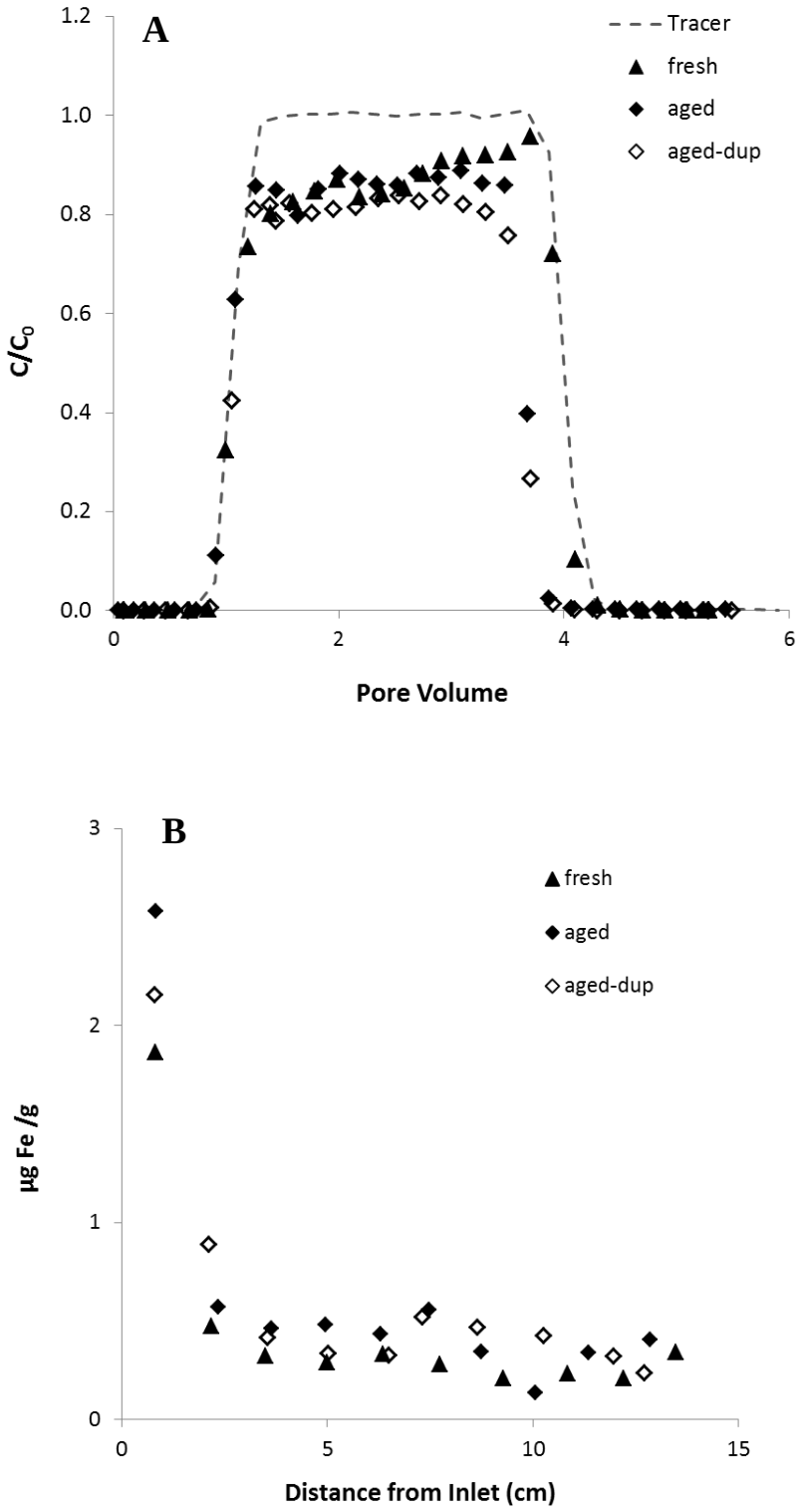

Figure 31. (A) Effluent breakthrough and (B) retention profiles for fresh and aged nMag transport in 40 mM NaCl in 40-50 mesh glass beads

At 200 mM NaCl, the mean diameter of fresh nMag in the influent solution increased from 69.4 to 81.3 nm and from ca. 80.4 to 88.6 for duplicate experiments during the injection period. Zeta potentials for respective duplicate experiments were -29.6 mV and -33.2 mV. In column experiments with fresh nMag at 200 mM NaCl (Figure 32), time of breakthrough was delayed (1.5 PV). Delayed breakthrough has been reported in prior nanoparticles transport studies (e.g., Saleh et al. 2008; Wang et al. 2008), and indicates that retardation processes likely play a role at higher ionic strengths. Breakthrough of fresh nAg was asymmetrical, with effluent concentrations gradually increased to a plateau value of ca. 0.6 and remaining nearly constant without further increase from approximately 3-3.8 PV (Figure 32a). The percentage of breakthrough at 200 mM NaCl was ca. 40%, compared with 85-90% at 40 mM, a trend consistent with less negative zeta potential values at 200 mM (Table 4). Sizes of nMag in effluent samples in the first replicate experiment were 73.5, 76.8 and 74.5 nm at 2 PV, 2.7 PV and 3.5 PV, respectively, indicating aggregation and straining processes were unimportant.

The UV aging process had a marked effect on nMag transport and deposition behavior at the higher ionic strength of 200 mM. The size of nMag in influent suspension during injection period increased from 327.8 to 783.9 nm and 292.1 to 850.7 nm in duplicate experiments. When aged nMag was introduced to a column conditioned with 200 mM NaCl, approximately 30% more mass was retained in glass beads compared with fresh nMag under identical chemical conditions (Figure 32). Breakthrough was slightly delayed (1.5 PV), and effluent nMag

concentrations increased to a peak value of ca. 0.2 after 1.3 PV and then gradually decreased until the pulse eluted from the column. A decreasing breakthrough front has been previously reported in systems with aggregating TiO_2 nanoparticles (Guzman et al. 2006; Chen et al. 2011), and is associated with filter ripening behavior (preferential deposition onto previously deposited particles).

Evidence of straining, which can contribute to a depth-dependent retention capacity, was seen in size measurements of effluent samples. Mean diameters of aged nMag effluent samples collected during the first 200 mM replicate experiment were 409.3, 315.6 and 245.3 nm at 2 PV, 2.7 PV and 3.5 PV, respectively. These measurements suggest that larger particles were strained out as aggregation occurred in the influent solution and as particles aggregated within the porous media. However, the ratio of the largest aggregate diameter (400 nm) to glass bead diameter (365 μm) is ca. 3-7 times smaller than previously reported thresholds ($3\text{-}8 \times 10^{-3}$) for straining in porous media (Xu et al. 2006; Bradford et al. 2007). Physical straining is generally assumed to be a purely physical phenomena controlled solely by system geometry. However, experiments by Bradford et al. (2007) and Torkzaban et al. (2008) suggest that straining can also be strongly associated with solution chemistry. In particular, deep secondary energy minima which develop at high ionic strengths are thought to increase the number of colloids transported to immobile "straining" regions on the solid surface (Torkzaban et al. 2008).

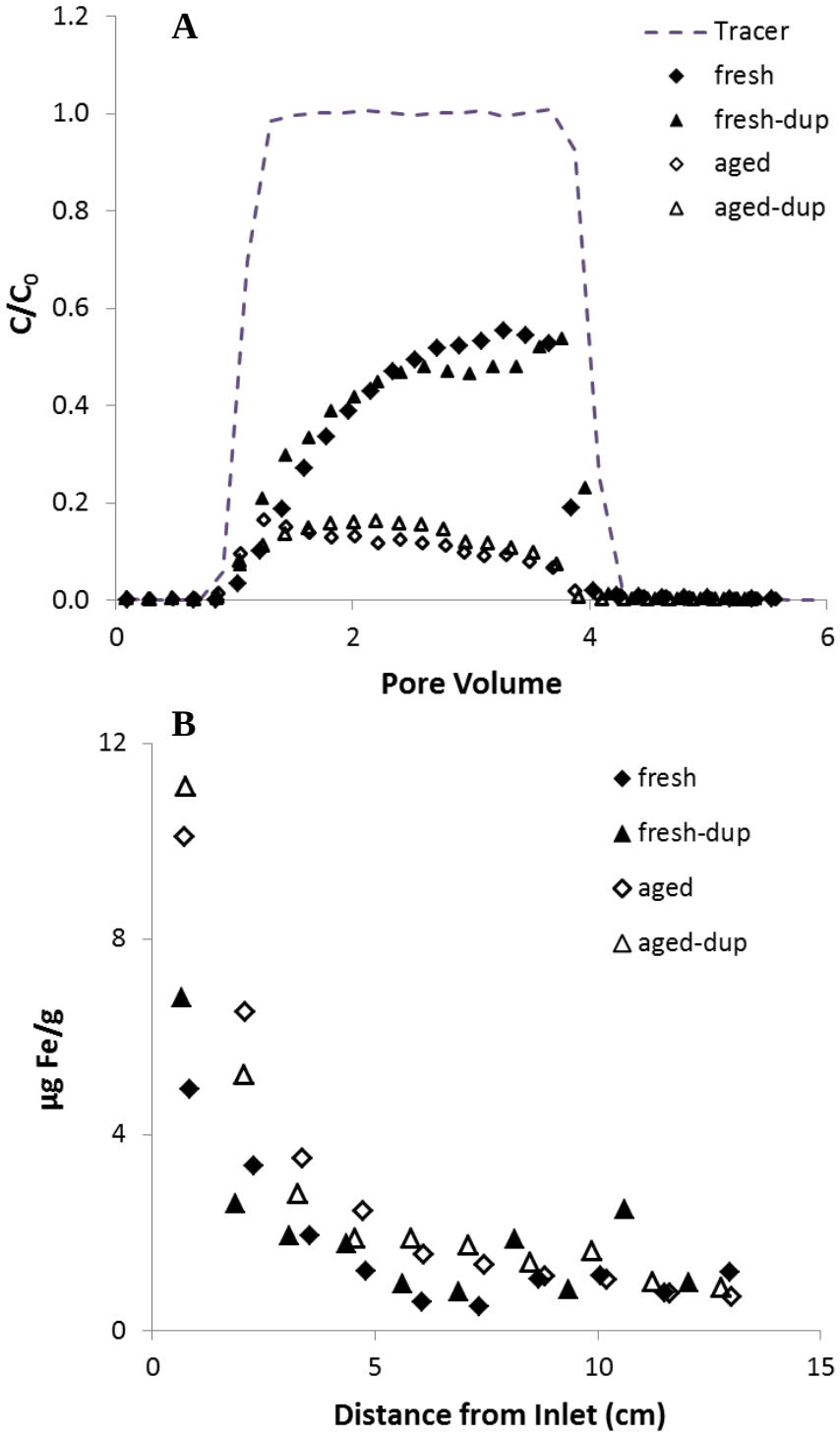

Figure 32. (A) Effluent breakthrough and (B) retention profiles for fresh and aged nMag transport in 200 mM NaCl in 40-50 mesh glass beads

Experiments were also conducted with 2 mM $CaCl_2$ as the background electrolyte to elucidate the effect of a divalent cation on fresh and aged nMag transport behavior (Figure 33). Minimal aggregation occurred in fresh suspensions at 2 mM $CaCl_2$, with mean diameter increasing from 48.3 to 52.9 nm during the 75 minute injection. Aged nMag at 2 mM $CaCl_2$ also readily aggregated, with the mean particle size increasing from 262.5 to 568 nm and from 111.1 and 230.5 nm over the injection in duplicate experiments. Zeta potential was slightly less negative for fresh nMag (-18.4 mV) compared with aged nMag (ca. -22 mV). The lower zeta potential values in divalent salt solutions compared with monovalent solutions is consistent with results from previous studies (e.g., El Badawy et al. 2010), and can be attributed to increased screening of the electric double layer in divalent solutions.

Breakthrough behavior for fresh nMag at 2 mM $CaCl_2$ was similar in shape and magnitude to column experiments at 200 mM NaCl, with effluent concentrations gradually increasing to a nearly constant plateau C/C_0 value of ca. 0.55 (Figure 33a). Aged suspensions at 2 mM $CaCl_2$ were retained more strongly in the glass beads compared with fresh suspensions (ca. 55% and 80-90%, respectively), and displayed filter ripening behavior consistent with aggregation observed in influent solutions. Retention profiles for both aged and fresh suspensions at 200 mM NaCl and 2 mM $CaCl_2$ were hyper-exponential in shape with the highest deposition near the inlet (inlet solid-phase concentrations of ca. 10 µg/g and 5 µg/g for fresh and aged suspensions, respectively)

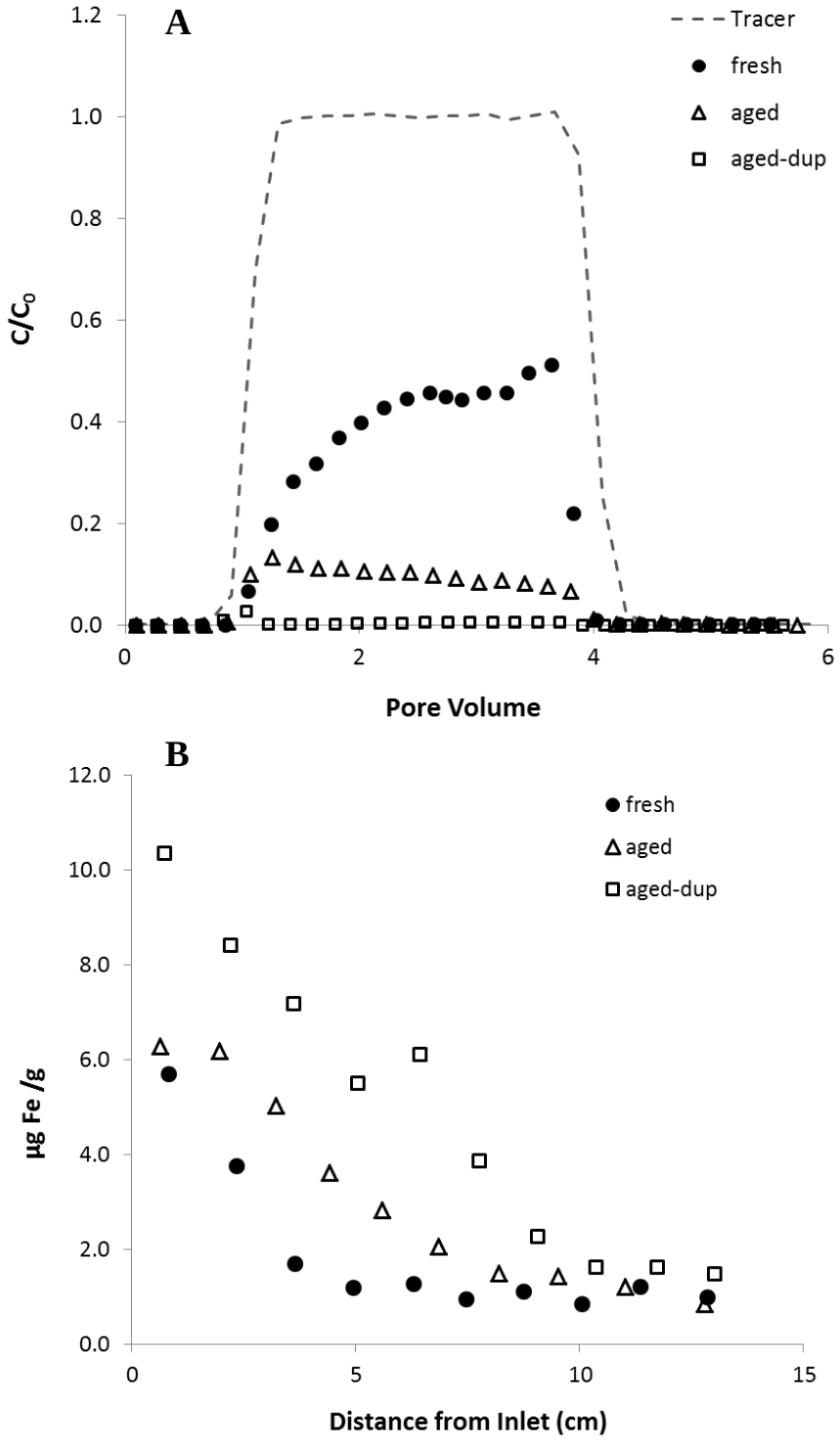

Figure 33. (A) Effluent breakthrough and (B) retention profiles for fresh and aged nMag transport in 2 mM $CaCl_2$ in 40-50 mesh glass beads.

Table 4. Column conditions for fresh and aged nMag transport studies in 40-50 mesh glass beads

Salt	Condition	C_0 (mg/L)	Size-start (nm)	Size-end (nm)	Zeta Potential (mV)	% Retained	Mass Balance
40 mM NaCl	Fresh	5.8	44.2	45.6	-48.7	13.6	104.7
	Aged	6.7	48.9	48.7	-47.9	15.6	103.1
	Aged-dup	6.7	48.9	48.7	-47.9	14.7	96.4
200 mM NaCl	Fresh	4.8	69.4	81.3	-29.6	53.5	94.8
	Fresh-dup	5.1	80.4	88.6	-33.2	55.6	77.8
	Aged	4.9	327.8	783.9	-14.3	82.8	94.4
	Aged-dup	4.7	292.1	850.7	-13.7	83.2	96.2
2 mM CaCl2	Fresh	5.3	48.3	52.9	-18.4	55.7	95.6
	Aged	4.9	262.5	568.2	-23.6	82.4	92.5
	Aged-dup	6.8	111.1	230.5	-22.5	93.1	93.7

Summary and Conclusions

Experimental results from column studies showed that UV-aged magnetite nanoparticles are more strongly retained in water-saturated glass beads compared with un-aged suspensions. At 40 mM NaCl, minimal differences were observed between fresh and aged nMag breakthrough curves and retention profiles. When ionic strength was increased to 200 mM NaCl, aged suspensions were approximately 30% more strongly retained in the glass beads compared with fresh suspensions. Fresh nMag displayed asymmetrical breakthrough, while aged nMag exhibited filter ripening behavior due to aggregation (2-3 times original diameter) in influent solutions. Similar breakthrough and retention behavior was observed at 2 mM $CaCl_2$.

Findings from this study suggest that transformations, such as surface oxidation, are important considerations in environmental fate and transport studies. From a contamination and remediation perspective, stronger retention of nanomaterials in porous media following aging may help to contain contamination and enable easier treatment or removal strategies. It is also possible that surface coatings can be engineered so that nanoparticles are less mobile after aging, preventing uncontrolled migration in the environment. However, less mobile contaminants may also pose a greater ecological risk due to higher localized concentrations and longer time scales required for natural dilution and degradation processes.

CHAPTER 6: SILVER NANOPARTICLE RETENTION AND DISSOLUTION IN CERAMIC WATER FILTERS

Introduction

An estimated 768 million people do not have access to an improved drinking water source, and an additional 1.2 billion are estimated to drink microbiologically contaminated water from improved sources.(WHO & UNICEF 2013) Household water treatment and safe storage (HWTS) options, such as chlorine or filtration methods, can serve as an effective means for providing safe drinking water in areas where water sources are untreated, insufficiently treated, or become contaminated during distribution or storage.(WHO & UNICEF 2013) Ceramic "pot" water filters (CWFs) are one HWTS technology, and consist of an approximately 10-liter capacity ceramic filter that rests on its rim in a lidded receptacle. The receptacle serves as a safe storage container and is fitted with a tap for dispensing filtered water (CMWG 2011).

CWFs are locally produced in >50 countries by firing a mixture of clay, burn-out material, and water to produce a porous ceramic. Silver is added to the filters either after firing or directly into the clay/burn-out material mixture, and has been shown to improve the microbiological efficacy of CWFs (Oyanedel-Craver and Smith 2008; Bielefeldt et al. 2009; Lantagne 2001), inhibit biological growth within filters and plastic receptacles (Bloem et al. 2009; Oyanedel-Craver and Smith 2008), potentially reducing filter clogging. Casein-coated silver nanoparticles (nAg) are the most commonly used silver formulation for CWFs,

while some factories use silver nitrate ($AgNO_3$) due to lower cost and/or local availability (Rayner et al. 2013).

Water treatment in CWFs is thus achieved through three mechanisms: physical straining of larger particles, such as protozoa, due to pore size exclusion; physical-chemical attachment of particles (some bacteria and viruses) to the ceramic surface; and the antimicrobial action of silver. While silver released into the treated water may prevent re-contamination during water storage, silver release over time may also decrease the effective lifespan of the filter and result in increased silver exposure. The World Health Organization and Environmental Protection Agency have established a secondary standard of 0.1 mg/L for silver in drinking water (WHO 2011; US EPA 2014). Thus, there are competing requirements of applying sufficient silver to ensure disinfection during treatment and storage over time while not exceeding drinking water standards.

Prior research has shown that after painting, dipping, or firing-in nAg or $AgNO_3$, silver concentrations in effluent water fall below 0.1 mg/L after 8-24 hr of filter throughput (Bielefeldt et al. 2009; van Halem et al. 2009; Oyandel-Craver and Smith 2008; Rayner et al. 2013; Ren and Smith 2013). A limited number of studies have examined the impact of different water chemistries on silver fate in CWFs, and shown that pH, ionic strength, dissolved organic matter, and chlorine content can influence silver retention (Rayner et al. 2013; Ren and Smith 2013; Bielefeldt et al. 2013). We identified no studies to date that examined the impact of transient water chemistry on silver retention, the mechanism of silver transport and release (e.g., nanoparticle detachment, dissolution, or cation exchange) under

different influent chemistries, or consistently distinguished between Ag^+ and nAg particles in effluent samples. The form of silver released from filters could have implications related to user safety and disinfection performance, as the biological activity of nAg results primarily from release of silver ions, with the degree of nAg dissolution correlated with antimicrobial activity (Tolaymat et al. 2010; Choi et al. 2008; Dasari & Hwang 2010).

Based on observations from prior nAg transport studies conducted in water-saturated sands (Mittelman et al. 2013), we hypothesized that nAg would be strongly retained within the ceramic filter matrix, and would slowly dissolve, releasing Ag^+ into effluent water over time. The objective of this study was to evaluate the fate and transport of nAg and Ag^+ in ceramic filter disks painted with 0.03 mg/g of nAg or $AgNO_3$ and exposed to influent waters of variable pH (5, 7, 9), ionic strength (1, 10, 50mM), and cation species (Na^+, Ca^{2+}, Mg^{2+}). Cation exchange experiments (batch and in situ) were conducted in order to determine the importance of ion exchange in silver release. In addition, a set of experiments utilized filters that were painted on only the top surface, rather than both the top and bottom, to determine the relative amounts of silver released from each painted surface. Experimental data were translated into recommendations for filter manufacturers and distributors regarding the longevity of the silver coating.

Summary of Methods

Prior to silver application, the ceramic material was characterized through pore size distribution analysis, non-reactive tracer tests, and cation exchange capacity

(CEC) experiments. Derjaguin Landau,Verwey, Overbeek (DLVO) theory calculations were performed to qualitatively predict how changes in solution chemistry may influence attachment and detachment behavior in the nAg-ceramic system. After silver application, silver release was quantified in 10 separate disks treated with different application methods and exposed to variable influent water chemistries (Table 5). These data were analyzed to predict the duration of silver retention under different source water compositions.

Table 5. Experimental parameters for ceramic filter experiments

Coating	Application	Variable of Interest	Sequence
$AgNO_3$	Both sides	Base case	10 mM $NaNO_3$ (pH 7)
nAg	Both sides	Base case	10 mM $NaNO_3$ (pH 7)
$AgNO_3$	Both sides	Ionic strength	10 mM → 1 mM → 10 mM $NaNO_3$ (pH 7)
nAg	Both sides	Ionic strength	10 mM → 1 mM → 10 mM $NaNO_3$ (pH 7)
nAg	Both sides	Ionic strength	10 mM → 1 mM → 10 mM → 50 mM → 10 mM $NaNO_3$ (pH 7)
$AgNO_3$	Both sides	pH	pH 7 → pH 5 → pH 7 → pH 9 → pH 7 (10 mM $NaNO_3$)
nAg	Both sides	pH	pH 7 → pH 5 → pH 7 → pH 9 → pH 7 (10 mM $NaNO_3$)
nAg	Both sides	Cation species	Na^+ → Mg^{2+} → Na^+ → Ca2+ → Na^+ (10 mM, pH 7)
nAg	One side	Base case	10 mM $NaNO_3$ (pH 7)
$AgNO_3$	One side	Base case	10 mM $NaNO_3$ (pH 7)

Results and Discussion

Pore Size Distribution

Mercury intrusion porosimetry measurements performed on fragments collected from two disks yielded an average porosity value of 0.42 (41.9 ± 0.8%), which corresponded to a total disk pore volume of 11.8 ± 0.7 mL. At the applied flow rate of 0.6 mL/min, this pore volume corresponds to a fluid residence time of approximately 20 minutes. The porosimetry data also indicated that the disk manufacturing and firing process creates a highly heterogeneous pore structure; approximately 35% of pore diameters were less than 20 nm, 45% ranged from 1 nm to 30 μm, and 10% were larger than 30 μm (Figure 34). Due to the wide distribution of pore sizes, non-reactive tracer tests were conducted to further characterize the pore structure and hydrodynamic properties of the intact ceramic disks.

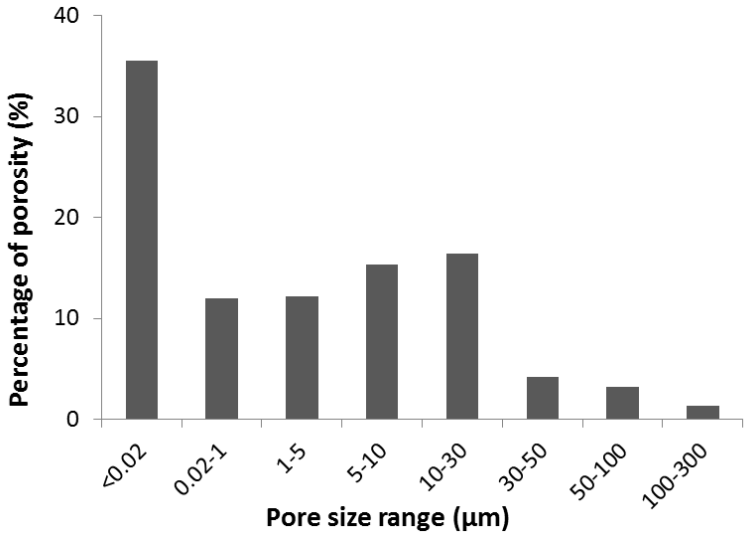

Figure 34. Pore size distribution in ceramic filter disks as determined by high intrusion mercury porosimetry

Tracer Tests and Modeling

A series of non-reactive tracer studies was undertaken to confirm the total pore volume and to investigate differences in water flow among ceramic disks from the same batch. In the first tracer experiment, a small pulse (0.09 pore volumes, ca. 1 mL) of 10 mM NaBr solution was introduced into a water-saturated ceramic disk. The resulting effluent BTC reached a maximum relative concentration (C/C_0) of approximately 0.11, and exhibited tailing in the distal portion (late time) of the BTC (Figure 35). The observed asymmetrical shape of the effluent BTC was consistent with non-reactive tracer data reported by Oyanedel-Craver and Smith (2008) and Kallman et al. (2011), who evaluated *E. coli* transport in ceramic filter disks. To further evaluate the flow conditions of the filter disks, the pulse width was increased to approximately 3.7 pore volumes, which resulted in maximum

relative effluent concentrations (C/C_0) ranging from 0.9 to 1.0 (Figure 36). Representative non-reactive tracer BTCs obtained for three separate disks (Figure 55) exhibited early breakthrough of bromide tracer, indicating that that solute did not interrogate the pore volume. In addition, all of the BTCs exhibited tailing, which was particularly pronounced for disks 10 and 12. Mass recovery ranged from 98 to 100% in these experiments, indicating that exchange of non-reactive solute between regions of mobile-immobile water was reversible even in the disks that exhibited prolonged tailing.

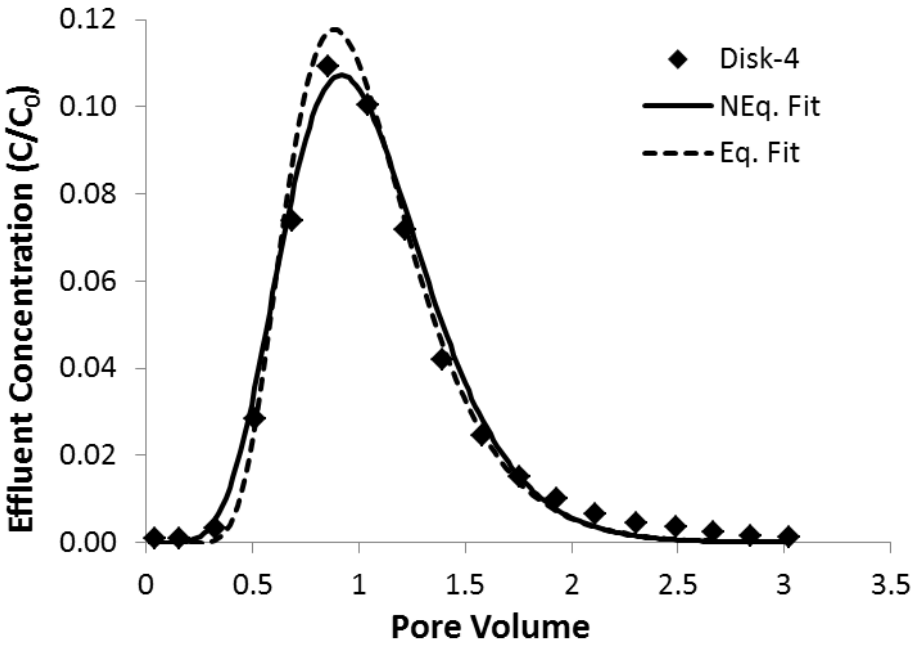

Figure 35. Effluent breakthrough of bromide following a small pulse injection (0.09 PV, ca. 1 mL) of 10 mM NaBr solution to a water-saturated ceramic disk. Equilibrium and non-equilibrium solute transport model fits to the data are shown.

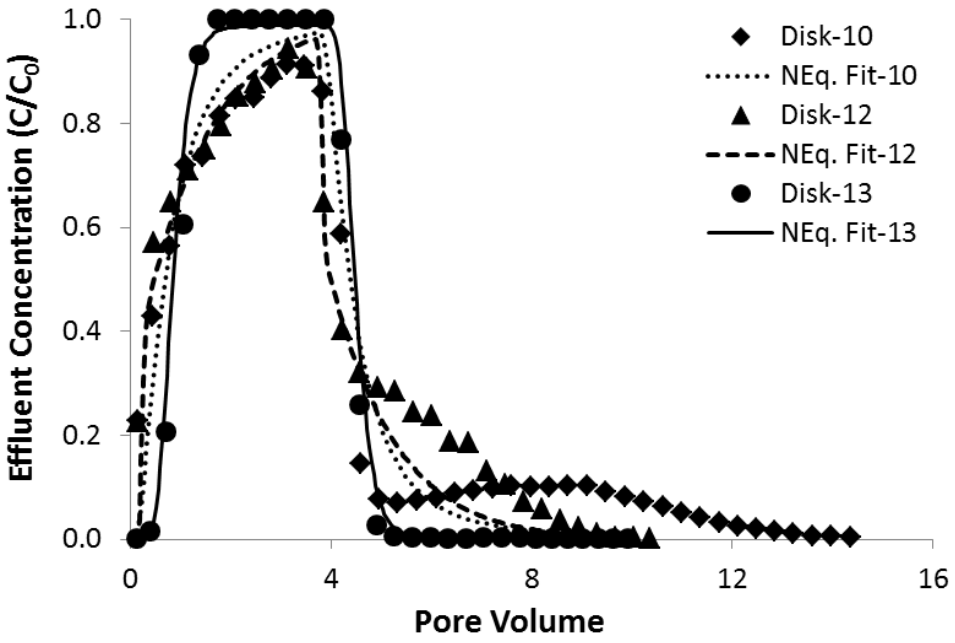

Figure 36. Non-reactive tracer breakthrough curves for three separate disks (10, 12 and 13) following a ca. 3.7 pore volume pulse injection of 10 mM NaBr solution. Equilibrium and non-equilibrium solute transport model fits to the data are shown.

Effluent breakthrough data from non-reactive tracer experiments were initially fit to the dimensionless form of the advective-dispersive transport (ADR) equation, which can be expressed as:

$$R_F \frac{\partial C^*}{\partial PV} = \frac{1}{Pe}\frac{\partial^2 C^*}{\partial X^2} - \frac{\partial C^*}{\partial X} \qquad (27)$$

$$R_F = 1 + \frac{K_D \rho_b}{\theta_w};\ C^* = \frac{C}{C_0};\ PV = \frac{v_p t}{L};\ Pe = \frac{v_p L}{D_H};\ X^* = \frac{x}{L} \qquad (28)$$

where R_F is the solute retardation factor, which is fixed at 1.0 for a non-reactive tracer (i.e., $K_D = 0$), ρ_b is the bulk density of the matrix, C is the aqueous concentration, C_0 is the influent or applied aqueous concentration, PV is the dimensionless pore volume, v_p is the pore-water velocity, t is time, L is the length of the domain in the direction of flow (i.e., filter disk thickness), Pe is the Peclet number, D_H is the hydrodynamic dispersion coefficient, X^* is dimensionless distance, and x is the distance parallel to flow. The CXTFIT program (ver. 2.0; Toride et al., 1999), which employs a least squares fitting routine, was used to simulate the effluent BTC data shown in Figure 35. Results of this simulation, which assumed local equilibrium conditions and no solute sorption, yielded a Peclet number of 15.5, which corresponds to a hydrodynamic dispersion coefficient of 0.42 cm^2/hr (Figure 1, Eq. fit).

To account for non-equilibrium mass transfer processes, a "two-region" solute transport model was fit to the data (Gamerdinger et al., 1990; van Genuchten and Wagenet, 1989), which accounted for physical mass transfer limitations (e.g., solute diffusion between regions of mobile and immobile water). Fitting this model to the measured bromide BTC for the 0.1 PV pulse (Figure35, NEq. fit) resulted in a β value of 0.22, indicating that only 22% of the pore volume contained mobile water. Thus, the volumetric content of mobile water ($\theta_{w,m}$) was only considered to be 0.09 cm^3/cm^3, while the total volumetric water content (θ_w) was 0.42 cm^3/cm^3. The fitted value for ω was 29.7, which corresponds to a mass transfer rate (α_1) of 36.0 1/hr, while the fitted Peclet number was 21.9, which corresponds to a hydrodynamic dispersion coefficient of 1.32 cm^2/hr. The

difference between the dispersion coefficients obtained using the "two-region" and the "equilibrium" model despite the similarity in fitted Peclet numbers (21.9 versus 15.5), results from the higher pore-water velocity due to the small value of $\theta_{w,m}$. The two-region model was able to capture the effluent BTC for disk 13 (Figure 36), which yielded a β value of 0.89 (i.e., 11% of the pore water consisted of immobile water), an ω value of 0.015 (α_1 = 0.015 1/hr), and a Peclet number of 18.7 (D_H = 0.36 cm^2/hr).

Non-reactive tracer data and the pore size analysis together indicate that the ceramic disks contain variable pore structures with regions of immobile water. The variability among tracer BTCs in disks produced from the same batch suggests that heterogeneity produced during the manufacturing process may strongly influence solute transport.

Cation Exchange

The CEC of the crushed ceramic filter material was determined to be 5.2 ± 0.4 meq/100g based on the $CaCl_2/Mg(NO_3)_2$ batch exchange method. This value is consistent with CEC data reported for reference clay minerals and natural soils. For example, the CEC of representative kaolinites, determined using similar methods, are reported to range from 2.4 to 4.2 meq/100g respectively (Pennell et al. 1991), while the CEC of natural soils typically ranges from 2.0 to 50 meq/100g, and is strongly dependent upon the soil organic carbon and clay contents (Taylor, 1985). The batch-determined CEC of the crushed ceramic material was expected to be larger than that of the intact filter disk due to the

greater exposed surface area available for exchange. The CEC of an intact ceramic disk determined via displacement of bound Ca^{2+} with Mg^{2+} (Figure 37) was 4.2 meq/100g, which was ca. 20% less than the batch measured value as anticipated. The similarity of the values indicates that Ca^{2+} saturation and Mg^{2+} exchange occurred relatively quickly, with Mg^{2+} reaching the steady-state input concentration (0.5 M) within 5 hours.

Ag-Mg exchange also occurred rapidly (Figure 38), with displaced Ag concentrations decreasing to zero within 4 hr. The CEC of filter disks for Ag^{+} was found to be 11 meq/100g, higher than the CEC values measured above through Mg-Ca exchange, but still within the same order of magnitude. The Ag^{+} exchange corresponds to an absorbed mass of ca.1200 µg/g, indicating that the recommended silver application of 30 µg/g falls well below the adsorption capacity of the ceramic material. CEC values obtained by different methods produce similar values (4 – 11 meq/100 g) and together indicate that the ceramic has a relatively high cation adsorption and exchange capacity.

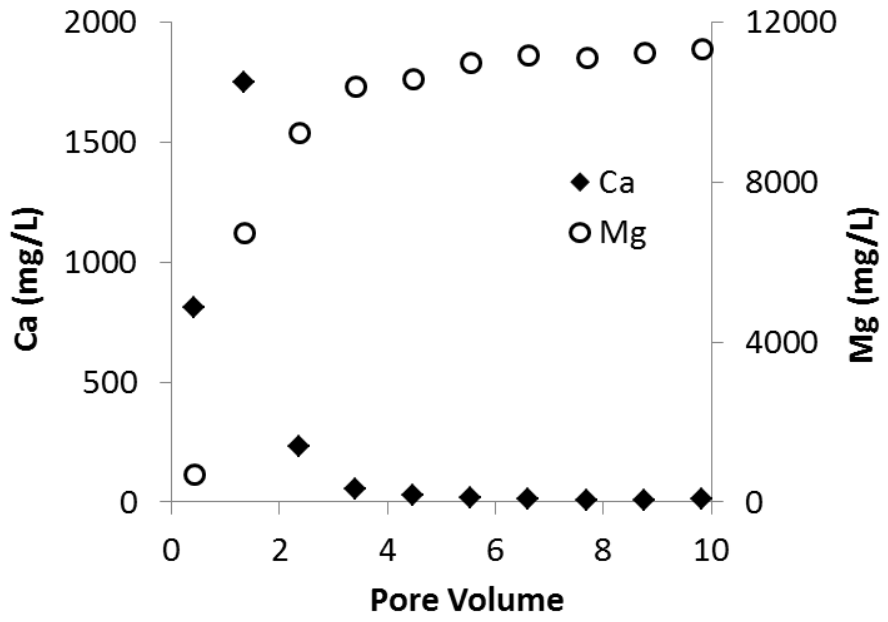

Figure 37. Exchange of Mg for Ca over time in a Ca-saturated filter disk.

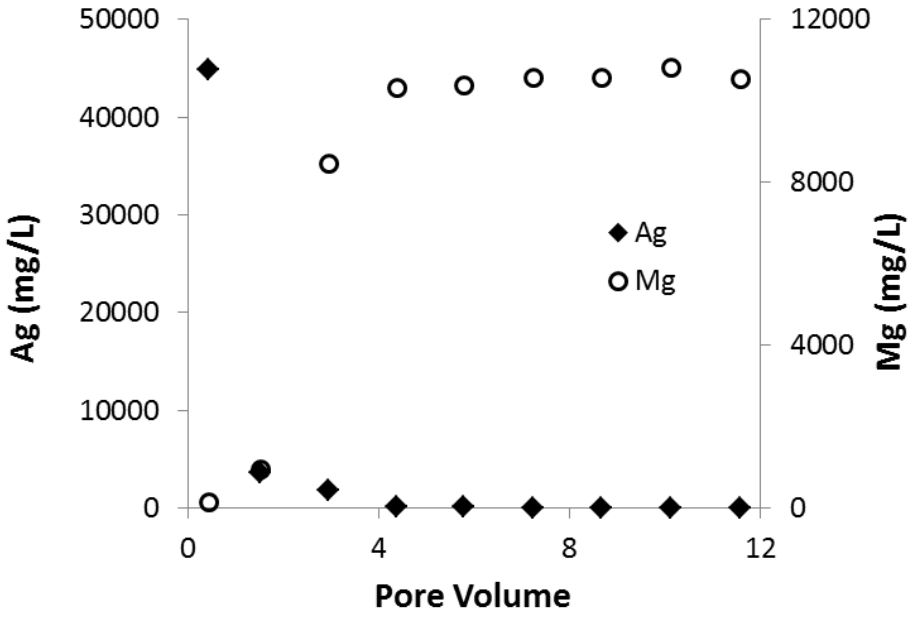

Figure 38. Exchange of Ag for Ca over time in an Ag-saturated filter disk.

DLVO Calculations

The mean diameter of nAg and the zeta potential of nAg and the ceramic surface were measured at various ionic strengths and pH (Table 6). A Hamaker constant of 1.23×10^{-20} J was calculated for the nAg-water-ceramic system (Bergström 1997; Hiemenz and Rajagopalan 1997). Interaction energy profiles for the system at different ionic strength indicate the presence of a sizable primary energy barrier (repulsive conditions) at 1 mM and purely attractive conditions at 50 mM (Figure 39). Similarly, DLVO theory predicts a large energy barrier to deposition at pH 9, and purely attractive conditions (negative interaction energy) at pH 5 (Figure 40). Nanoparticle detachment is often associated with "unfavorable" deposition in secondary energy minima, and small secondary energy interactions were predicted at 1 mM and pH 9. A summary of the magnitude of the primary energy barrier and the secondary energy minimum as a function of pH and ionic strength are provided in Table 7.

Table 6. Mean diameter of nAg and zeta potential of nAg and crushed ceramic disk material at different ionic strengths and pH values

pH	Ionic strength	Mean Diameter (nm)	Zeta Potential (mV)	
			nAg	Ceramic
7	1	50.9	-38.5	-31.6
7	10	73.3	-30.1	-27.6
7	50	575	-15.2	-18.4
5	10	79.2	-23.8	-21.8
9	10	73.5	-39.1	-35.2

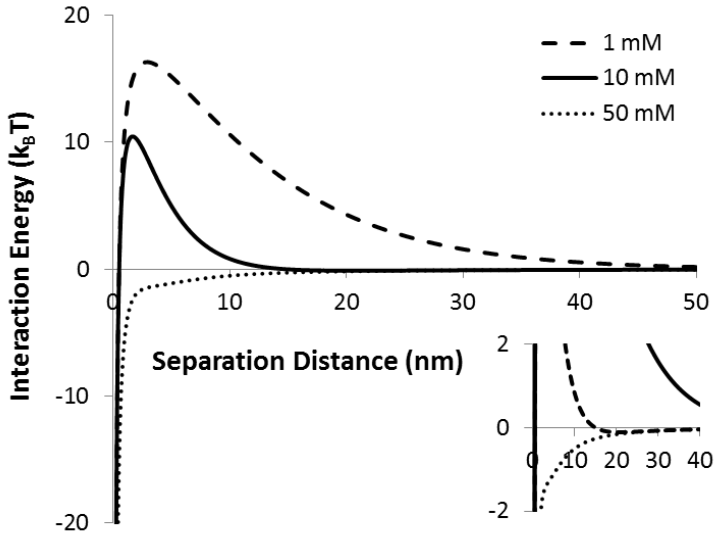

Figure 39. DLVO interaction energy profiles between nAg and the ceramic collector surface at three different ionic strengths. Inset shows a small secondary minimum at 10 mM.

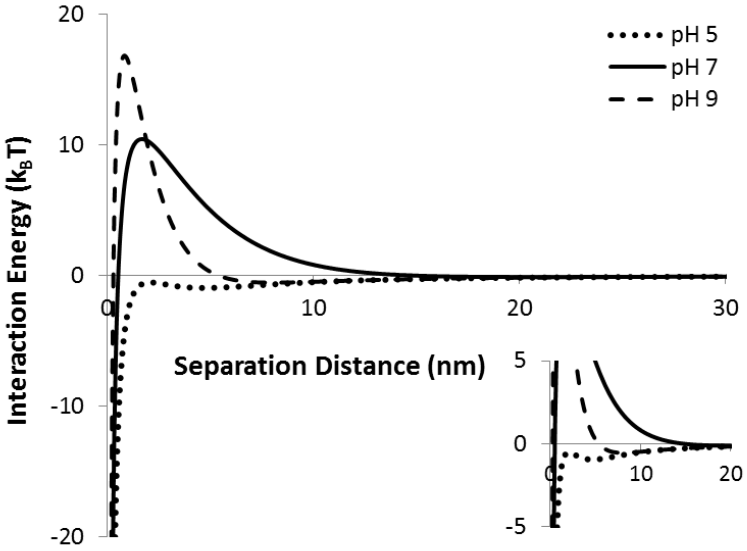

Figure 40. DLVO interaction energy profiles between nAg and the ceramic collector surface at different pH values. Inset shows a small secondary energy minimum at pH 9.

Table 7. Maximum interaction energy and depth of secondary energy minima for nAg-ceramic interactions at different ionic strength and pH values.

pH	Ionic strength	Φ_{max} (k_BT)	$\Phi_{2\text{-}min}$ (k_BT)
7	1	16.3	-0.00720
7	10	10.5	-0.114
7	50	N/A	N/A
5	10	N/A	N/A
9	10	16.8	-0.539

Baseline Silver Release

In $AgNO_3$- and nAg-painted disks, effluent Ag^+ concentrations reached maximum levels of ~1 mg/L and 0.3-0.5 mg/L, respectively, within the first 3 hr (5 PV) of flushing with pH 7 10mM $NaNO_3$ (Figure 41). Effluent silver levels fell below the drinking water standard (0.1 mg/L) after 10-15 hr (30-45 PV) and 3-4 hr (18-24 PV) in $AgNO_3$- and nAg-painted disks, respectively. Silver release from disks painted with $AgNO_3$ was higher than nAg, in general agreement with the findings of Rayner (2013) who reported 20% greater release of Ag^+ from nAg-painted disks during the first 24 hr (72 PV) of throughput with a phosphate buffer solution (pH 7.4, 16.3mM).

In these experiments, the observed differences between total and dissolved silver release were minimal (< 0.05 mg/L), indicating that the majority of silver eluted from the disks existed in dissolved form, rather than as nanoparticles (nAg). The greatest amount of nAg release, based on the difference between total and ionic silver, occurred within the first 15 pore volumes (5 hr) of flushing, and represented less than 1% of total silver mass released.

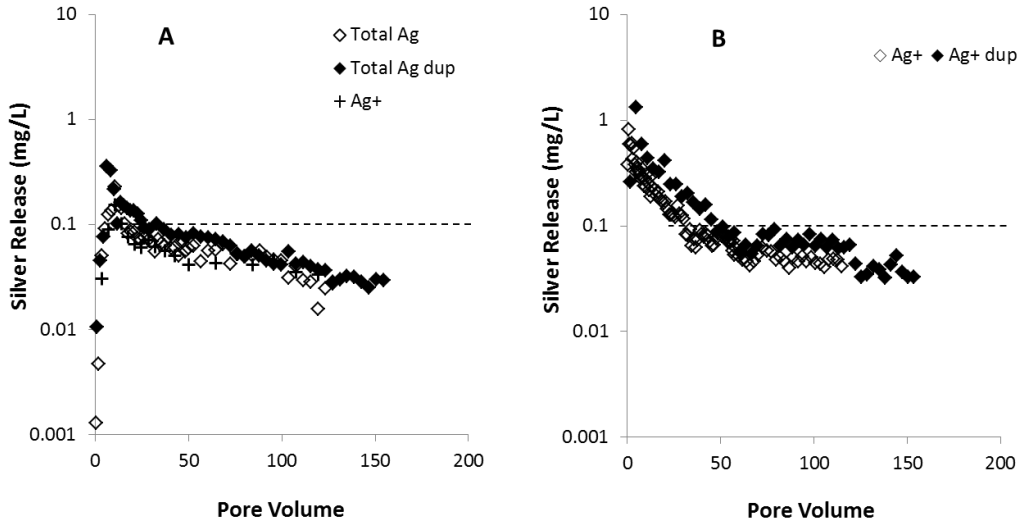

Figure 41. Silver release from duplicate ceramic filter disks painted with either (a) $AgNO_3$ or (b) nAg after introduction of an aqueous solution of 10 mM $NaNO_3$ (pH 7). To improve clarity, Ag^+ data are only shown for one of the nAg-painted disks (open diamonds) in (b).

Effect of ionic strength, cation species, and pH

Silver elution from disks painted with either $AgNO_3$ or nAg was sensitive to changes in IS. When influent solution IS was reduced from 10mM to 1mM $NaNO_3$ for 4.5 hr (14 PV), a nearly 10-fold decrease in effluent silver concentrations was observed (Figure 42). When IS was increased back to 10mM $NaNO_3$, silver concentrations in effluent samples quickly rebounded to previous levels. Small amounts of nAg release were observed in the nAg-painted disk when IS was decreased to 1mM, consistent with interaction energy predictions. This observed nanoparticle detachment is consistent with prior transport studies (Wang et al. 2008; Phenrat 2009b; Bradford et al. 2007) which reported detachment of negatively-charged colloids and nanoparticles from silica surfaces

upon a decrease in IS. At lower IS, screening of the electrical double layer of nAg is minimized, resulting in weaker particle-surface interactions (Hiemenz & Rajagopalan 1997).

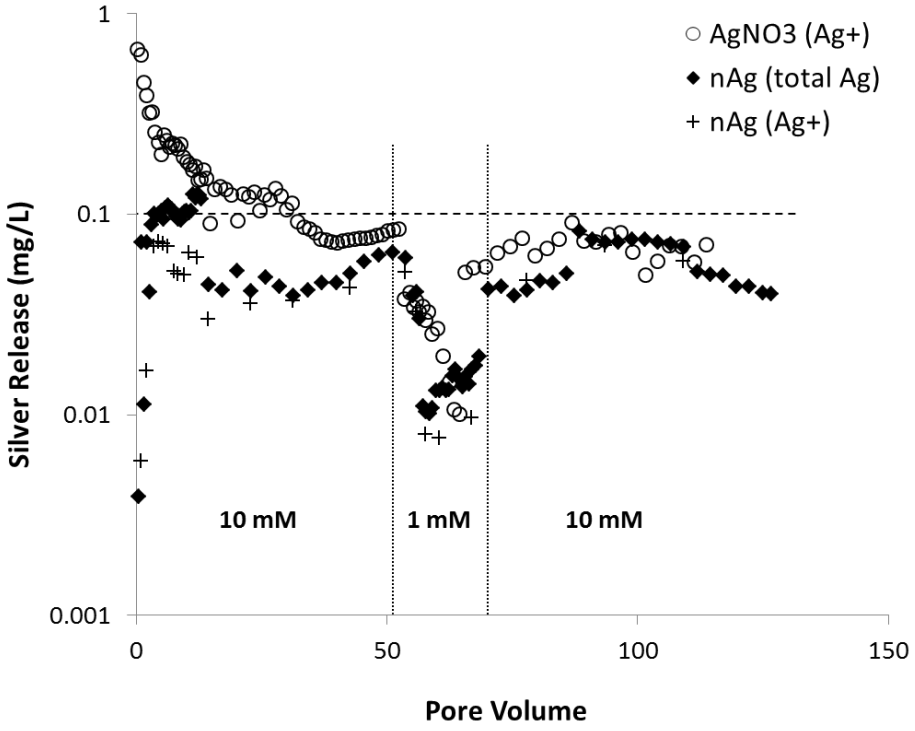

Figure 42. Effect of an ionic strength reduction (10 to 1 mM $NaNO_3$, pH 7) on silver release from filter disks painted with $AgNO_3$ or casein-nAg. Both total and dissolved silver data are shown for the filter disk painted with nAg.

Similar results were observed in an nAg disk exposed to sequential changes in IS (10mM to 1mM to 10mM to 50mM to 10mM $NaNO_3$ (Figure 43). Effluent silver concentrations decreased by approximately a factor of 10 upon the IS reduction to 1mM and were accompanied by the release of nAg. When IS was increased from 10 to 50mM $NaNO_3$ for 4 hr (12 PV), effluent silver concentrations reached levels as high as 0.8 mg/L. In a separate nAg-painted disk, when influent solution cation

species was changed from monovalent ($NaNO_3$) to divalent ($Ca(NO_3)_2$ or $Mg(NO_3)_2$) at a constant IS (10mM, pH 7), effluent Ag^+ concentrations increased 2-4-fold (Figure 44). Peak effluent silver concentrations were 0.20 and 0.17 mg/L upon introduction of 10mM $Ca(NO_3)_2$ or $Mg(NO_3)_2$ solutions, respectively.

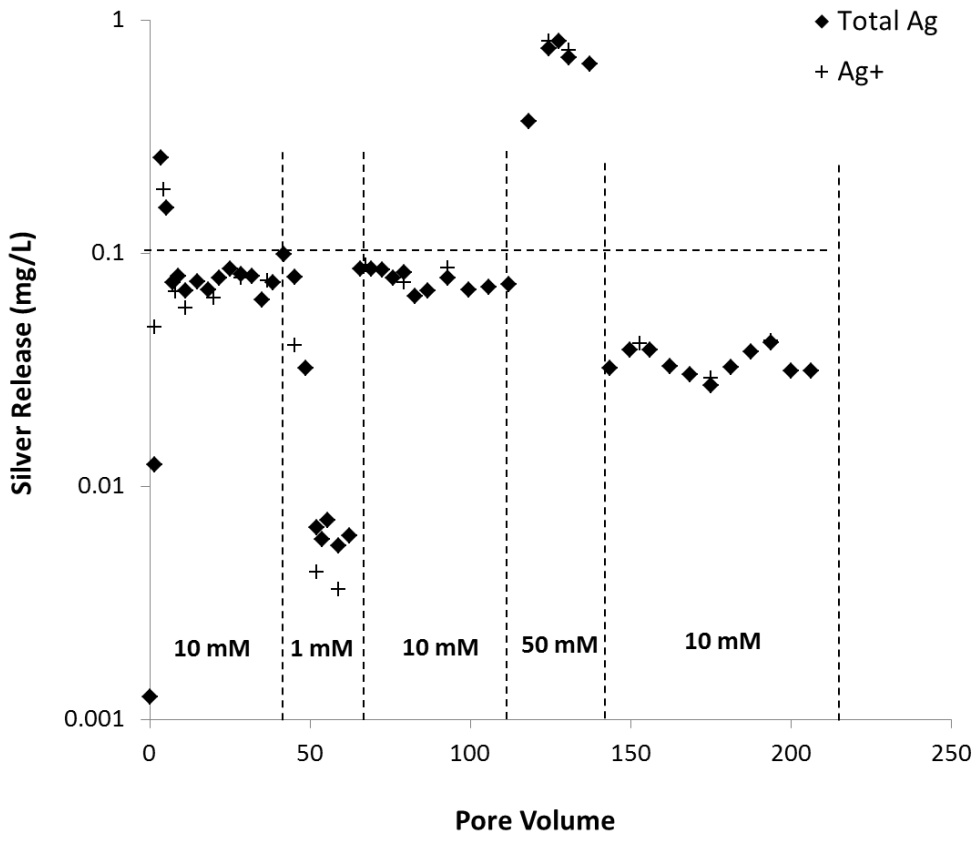

Figure 43. Effects of sequential changes in IS (10 mM, 1 mM, 10 mM, 50 mM, 10 mM $NaNO_3$) on total Ag and Ag^+ release from a filter disk painted with casein-nAg. Both total and dissolved silver data are shown.

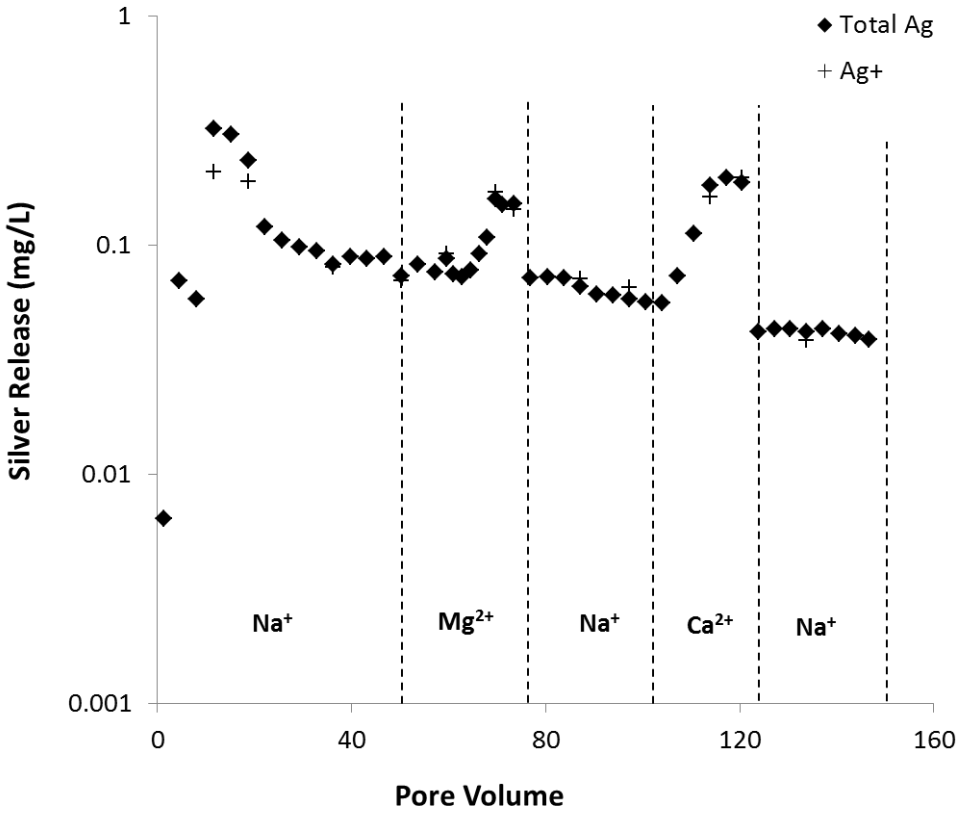

Figure 44. Impact of cation species (constant ionic strength of 10 mM) on total and dissolved silver release from filter disks painted with casein-nAg

Sequential changes in pH in an $AgNO_3$-painted disk resulted in a ~3-fold increase in effluent silver concentrations (maximum=0.3 mg/L) when the pH was decreased from 7 to 5 and a 9-fold reduction in effluent silver when the pH was increased from 7 to 9 (minimum=0.006 mg/L) (Figure 45). Results were similar in a disk painted with nAg, with a 5-fold increase in effluent silver after pH reduction (maximum=0.4 mg/L), and a 6-8-fold decrease following a pH increase (minimum=0.008 mg/L). At all pH values tested, silver in the effluent samples was primarily in the dissolved form, with only minimal nanoparticle (nAg) release

(<0.02 mg/L) observed in the first hours of throughput at pH 7 and following the increase in pH, consistent with DLVO theory predictions.

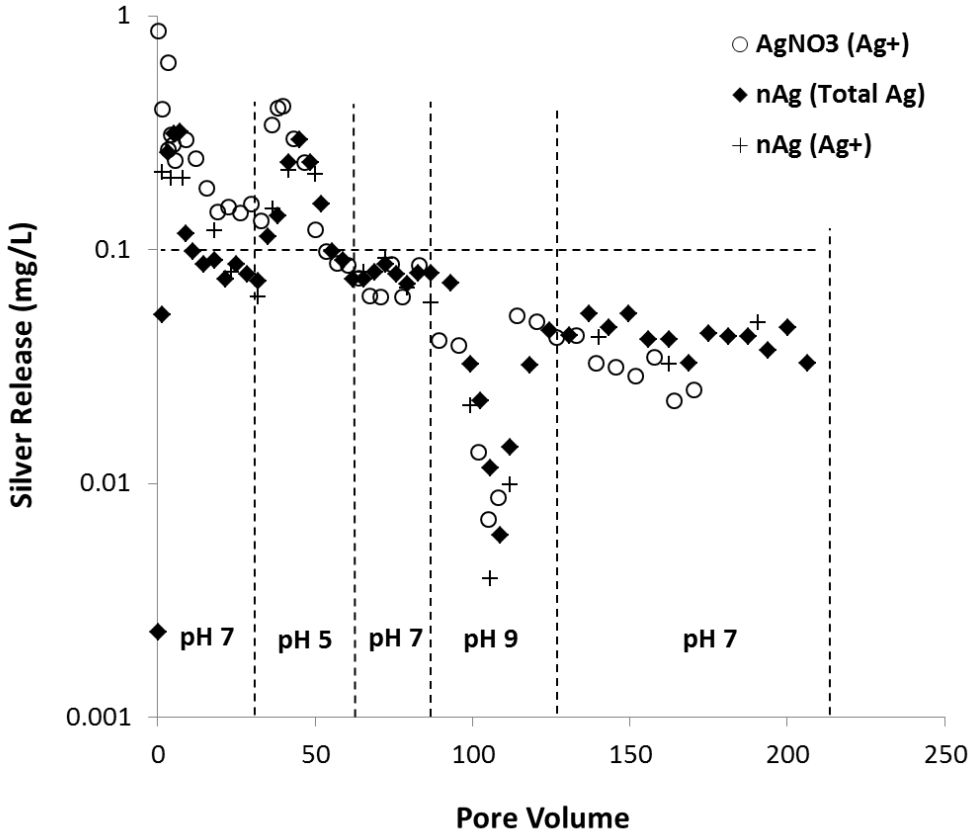

Figure 45. Impact of variable influent pH (7, 5, 7, 9, 7; 10 mM $NaNO_3$) on silver release from filter disks painted with $AgNO_3$ and casein-nAg. Both total and dissolved silver data are shown for the n-Ag painted disk.

Although some nAg release (<0.05 mg/L) was observed at pH 9 and 1mM, Ag^+ was the dominant silver form in effluent samples across all influent water conditions evaluated, leading to the conclusion that nanoparticle detachment is not the predominant mechanism of silver release in CWFs. Silver release in nAg-painted disks can also occur through dissolution of retained nAg (Ag^0 to Ag^+ or

Ag_2O to Ag^+) (Taghavy et al. 2013) and cation exchange (substitution of Ag^+ for Na^+, H^+, or other cations). The similarity between silver elution profiles from $AgNO_3$- and nAg-painted disks indicates that release is controlled by dissolution and exchange processes involving Ag^+, rather than by DLVO-mediated particle-surface interactions and particle detachment.

Silver release from filter disks was highly sensitive to changes in IS, cation valence, and pH of the influent water. Data from all silver release experiments demonstrated that disks responded rapidly (within 1 PV) to changes in influent solution chemistry, consistent with results from cation exchange experiments. When influent water returned to background conditions (pH 7, 10mM $NaNO_3$), silver effluent levels returned to baseline concentrations, indicating that silver adsorption was reversible. Decreasing pH from 7 to 5, increasing IS from 10mM to 50mM $NaNO_3$, and changing from a monovalent to divalent cation resulted in rapid Ag^+ exchange, with release rates governed by competitive exchange of Ag^+ for Na^+, Ca^{2+}, and Mg^{2+}, and H^+. Similarly, when there are fewer positively charged ions in solution, or ions of lower valence, Ag^+ was better retained on the ceramic surface.

Effect of Application Method on Silver Release

In a disk painted on only the top surface with $AgNO_3$, no silver was detected in effluent samples after 20 hr (60 PV) of flushing with 10mM $NaNO_3$ at pH 7 (Figure 46a). However, when IS was increased to 50mM for 18 PV, effluent silver concentrations increased to a maximum of 0.03 mg/L. In an nAg-painted disk

painted on only the top surface, effluent silver concentrations reached a maximum of 0.04 mg/L after 3 hr (10 PV), compared with peak concentrations of 0.2-0.4 mg/L when disks were painted on both the top and bottom surfaces (Figure 46b). Silver release rapidly decreased to parts-per-billion levels after 15-20 hr (45-60 PV) of flushing with 10mM $NaNO_3$. In disks painted on only the top surface with either silver formulation, effluent silver levels were consistently lower than international standards, indicating the lower surface contributes the majority of silver release.

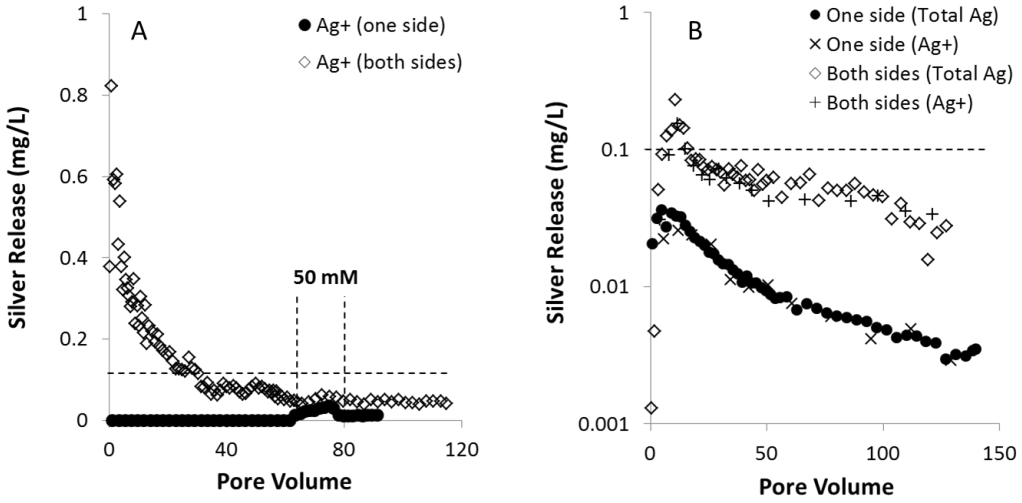

Figure 46. Silver release from disks painted with either (a) $AgNO_3$ or (b) casein-nAg on one side or both sides (equivalent mass loading of 30 µg Ag/g) after introducing an aqueous solution containing 10 mM $NaNO_3$ at pH 7. Both total and dissolved silver data are shown for the nAg painted disk.

Longevity Calculations

The estimated duration of silver retention in filters was highly dependent on influent water chemistry (Figure 47 and 48). In a best-case influent water

chemistry scenario (pH=9, IS=10 mM), silver would remain in the filter element for 7.5 and 5.7 years for nAg and $AgNO_3$, respectively. Using "normal" water conditions (pH=7), silver would remain in the ceramic filter for 1.1 and 0.6 years (IS=10mM) and 3.4 and 3.5 years (IS=1mM) for nAg and $AgNO_3$ application, respectively. The highest levels of silver release occurred with pH=5 and IS=50mM; under these conditions, silver would remain in the filter element for 0.12 and 0.05 years for nAg and $AgNO_3$, respectively. These results show that the use of poor quality source water, particularly with high salinity or low pH , can decrease silver retention in filters 10-30-fold compared with normal conditions (pH=7, IS=1-10mM).

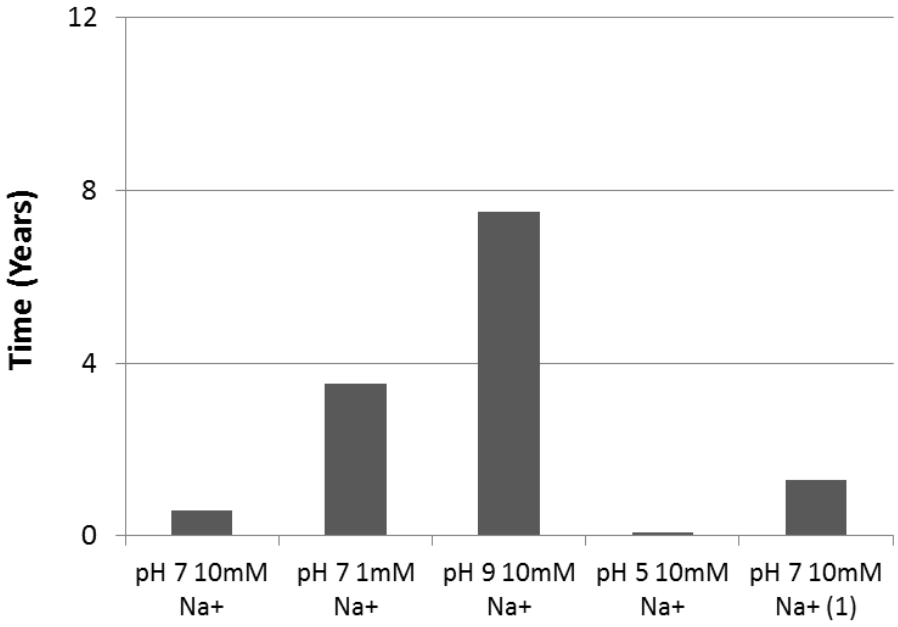

Figure 47. Estimated longevity of $AgNO_3$ coating in years under different water chemistries. "(1)" denotes one-sided application

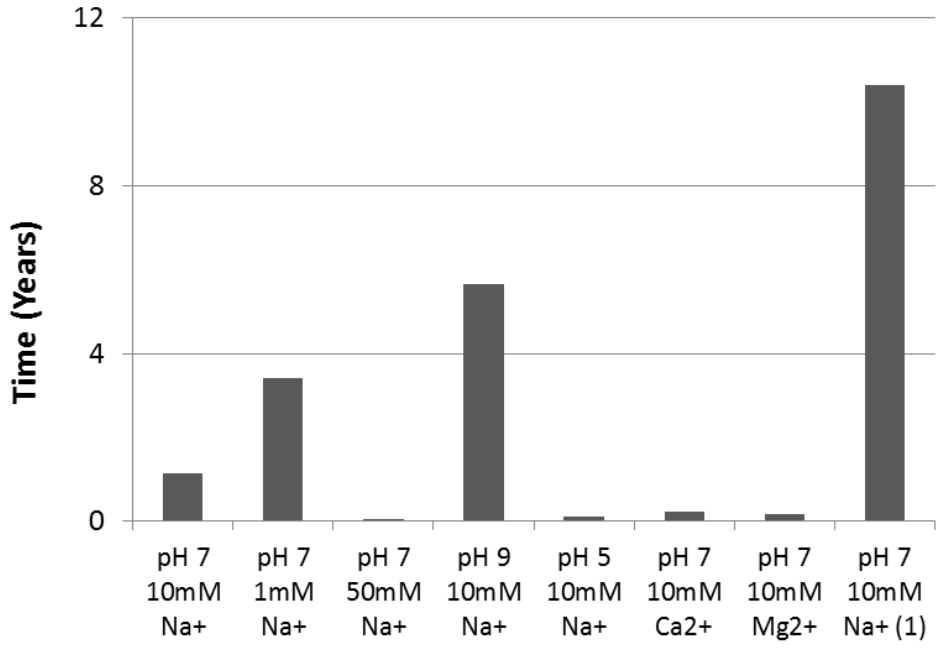

Figure 48. Estimated longevity of silver nanoparticle (nAg) coating in years under different water chemistries. "(1)" denotes one-sided application.

Recommendations and Limitations

These experimental results are, to our knowledge, the first data that highlight the importance of dissolution and cation exchange in silver release across a range of influent water chemistry conditions. Releases of 5-10 times international guidelines for silver in drinking water were observed in disks exposed to increased IS (10 to 50mM), divalent cations (Ca^{2+} and Mg^{2+}), and reduced pH (pH 7 to 5). Conversely, decreases in silver release were measured in disks exposed to decreased IS (10 to 1mM) and increased pH (pH 7 to 9). These results can be translated into recommendations for filter manufacturers and distributors. The target population for ceramic filters tends to use poor-quality (chemically and microbiologically), untreated water sources. Although it may be difficult for

filters users in developing regions to obtain a consistent supply of high quality source water, these findings support the recommendations that households should avoid using acidic, saline, and "hard" (high concentration of divalent cations) water to preserve the integrity of the silver coating and avoid exposure to unnecessarily high concentrations of silver. It is important to note that while Ag^{+} concentrations exceeded international standards, nanoparticle (nAg) exposure is expected to be minimal with CWF use. Additionally, these findings suggest that the use of alkaline water (pH≥9) will reduce silver release, and may consequently reduce the bactericidal action of silver in filters and storage containers.

The data presented herein also inform an ongoing discussion on recommended filter lifespan and manufacturing quality control. Some manufacturing facilities recommend filter element replacement regularly, while others recommend an indefinite lifespan of 'until it breaks.'(CMWG 2011). Our data support a regular filter replacement schedule (or reapplication of silver schedule) to ensure ongoing efficacy. However, further research is required to evaluate the effectiveness of silver reapplication, as previous research by Bielefeldt (2009) observed decreased retention following reapplication. These data also support recommended testing of filters for microbiological removal performance prior to silver application (CMWG 2011), so that silver is not relied on as the primary treatment mechanism. Filters can achieve recommended bacterial log reduction values of ≥2 (*E. coli*) without silver application (Kallman et al. 2010; Oyanedel-Craver & Smith 2008; Rayner et al. 2013). Therefore, well-manufactured filters should remain effective beyond the lifespan of the silver coating. Although a top surface

application minimized user exposure and increased silver retention, an inside-only application in full-sized filters may not be a feasible manufacturing change. Lantagne (2001) reported that silver applied to the outside surface was critical in maintaining disinfection properties.

Limitations of this data include the use of one application strength of silver and one filter recipe. It is possible that results might vary with different clays, burnout material characteristics, variations in firing temperature, or amount of silver applied. Although we do not anticipate that our general conclusions would significantly change, further research is recommended to compare silver elution across additional filter recipes. Additionally, the influence of changes in other common water constituents on silver release – such as chlorine and dissolved organic matter – should also be explored further. The experimental set-up may also introduce some uncertainty, as the water pressure through the filter disks is likely greater than the hydraulic head that full-sized filters are subjected to under normal gravity-flow conditions.

Summary and Conclusions

The addition of silver nanoparticles (nAg) or silver nitrate ($AgNO_3$) improves the microbiological efficacy of ceramic water filters used for household water treatment. Silver release, however, can lead to undesirable health effects and a reduction in filter effectiveness. We evaluated the contribution of nanoparticle detachment, dissolution, and cation exchange to silver release and calculated the duration of silver retention in filters for different influent water chemistries. Silver

nanoparticle and dissolved ion release from filter disks painted with 0.03 mg/g casein-coated nAg or $AgNO_3$ were measured as a function of pH (5-9), ionic strength (1-50mM), and cation species (Na^+, Ca^{2+}, Mg^{2+}). Silver release occurred primarily through dissolution (as Ag^+) and cation exchange processes, regardless of silver type applied. Effluent silver levels fell below international drinking water standards after flushing with 30-42 pore volumes of 10mM $NaNO_3$ pH 7 solution. Influent water at pH 5, containing divalent cations, or at 50mM $NaNO_3$ resulted in effluent concentrations 5-10 times above standards. Silver retention ranged from 0.05-7.5 years, depending on influent water chemistry. These findings support regular filter replacement and suggest that saline and acidic influent water should be avoided to prevent high effluent silver concentrations and preserve the integrity of the silver coating. These data present a challenge to the use of CWFs, as it is unlikely that influent water can be tested or controlled in the household contexts CWFs are used within.

CHAPTER 7: RELATING NANOPARTICLE DEPOSITION IN QCM-D AND SAND COLUMNS

Introduction

Quartz crystal microbalance with dissipation (QCM-D) can be used to rapidly quantify small molecule and particle deposition behavior across a range of chemical and hydrodynamic conditions. In the QCM-D system, a thin quartz sensor is located between a pair of electrodes. When AC voltage is applied across the electrodes, the crystal is excited and oscillates. A solution containing the constituent of interest is introduced laterally over the sensor surface and depositing mass results in changes in the sensor oscillation. A nanoparticle deposition rate (Hz t^{-1}) can be obtained by monitoring the rate in frequency shift at the third overtone (Chen and Elimelech 2006):

$$k_{QCM} = {}^{d\Delta f_3}/_{dt} \qquad (29)$$

QCM-D has traditionally been used in the biological sciences to measure deposition rates of proteins, polymers, surfactants, and cells onto biologically relevant surfaces in aqueous media. It has recently seen increased use as a tool for examining interactions between colloids and environmental surfaces under different solution chemistries (Table 8). Key observations from these prior studies include increased nanoparticle deposition with increasing ionic strength and at pH values near the point-of-zero charge (PZC) of the nanoparticle, as well as decreased deposition in the presence of humic and fulvic substances. A few studies also reported a sharp decrease in deposition at high ionic strengths due to

aggregation and reduced diffusive transport of large aggregates toward to sensor surface (Chen and Elimelech 2006; Quevedo et al. 2014).

Although QCM-D can provide qualitative or relative comparisons of nanoparticle affinity for a surface, the applicability of QCM-D results to transport behavior in porous media has not been fully assessed. Nanoparticle transport in porous media is typically evaluated through one-dimensional column experiments which generate effluent breakthrough and solid-phase retention data. Classical filtration theory (CFT) (Yao et al. 1971) and its modifications (e.g., Li et al. 2008) are regularly used to simulate and predict transport behavior as a function of suspension characteristics, porous media properties, and flow conditions. The transport and deposition of colloids in porous media can be described by the one-dimensional advection-dispersion equation,

$$\frac{\partial C}{\partial t} + \frac{\rho_b}{\theta}\frac{\partial S}{\partial T} = D_h \frac{\partial^2 C}{\partial t} - v_p \frac{\partial C}{\partial x} \quad (12)$$

where C is the aqueous phase concentration, ρ_B is the bulk density of the porous medium, θ is the volumetric water content, S is the solid-phase concentration, D_h is the hydrodynamic dispersion, v_p is the pore water velocity and x is distance.

The kinetics of attachment to the solid phase can be described by a first order decay rate (k_{att}):

$$\frac{\rho_b}{\theta}\frac{\partial S}{\partial T} = k_{att} C \quad (13)$$

Two previous QCM-D studies conducted complementary sand column experiments (Quevedo et al. 2014; Liu et al. 2012), and reported discrepancies in deposition behavior between the two systems. Nanoparticles were generally found to have greater mobility in QCM-D compared with sand columns, which was attributed to differences in flow geometry and surface heterogeneity. Quevedo et al. (2014) also suggested that QCM-D measurements of nanoparticle deposition should be interpreted with caution as sensor response cannot be always directly correlated with deposited mass, particularly in the presence of large aggregates. While these studies provided some insight into the significance of QCM-D data, flow geometry and the surface area available for deposition within the QCM-D system remain poorly understood. In addition, QCM-D deposition rates (k_{QCM}) have not yet been compared with fitted attachment rates derived from traditional column experiments (e.g., k_{att}).

In this study, corresponding sand column and QCM-D experiments with three different nanoparticles (silver, fullerene, and iron oxide) were conducted. DLVO theory was used to predict nanoparticle deposition behavior as a function of collector (sensor or porous media) surface charge and chemical conditions. Sand columns were packed with 40-50 mesh Ottawa sand or glass beads and saturated with different concentrations of $NaNO_3$, NaCl, or $CaCl_2$. QCM experiments were performed under identical chemical conditions using silicon dioxide-coated sensors. QCM-D flow rates equivalent to the linear velocities (7.7, 11.4, and 15.2 m/d) used in sand column experiments were determined by considering flow geometry in the QCM-D sensor chamber. When nanoparticle deposition was

observed in both QCM-D and columns, QCM-D rates were scaled by the specific surface area (area exposed to flow/volume of fluid) of the porous media and compared with fitted attachment parameters from column experiments.

Table 8. Summary of prior nanoparticle studies using quartz crystal microbalance with dissipation (QCM-D)

Nanoparticle	Reference	C_0 and Flow Rate*	Primary Diameter	Major Findings
Ag	Thio et al. 2011b	10 mg/L 0.1 mL/min	80 nm	Negligible deposition on silica in seawater and freshwater except at low pH (<5) and high IS (100 mM $CaCl_2$)
C_{60}	Chen and Elimelech 2006	10 mg/L 0.1 mL/min	50-60 nm	Increasing deposition on silica with increasing ionic strength in NaCl and $CaCl_2$. Minimal deposition above CCC due to aggregate formation.
CeO_2	Liu et al. 2012	50 mg/L 0.1 mL/min	170 nm	Deposition on silica in NaCl dependent on pH. Large aggregates were more mobile. Presence of stabilizing agents enhanced mobility in QCM.
SiO_2	Quevedo et al. 2014	10 mg/L 0.4 mL/min	70 nm	Deposition decreased with increasing ionic strength due to aggregate formation.
TiO_2	Thio et al. 2011a	10 mg/L 0.1 mL/min	250 nm	Presence of humic acid hindered deposition in NaCl solutions
TiO_2	Fatisson et al. 2009	10 mg/L 0.4 mL/min	250 nm	Highest deposition on silica measured near PZC in $NaNO_3$ (attractive electrostatic interactions)
ZnO	Jiang et al. 2012	10 mg/L 0.1 mL/min	300 nm	Reduced deposition on humic-coated surfaces compared with silica in NaCl and $CaCl_2$

*C_0 refers to injection concentration

Flow Geometry and Scaling Factors

Deposition rates obtained from QCM were converted from Hz/min to 1/h using the following relationship:

$$\Delta f = -\frac{C}{A}\Delta m \qquad (32)$$

where C is a sensor-specific constant (17.7 ng/Hz/cm^2 for a 5 MHz crystal), A is the surface area of the sensor (154 mm^2 for a standard 14 mm sensor), and Δm is the mass applied (e.g., 1800 ng for a 30 min-0.02 mL/min injection of 5 mg/L nMag).

Dimensions of the QCM-D sensor chamber were obtained from the manufacturer (Q-Sense AB, Sweden) and used to approximate the linear velocity during sample injection. The QCM-D sensor chamber was assumed to be cylindrical in shape with a rectangular cross section equal in length to the diameter of the sensor (14 mm). The height of fluid above the sensor was calculated using the volume of fluid above the sensor given by Q-Sense (40 µl) and the surface area of the circular sensor. Flow rates in sand columns (2.5 cm diameter) and the QCM-D system at equivalent linear velocities are shown in Table 9.

Table 9. Flow rates as a function of linear velocity in QCM-D and sand columns

Linear Velocity (m/d)	Column Flow Rate (mL/min)	QCM Flow Rate (mL/min)
7.7	1.0	0.02
11.5	1.5	0.03
15.2	2.0	0.04
39.6	5.2	0.1
158	20.8	0.4

Previous nanoparticle deposition experiments with QCM-D were conducted at flow rates of 0.1-0.4 mL/min, equivalent to linear velocities of 39.6-158 m/d. These velocities are more than 3-fold higher than those used in most column transport studies (e.g., Liang et al. 2013; Taghavy et al. 2013) and also considerably higher than any velocities realistically encountered in porous media. The lower limit for flow in QCM-D was approximately 0.02 mL/min. Thus, QCM-D flow rates of 0.02-0.04 mL/min (7.7-15.2 m/d) were selected to more closely mimic experimental conditions in sand columns.

Specific surface area (SSA) in QCM-D and sand columns was determined by considering the area exposed to flow and the volume of the fluid bed (Table 8). The area exposed to flow (available for deposition) in the QCM-D system was taken as the surface area of the sensor, while area in sand columns was calculated based on the mass-based specific surface area of the porous media and the mass of sand in a column. The volume of the fluid bed was taken as the pore volume and volume above the sensor for the QCM-D and sand column systems, respectively. The fluid-based SSA (surface area/fluid volume) was used to compare the area available for nanoparticle deposition among the different systems and derive a factor with which to scale k_{QCM} to predict attachment rates in sand columns experiments ($k_{att,pred}$). A scaling factor (SF) was determined for each porous media:

$$C = \frac{SSA_{PM}}{SSA_{QCM}} \qquad (33)$$

$$k_{att,pred} = k_{QCM} \cdot SF \qquad (34)$$

where SSA_{PM} is the fluid-based SSA of the porous media (e.g., 40-50 mesh glass beads), and SSA_{QCM} is the fluid-based SSA of the QCM-D system.

Table 10. Specific surface area values and scaling factors used to relate flow regimes in QCM-D and porous media systems

	QCM-D	40-50 mesh OS	40-50 mesh GB
Mass-Based SSA (m2/g)[a]	n/a	0.1	0.03
Area Exposed to Flow	154 mm^2	12.0 m^2	3.32 m^2
Fluid Volume[b]	40 µl	26.1 mL	27.4 mL
Fluid-Based SSA (1/L)[c]	38.5	4588	1200
Scaling Factor[d] (SSA_{PM}/SSA_{QCM})	n/a	119.2	31.2

[a]Specific surface area of sand grains determined via N_2-BET analysis
[b]Fluid volume for QCM-D and porous media are pore volume and volume above sensor, respectively
[c]Specific surface area of the fluidized bed
[d]PM = porous media

DLVO Calculations

DLVO interaction energy profiles were generated based on the methods of Guzman et al. (2006). Since nMag aggregated quickly during injection into QCM or sand columns under some conditions, the mean aggregate diameter in electrolyte solutions, rather than primary nanoparticle diameter, was used in calculations. The surface potential of the nanoparticles or aggregates was approximated from zeta potential measurements, while the surface potential of the porous media was estimated based on values reported in the literature (Kaya & Yukselen 2005; Sharma 2009; Saiers & Lenhart 2003). The surface potential of

the sensors was determined based on the methods of Thio et al. (2011) and Jiang et al. (2012) using 200-300 nm silica particles as surrogates for the SiO_2 surface.

Hamaker constants for the nanoparticle-water-silica system were derived from previously reported values for nanoparticle-nanoparticle Hamaker numbers for nC_{60} (Chen & Elimelech, 2006), nAg, and nMag (Bergstrm, 1997; Butt, et al., 2005). Hamaker constants of 4.71×10^{-21}, 2.02×10^{-20}, and 5.05×10^{-20} were calculated for $nC_{60,}$ nAg, and nMag, respectively.

Nanoparticle Deposition in QCM and Sand Columns

Magnetite Nanoparticles

Transport and deposition behavior of nMag was evaluated in QCM-D (silica-coated sensors) and column experiments (40-50 mesh Ottawa sand or 40-50 mesh glass beads) with two different electrolytes (NaCl and $CaCl_2$). The mean diameter of nMag and zeta potentials of nMag and the collector surfaces were measured or estimated at each chemical condition (Table 11) for use in DLVO calculations.

Table 11. Mean diameter of nMag and zeta potentials of nMag and collector surfaces used in DLVO calculations

Ionic Strength	Diameter (nm)	Zeta Potential (mV)			
		nMag	Ottawa Sand	Glass Beads	SiO_2 Sensor
20 mM NaCl	27.9	-47.8	-36	-55	-57
40 mM NaCl	30.5	-51.4	-34	-53	-54
50 mM NaCl	42.3	-49.2	-32	-52	-50
60 mM NaCl	53.2	-48.7	-31	-50	-48
200 mM NaCl	58.6	-48.8	-25	-42	-39
0.1 mM $CaCl_2$	44.7	-30.7	-34	-60	-50
1 mM $CaCl_2$	45.3	-24.7	-30	-55	-35
2 mM $CaCl_2$	50.2	-23.5	-28	-52	-31
3 mM $CaCl_2$	51.3	-23.7	-26	-47	-28

Interaction energy profiles were generated for nMag interactions with Ottawa sand in NaCl (Figure 49a) and $CaCl_2$ (Figure 49b). In NaCl, primary energy barriers to nMag deposition were predicted at 20 mM (13.3 k_BT) and 40 mM (0.27 k_BT), while purely attractive conditions (negative interactive energy) existed at ionic strengths of 50 mM and above (Table 12). Relatively deep secondary energy minima of -0.74 and -1.81 k_BT were also calculated at 20 and 40 mM, respectively, suggesting that particle deposition is likely to occur despite the repulsive energy near the surface. At 0.1 mM $CaCl_2$, an energy barrier of ca. 2 k_BT extended to more 100 nm from the sand grain surface at 0.1 mM (Figure 49b), indicating that minimal deposition should be expected under these conditions. At higher ionic strengths of 1 mM and 2 mM $CaCl_2$, energy barriers near the surface (ca. 4 k_BT at a separation distance of 4-5 nm) and small secondary energy minima (e.g., -0.16 k_BT at 2 mM) were predicted.

DLVO interaction energy profiles calculated for nMag deposition in glass beads (Figure 50) reflect the more negative surface charge of the beads relatively to Ottawa sand (e.g., -55 mV vs. -30mV in 1mM $CaCl_2$). In NaCl. higher energy barriers (10-12 k_BT) and more shallow energy minima (-0.6 to -1.5 k_BT) were predicted at 20 mM and 40 mM, while purely attractive conditions existed at 200 mM (Table 12). In $CaCl_2$ (1-3 mM), energy barriers for nMag-glass bead interactions were twice as high compared with those predicted in Ottawa sand and were accompanied by more shallow secondary energy minima (-0.05 to -0.1 k_BT).

Interaction energy profiles generated for nMag deposition on the silica QCM sensor in NaCl (Figure 51a) display interaction energy barriers (4-12 k_BT) which decrease with increasing ionic strength and secondary energy minima (-0.5 to -4 k_BT) which increase in depth with ionic strength. Unfavorable conditions for nMag deposition were predicted at all NaCl concentrations, except 200 mM. In $CaCl_2$, interaction energy profiles were similar in shape and magnitude to those generated for nMag deposition in Ottawa sand, except with slightly higher energy barriers and deeper secondary energy minima (Figure 51b). Across a range of ionic strengths in NaCl and $CaCl_2$, the sensor surface charge was either more negative than that of glass beads, or intermediate between those of glass beads and Ottawa sand (Table 11), consistent with higher energy barriers predicted for nMag-sensor interactions compared with porous media.

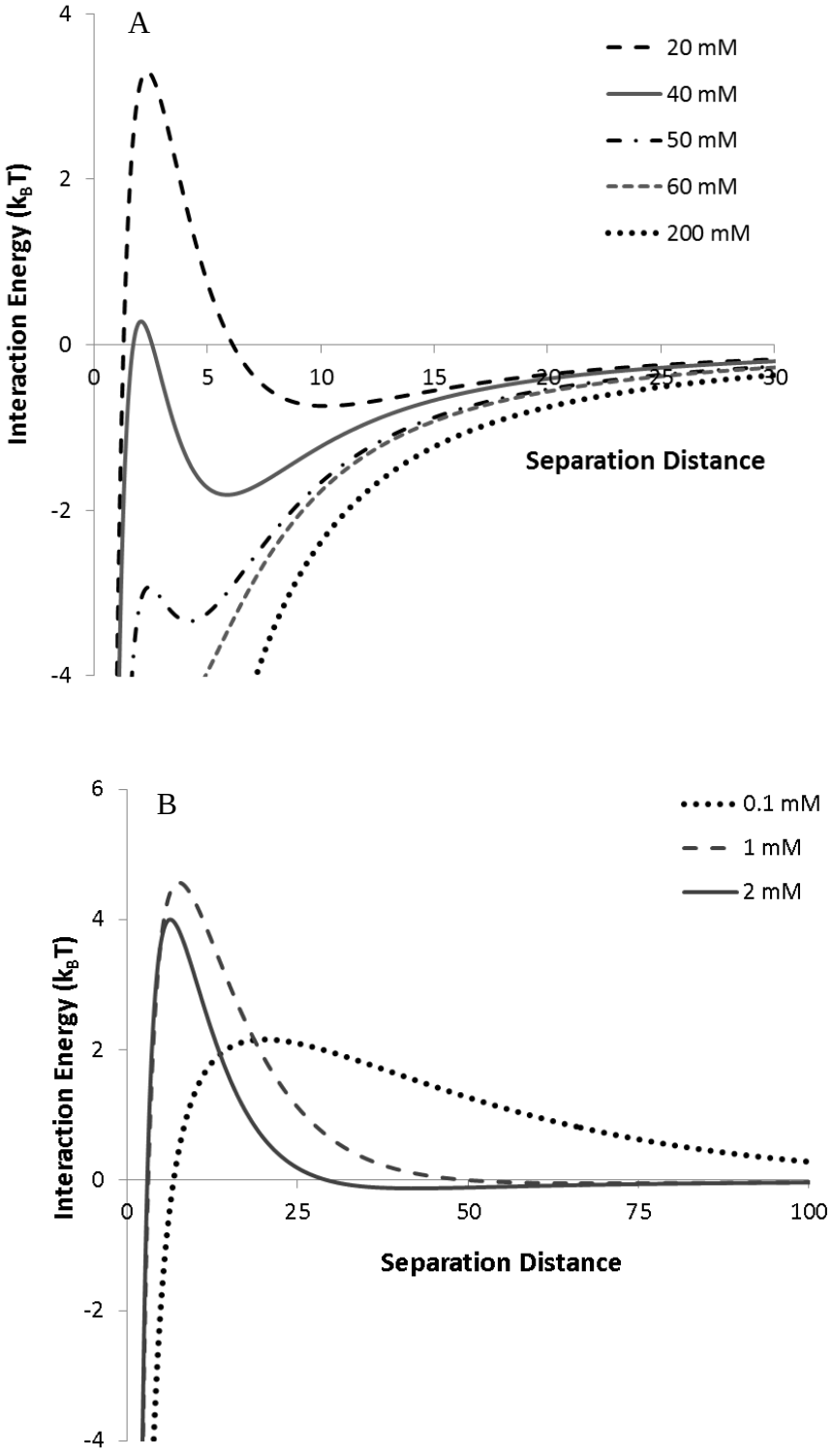

Figure 49. DLVO interaction energy profiles for nMag deposition on 40-50 mesh Ottawa sand conditioned with various concentrations of (a) NaCl and (b) $CaCl_2$

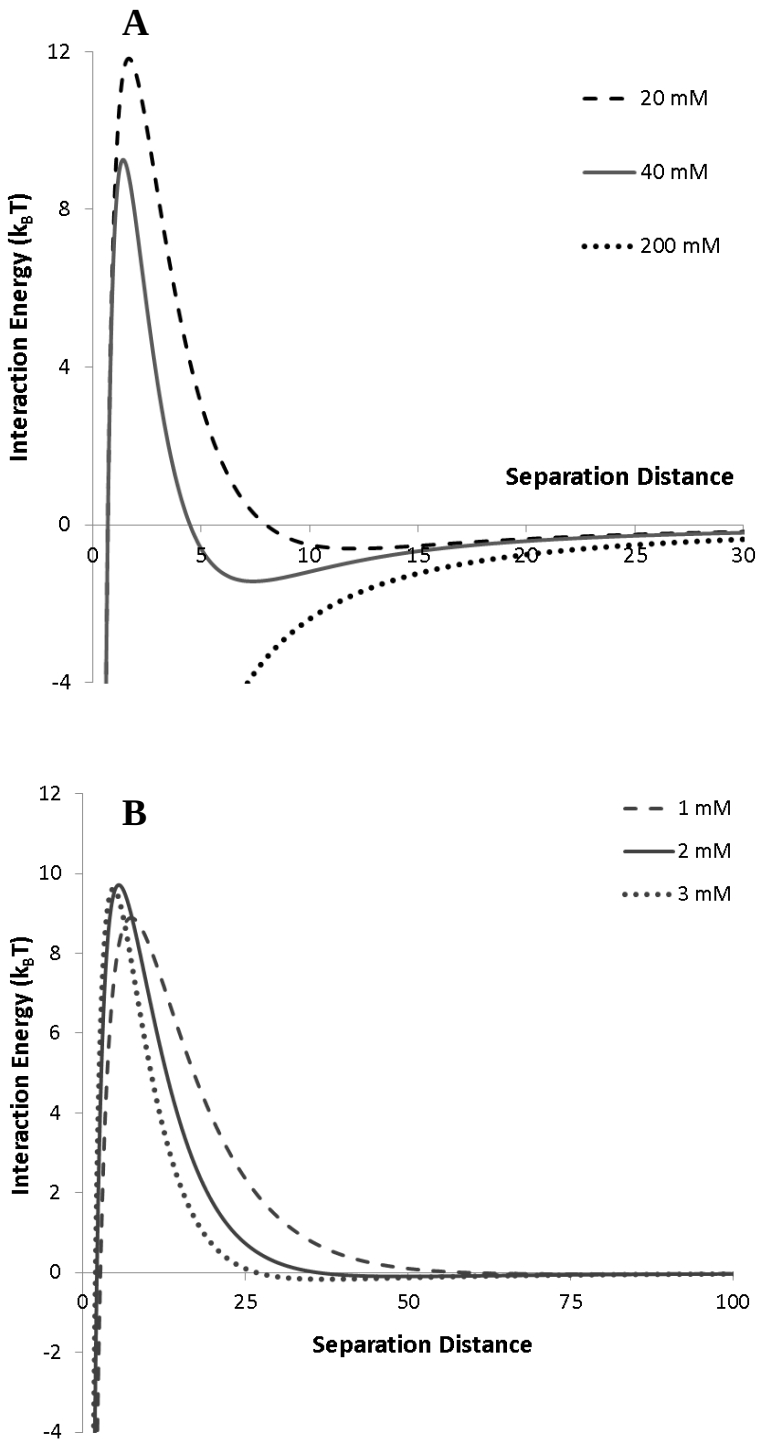

Figure 50. DLVO interaction energy profiles for nMag deposition on 40-50 mesh glass beads conditioned with various concentrations of (a) NaCl and (b) $CaCl_2$

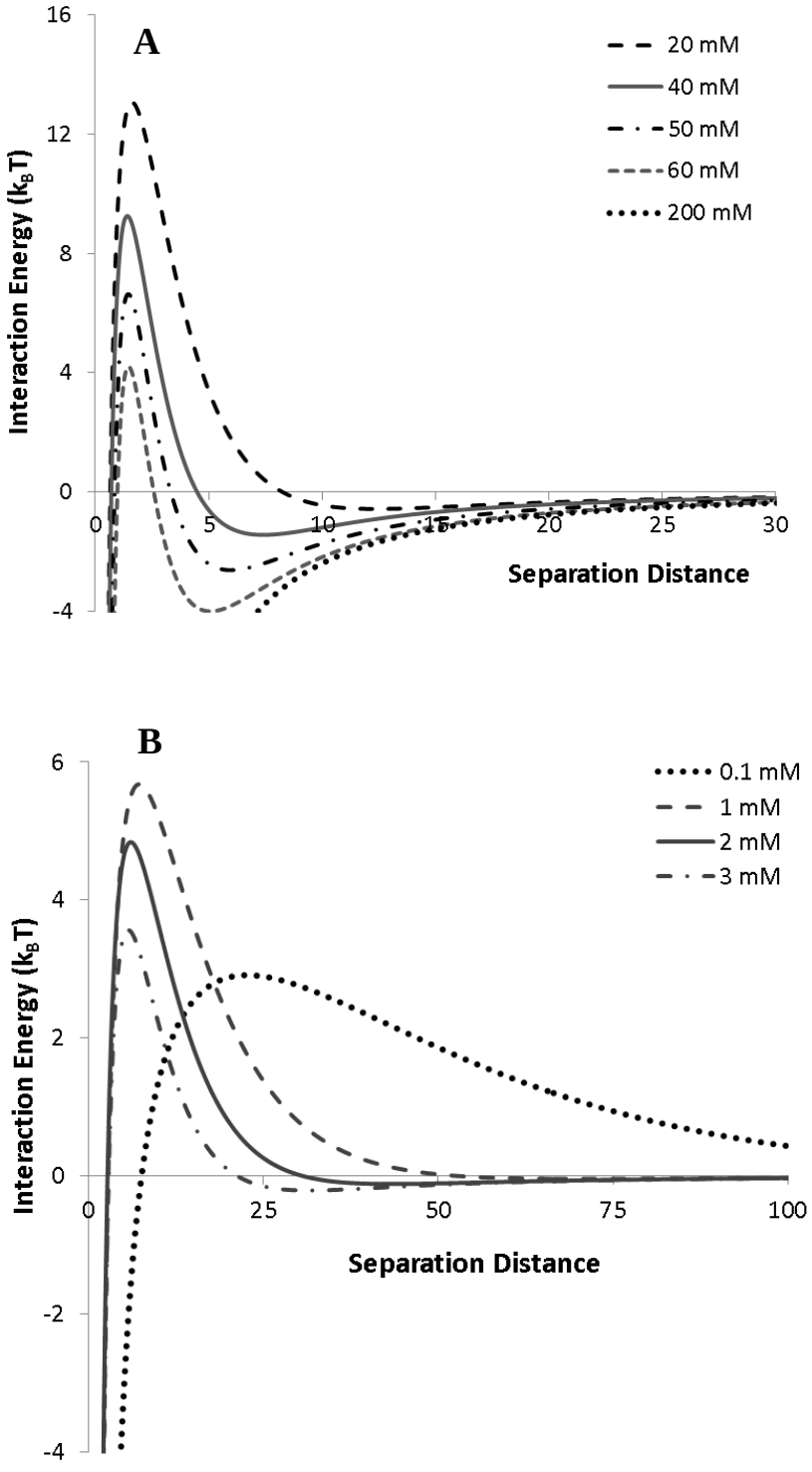

Figure 51. DLVO interaction energy profiles for nMag deposition on QCM silica sensor at various concentrations of (a) NaCl and (b) $CaCl_2$

Table 12. Height of the primary energy barrier and depth of the secondary energy minima (k_BT) calculated for nMag interactions with Ottawa sand, glass beads, and silica sensors in NaCl and $CaCl_2$

	Ottawa Sand		Glass Beads		SiO_2 Sensor	
Ionic Strength	Φ_{prim}	Φ_{sec}	Φ_{prim}	Φ_{sec}	Φ_{prim}	Φ_{sec}
20 mM NaCl	3.3	-0.74	11.8	-0.62	13.1	-0.55
40 mM NaCl	0.27	-1.81	9.3	-1.4	9.2	-1.4
50 mM NaCl	ATTR*	ATTR	n/d	n/d	6.3	-2.6
60 mM NaCl	ATTR	ATTR	n/d	n/d	4.2	-3.9
200 mM NaCl	ATTR	ATTR	ATTR	ATTR	ATTR	ATTR
0.1 mM $CaCl_2$	2.16	n/a	n/d	n/d	2.9	-0.01
1 mM $CaCl_2$	4.57	-0.05	9.5	-0.04	5.7	-0.07
2 mM $CaCl_2$	4.01	-0.16	9.6	-0.09	4.8	-0.16
3 mM $CaCl_2$	n/d	n/d	6.6	-0.11	3.6	-0.21

*Attractive conditions (no energy barrier)

In general, the highest energy barriers to nMag deposition occurred on the silica sensor surface, suggesting that nMag will exhibit greater mobility in QCM compared with Ottawa sand and glass beads. DLVO calculations also suggest that secondary energy interactions will play an important role in nMag deposition under unfavorable conditions on sand and sensor surfaces. In general, deposition is expected to occur in the following order: Ottawa sand > QCM > glass beads. However, it should be noted that DLVO theory does not account for the influences of straining, aggregation, nanoparticle shape, or surface roughness or heterogeneity on nanoparticle-collector interactions.

A total of 6 column experiments were conducted with nMag in Ottawa sand. In NaCl (Figure 52a) and $CaCl_2$ (Figure 52b), nMag deposition occurred under all

tested conditions, except at 0.1 mM $CaCl_2$. As it was not possible to accurately determine solid-phase nMag concentrations in sand, the percentage of retained mass was calculated as the difference between injected mass and eluted mass (Table 13). The time of nMag breakthrough became increasingly later (after 1 pore volume) and the percentage of mass retained in sand increased as the ionic strength was increased in both NaCl and $CaCl_2$. For example, in NaCl solutions, the time of breakthrough increased from 1.0 to 2.2 to 3.1 PV and the percentage of input nMag retained increased from 17.6 to 43.9 to 89.1 as ionic strength was increased from 20 to 40 to 50 mM, respectively. No effluent breakthrough was detected at 60 mM and 200 mM NaCl (i.e., 100% of input mass was retained in sand), consistent with net attractive interaction predicted by DLVO theory under these conditions (Figure 49). Straining and aggregation-related processes were considered negligible, as nMag diameter did not change considerably during the injection period.

The shape of breakthrough curves in nMag column experiments with Ottawa sand was asymmetrical, indicative of retention behavior consistent with an S_{max}-modified filtration theory (MFT, Li et al. 2008). The MFT model was able to capture the general shape of the breakthrough curves, and k_{att} and S_{max} generally increased with increasing ionic strength in NaCl and $CaCl_2$ (Table 13).

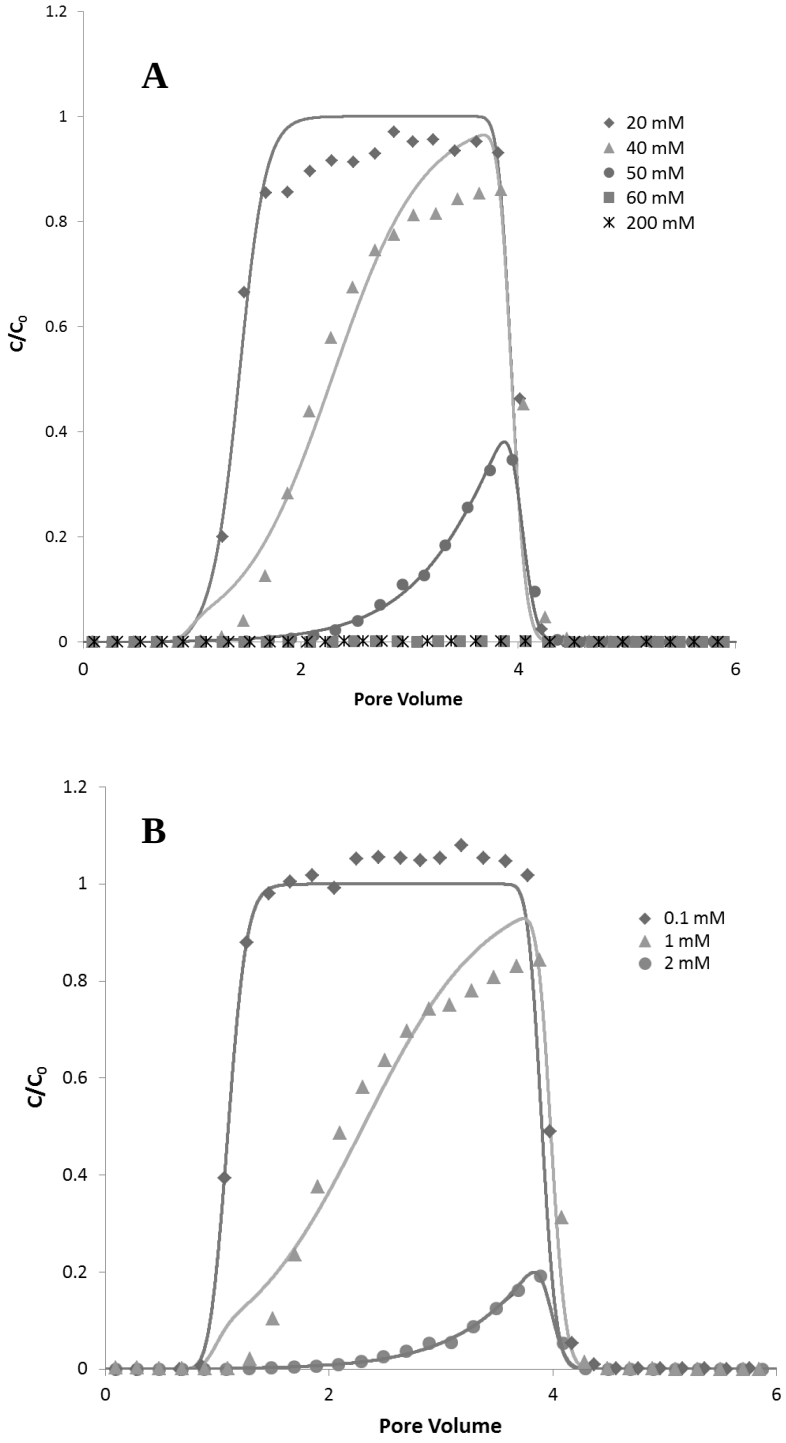

Figure 52. nMag effluent breakthrough in 40-50 mesh Ottawa sand columns with (a) NaCl and (b) $CaCl_2$ at a flow rate of 1.0 mL/min (7.6 m/d). Modified filtration theory was fit to the data.

Table 13. Experimental conditions and attachment parameters for complementary sand column and QCM-D experiments (linear velocity = 7.6 m/d)

Ionic Strength	%Retained	k_{att} (1/h)	S_{max} (ug/g)	Deposition Rate (Hz/min)	k_{QCM} (1/h)	Pred-k_{att} (1/h)
20 mM NaCl	17.6	8.47	0.49	0.025	0.023	2.71
40 mM NaCl	43.9	7.17	1.46	0.095	0.086	10.3
50 mM NaCl	89.1	14.8	3.37	0.195	0.177	21.1
60 mM NaCl	>99	NA	NA	0.220	0.200	NA
200 mM NaCl	>99	NA	NA	0.965	0.876	NA
0.1 mM CaCl2	<1	2.99	0.11	n/d	n/d	n/d
1 mM CaCl2	45.2	5.66	1.38	0.210	0.191	18.386
2 mM CaCl2	94.4	15.6	3.93	0.670	0.609	58.660

A total of 12 column experiments with nMag in mesh glass beads were conducted. The percentage of retained mass was observed to increase with increasing ionic strength in both NaCl (Figure 53) and $CaCl_2$ (Figure 54). In glass columns conducted at 3 different flow rates with 3 mM $CaCl_2$ (Figure 55), the percentage of retained mass was observed to decrease from 55.1 to 17.5 to 7.8 as flow rate was increased from 1.0 to 1.5 to 2.0 mL/min (7.6, 11.5, 15.2 m/d). Decreased retention with increasing flow rate is consistent with prior nanoparticle transport studies (e.g., Li et al. 2008; Liang et al. 2013). As in Ottawa sand columns, breakthrough curves were asymmetrical in shape, retention profiles were hyper-exponential, and time of breakthrough became increasingly later at higher ionic strengths.

The MFT model (fit to breakthrough data only) was able to capture the general shape of breakthrough curves in glass beads, but was unable to predict the high deposition near the column inlet. Fitted k_{att} values did not follow a particular trend

with ionic strength or flow rate, while S_{max} was observed to increase with increasing ionic strength and decrease with increasing flow rate (Table 14). A decrease in S_{max} with increasing velocity has been reported previously, and attributed to effects of the shear component of fluid flow around sand grains which creates a shadow zone on the collector surface down-gradient of attached particles where lower deposition can be expected (Ko and Elimelech 2000). Increasing the flow velocity is thought to result in a larger shadow zone area and reduced maximum attainable surface coverage, hence the observed decrease in S_{max} with increasing velocity (Ko & Elimelech 2000).

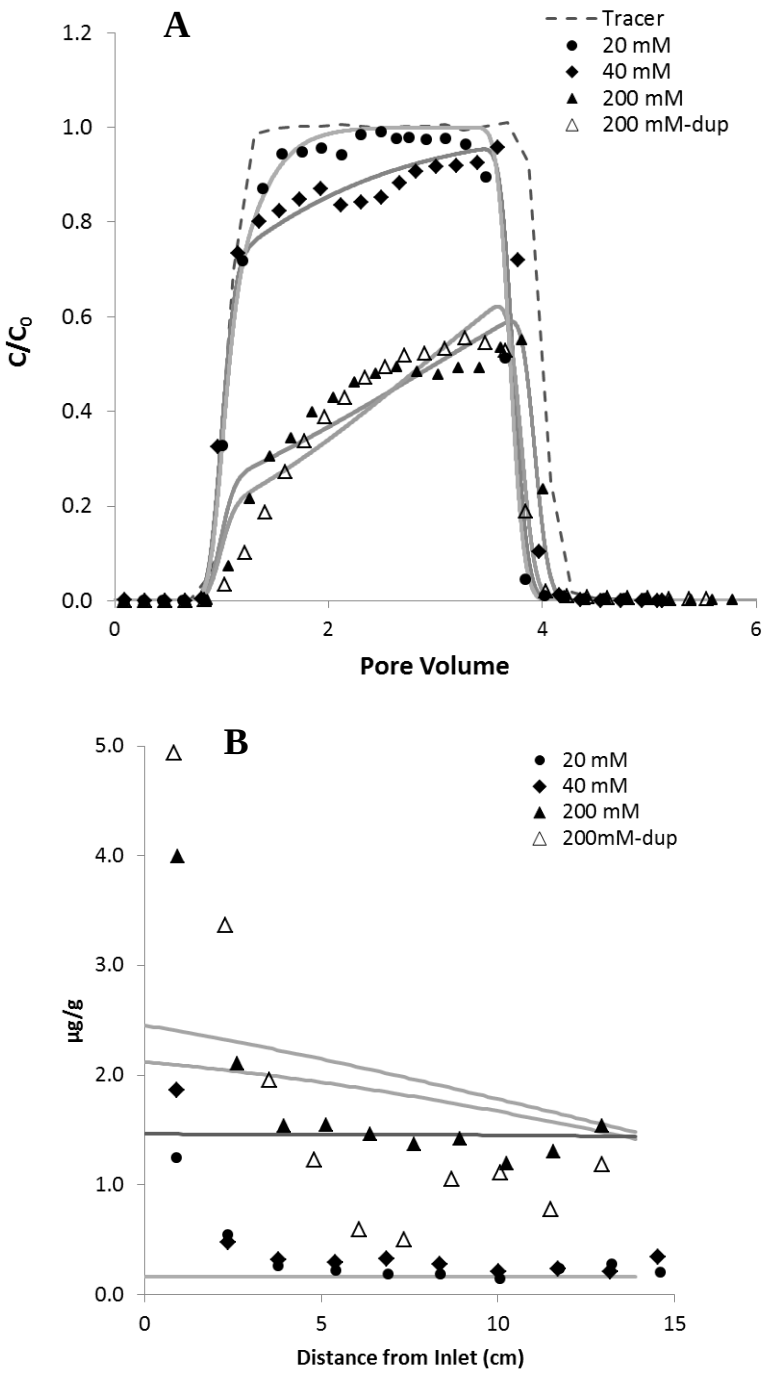

Figure 53. Effluent breakthrough curves and retention profiles for nMag transport in 40-50 mesh glass beads with NaCl at a flow rate of 1 mL/min (7.6 m/d). Modified filtration theory was fit to the data.

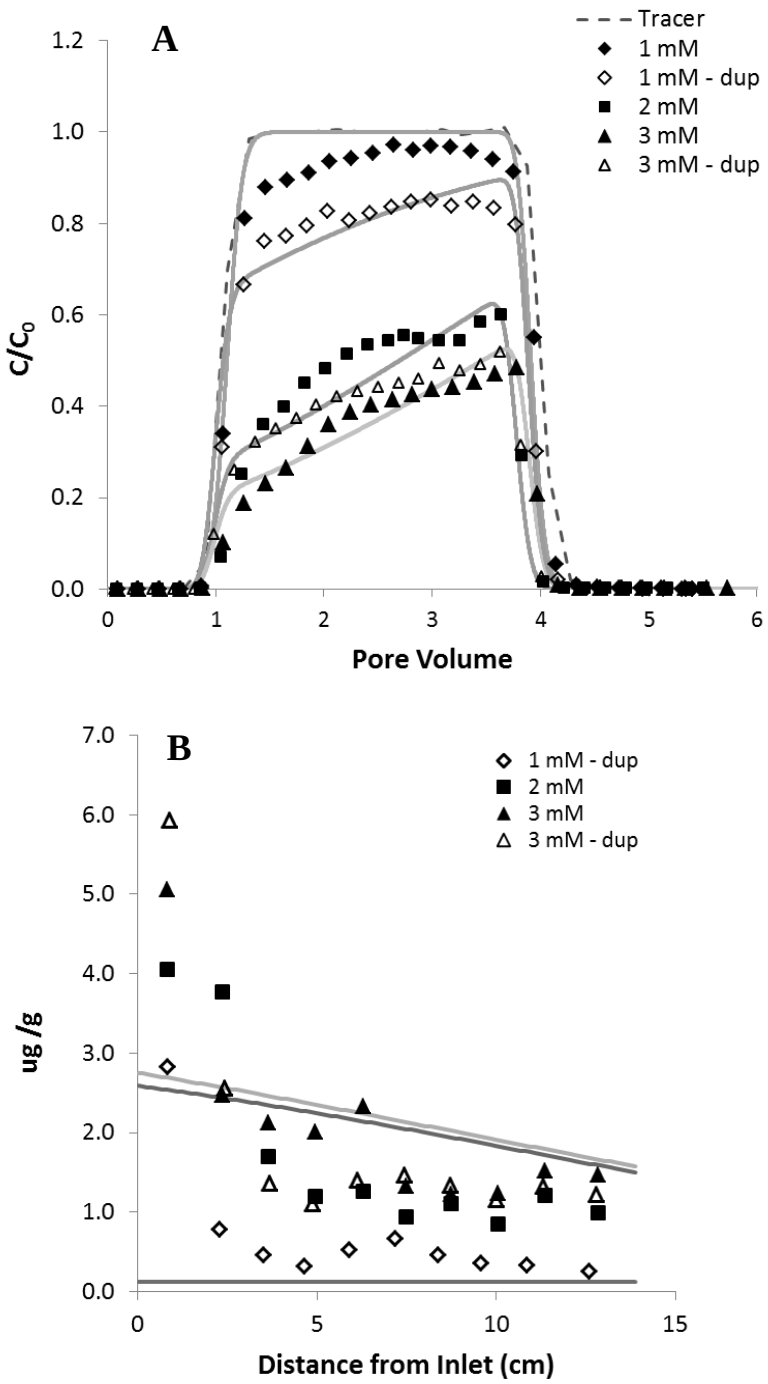

Figure 54. Effluent breakthrough curves and retention profiles for nMag transport in 40-50 mesh glass bead with CaCl2 at a flow rate of 1 mL/min (7.6 m/d). Modified filtration theory was fit to the data.

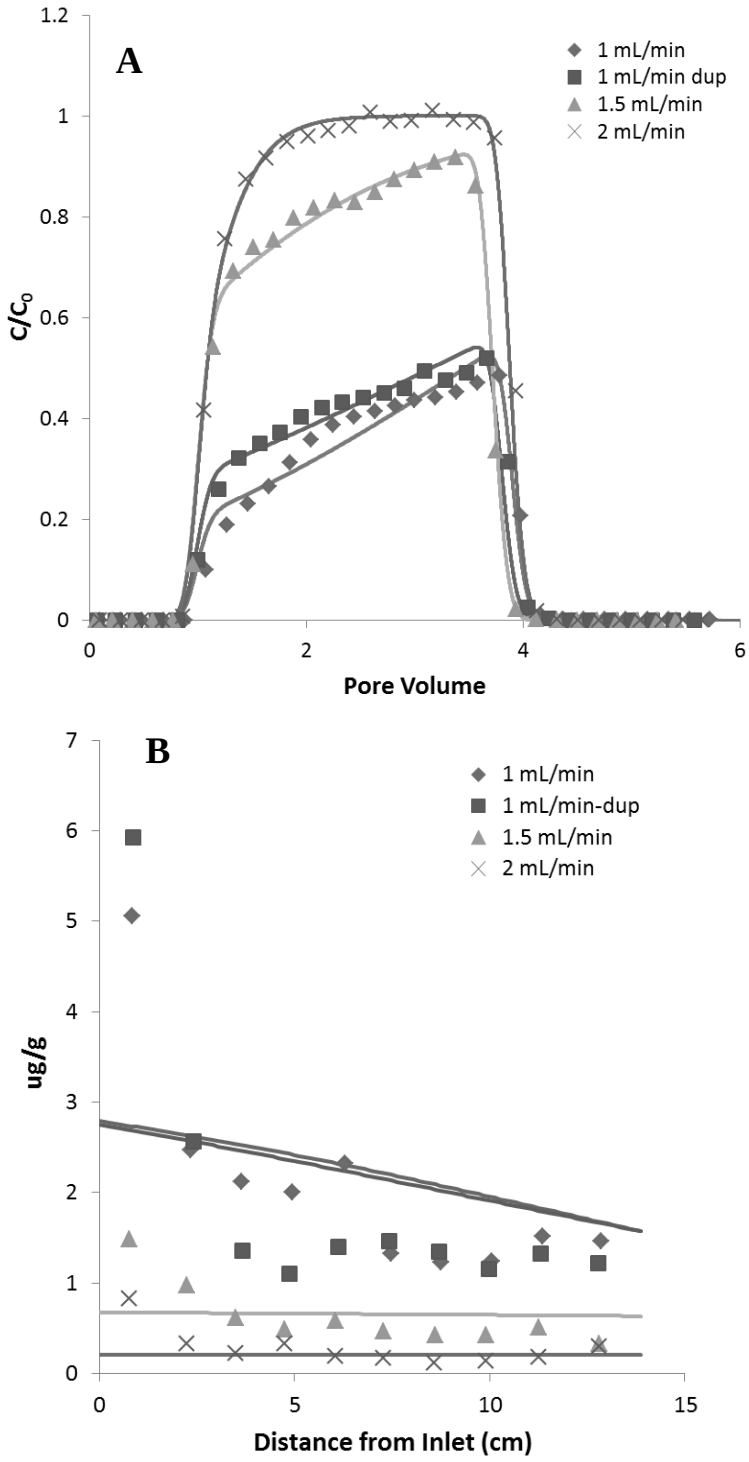

Figure 55. Effluent breakthrough curves and retention profiles for nMag transport in 40-50 mesh glass bead at various flow rates in 3 mM $CaCl_2$. Modified filtration theory was fit to the data.

Table 14. Experimental conditions and attachment parameters for glass bead columns and corresponding QCM studies with nMag

Ionic Strength	Linear Velocity (m/d)	% Retained	Mass Balance	k_{att} (1/h)	S_{max} (µg/g)	Deposition Rate (Hz/min)	k_{QCM} (1/h)	Pred-k_{att} (1/h)
20 mM NaCl	7.6	12.2	103.7	1.24	0.16	0.025	0.023	0.71
40 mM NaCl	7.6	13.6	104.8	0.753	0.543	0.095	0.086	2.69
200 mM NaCl	7.6	53.5	94.8	3.055	2.908	0.965	0.876	27.34
1 mM $CaCl_2$	7.6	21.0	100.9	1.920	0.210	0.210	0.191	5.95
2 mM $CaCl_2$	7.6	52.7	101.0	3.162	3.492	0.670	0.609	18.98
3 mM $CaCl_2$	7.6	55.1	92.4	3.512	3.371	2.245	2.039	63.59
3 mM $CaCl_2$	11.4	17.5	89.2	1.534	0.755	2.215	2.012	62.74
3 mM $CaCl_2$	15.1	7.8	102.7	2.548	0.205	2.175	1.975	61.61

In QCM-D experiments, nMag deposition occurred under all tested conditions and was highly sensitive to changes in ionic strength. For example, k_{QCM} increased from 0.025 to 0.095 Hz/min as NaCl concentration was increased from 20 mM to 40 mM, and from 0.21 to 0.67 Hz/min as $CaCl_2$ concentration was increased from 1 mM to 2 mM. The QCM deposition rate was converted to units of 1/h and scaled by factors of 119.2 and 31.2 (see Table 10) to predict attachment rates in Ottawa sand and glass beads, respectively (Table 15). In Ottawa sand, predicted attachment rates were in fairly good agreement with fitted values for experiments at three different NaCl concentrations (Figure 56). Scaled QCM data over-predicted k_{att} approximately 4-fold at 20 mM NaCl. This discrepancy may be due to the inability of the MFT model to fully capture the asymmetrical breakthrough behavior at 20 mM (Figure 53a). In $CaCl_2$ solutions, deposition occurred at much higher relative rates in QCM compared with NaCl, and thus QCM data substantially over-predicted column attachment rates.

In glass beads, QCM data over-predicted nMag attachment rates by 4-20-fold under all tested conditions except at 20 mM NaCl (Table 14). Contrary to results from column experiments, nMag deposition in QCM was not sensitive to flow rate in 3 mM $CaCl_2$ solutions, with measured deposition rates of ca. 2.0 Hz/min at 0.02, 0.03, and 0.04 mL/min (7.7, 11.5, 15.2 m/d). Discrepancies between the fitted and QCM-predicted k_{att} values are likely partially due to the lack of sensitivity of the fitted attachment rates to ionic strength and flow rate in glass beads. In addition, glass beads (soda lime glass) may not accurately represent the

SiO_2 surface of the QCM sensors, leading to difficulties relating deposition behavior between the two systems.

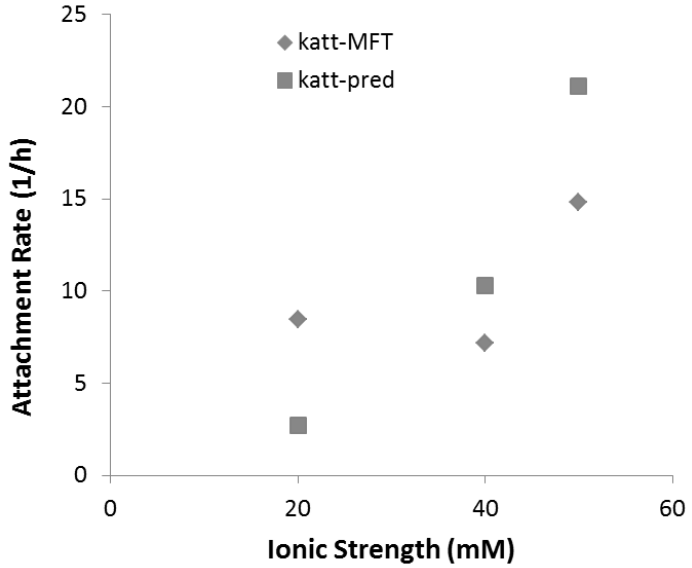

Figure 56. Fitted and QCM-predicted attachment rates as a function of ionic strength (NaCl)

Silver Nanoparticles

Transport and deposition behavior of nAg was evaluated in QCM experiments (silica sensors) and sand columns (washed and unwashed 40-50 mesh Ottawa sand) in $NaNO_3$ solutions. The mean diameter of nAg and surface charge of nAg, Ottawa sand, and the silica sensor were calculated as a function of ionic strength for use in DLVO calculations (Table 15).

Table 15. Diameters of nAg and zeta potentials of nAg, Ottawa sand, and SiO_2 sensor as a function of $NaNO_3$ concentration

Ionic Strength (mM)	Size (nm)	Zeta Potential (mV)		
		nAg	Sand	Sensor
10	10.8	-45.2	-45	-59
12	12.1	-41.0	-43	-54
20	11.8	-38.8	-39	-51
30	12.2	-37.2	-37	-48
40	11.9	-35.5	-33	-46

DLVO interaction energy profiles were generated for nAg interactions with Ottawa sand (Figure 57a) and QCM sensors (Figure 57b) as a function of ionic strength and show that repulsive conditions exist under all tested conditions for nAg-collector interactions. The height of the primary energy barrier and depth of the secondary energy minima increased as ionic strength was increased for nAg deposition in sand and QCM (Table 16). The height of the primary energy barriers increased from 0.5-1.5 k_BT to 2-4 k_BT for the sand and silica sensor, respectively, indicative of the more negative surface charge of the sensor. These DLVO theory calculations suggest that nAg will be considerably more mobile in QCM compared with sand columns.

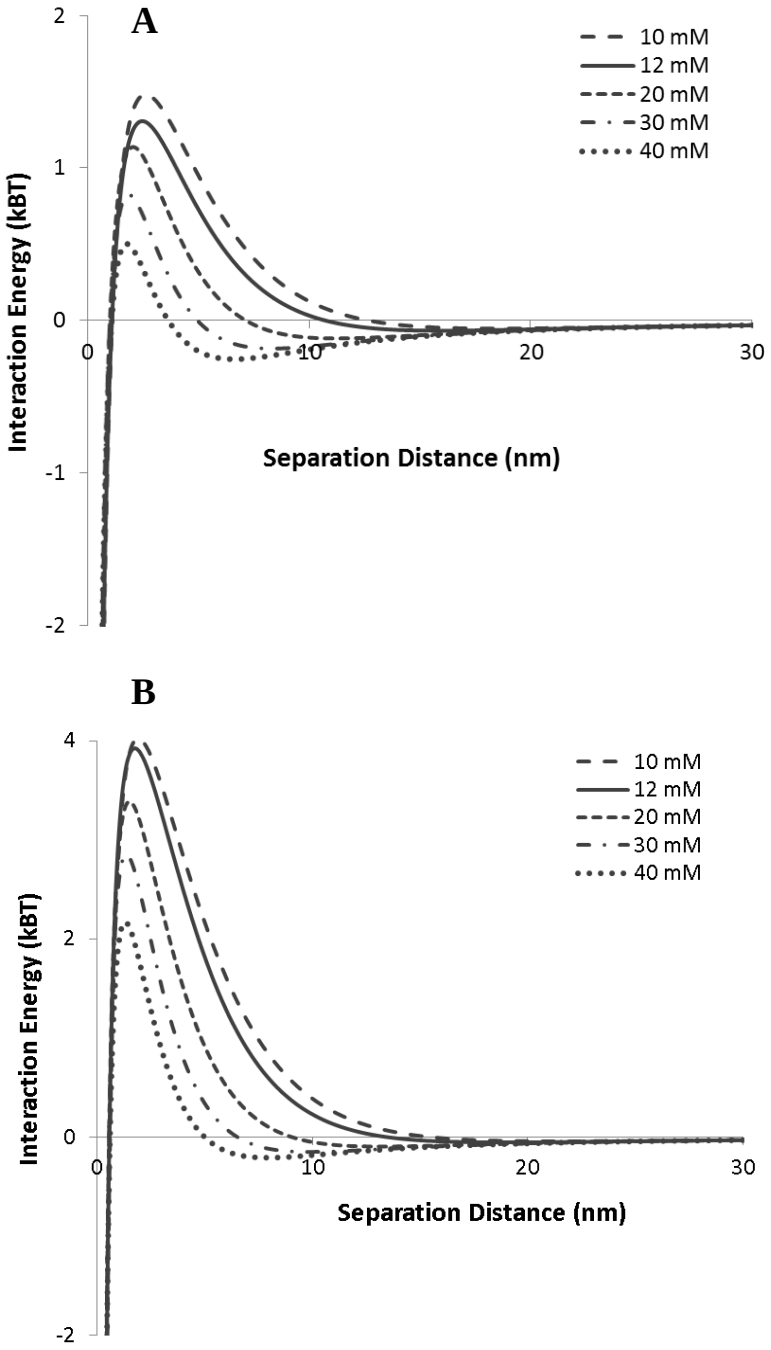

Figure 57. DLVO interaction energy profiles for nAg interactions with (a) Ottawa sand and (b) SiO_2 sensor in $NaNO_3$

Table 16. Height of primary energy barrier and depth of secondary energy minima (k_BT) for nAg-collector interactions in $NaNO_3$

Ionic Strength (mM)	Sand		Sensor	
	Φ_{prim}	Φ_{sec}	Φ_{prim}	Φ_{sec}
10	1.48	-0.09	4.1	-0.06
12	1.31	-0.12	3.9	-0.09
20	1.14	-0.16	3.4	-0.14
30	0.82	-0.23	2.9	-0.19
40	0.51	-0.25	2.2	-0.21

The effect of ionic strength ($NaNO_3$) on nAg transport and retention was evaluated in 3 columns with washed Ottawa sand (Figure 58) and 3 columns with unwashed Ottawa sand (Figure 59). In washed sand, effluent breakthrough began at 1 pore volume and continued to increase over the duration of the pulse. In unwashed sand, the time of breakthrough was delayed (1.5-2 pore volumes) and breakthrough curves plateaued at a near-constant C/C_0 value, in contrast to asymmetrical breakthrough observed in washed sand. Greater retardation of nAg in unwashed sand columns likely results from the presence of positively-charged iron and aluminum oxides and other impurities on the sand surface. The percentage of retained mass increased with increasing strength in both washed and unwashed sand (Table 17), consistent with increased compression of the electrical double layer at higher salt concentrations. In unwashed sand, 11.7, 33.9, 76.9 and 97.7% of input mass was retained in columns at 10, 12, 20, and 30 mM $NaNO_3$, respectively. Hyper-exponential retention profiles were observed in all column experiments with nAg.

The effect of flow rate on nAg transport and retention was also explored in column experiments with washed Ottawa sand conditioned with 40 mM $NaNO_3$ (Figure 60). At three flow rates tested, effluent breakthrough began at ca. 1 PV and was asymmetric in shape. Consistent with filtration theory, nAg attachment in sand columns was observed to decrease with increasing flow rate. The percentage of retained mass at 1.0, 1.5, and 2.0 mL/min (7.6, 11.4, and 15.1 m/d) was 60.6, 45.9, and 25.8, respectively. Retention profiles were hyper-exponential at all three flow rates tested.

While the modified filtration theory (MFT) model was able to adequately fit nAg effluent breakthrough data, the model could not capture the higher-than-expected retention in the first 2-3 cm of columns. Both k_{att} and S_{max} were found to increase with increasing ionic strength in unwashed and washed sand (Table 17), with nearly linear relationships observed in unwashed sand (Figure 61). In washed sand columns at different flow rates, k_{att} increased with velocity, while S_{max} was inversely proportional with velocity (Figure 62). This behavior is consistent with classical filtration theory and the shadow effect described previously (Ko and Elimelech 2000).

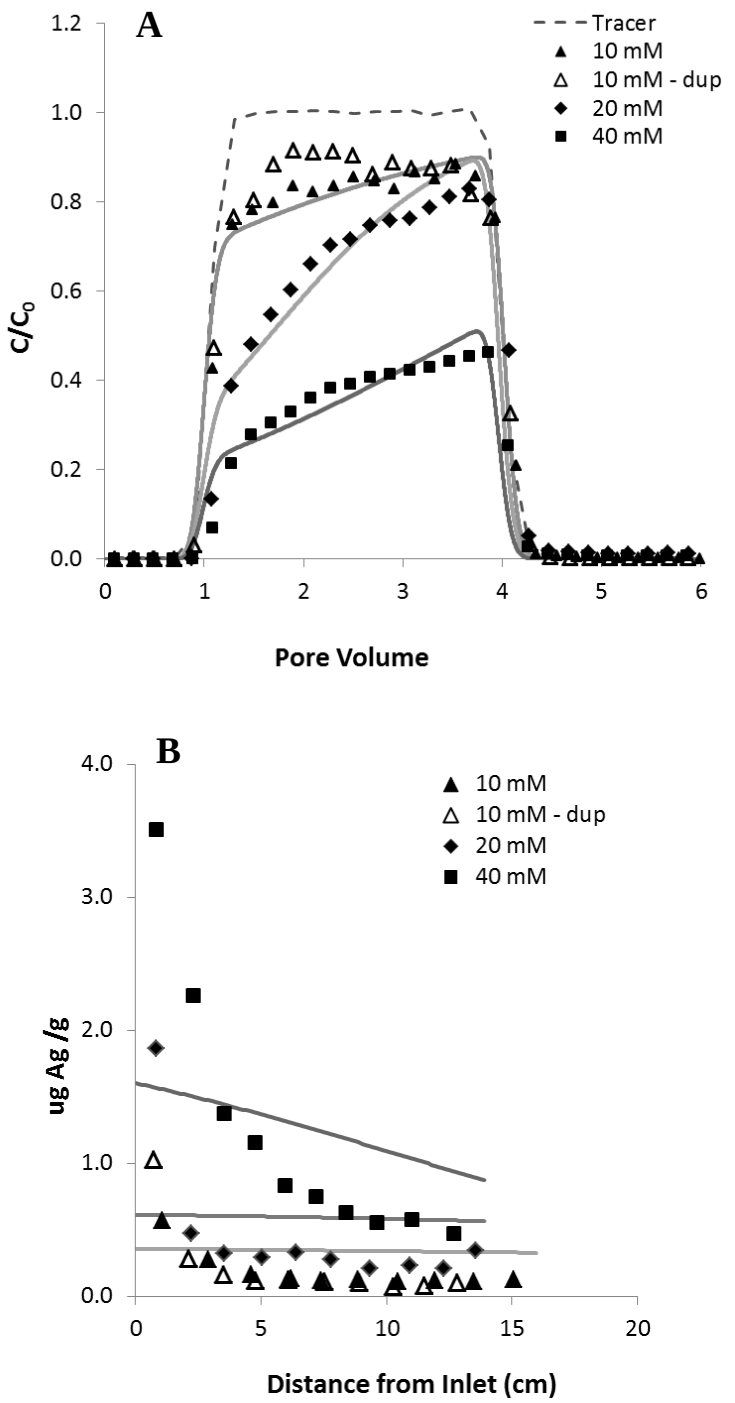

Figure 58. Effect of ionic strength on nAg effluent breakthrough and retention in washed 40-50 mesh Ottawa sand at 1 mL/min (7.6 m/d). Modified filtration theory was fit to the data.

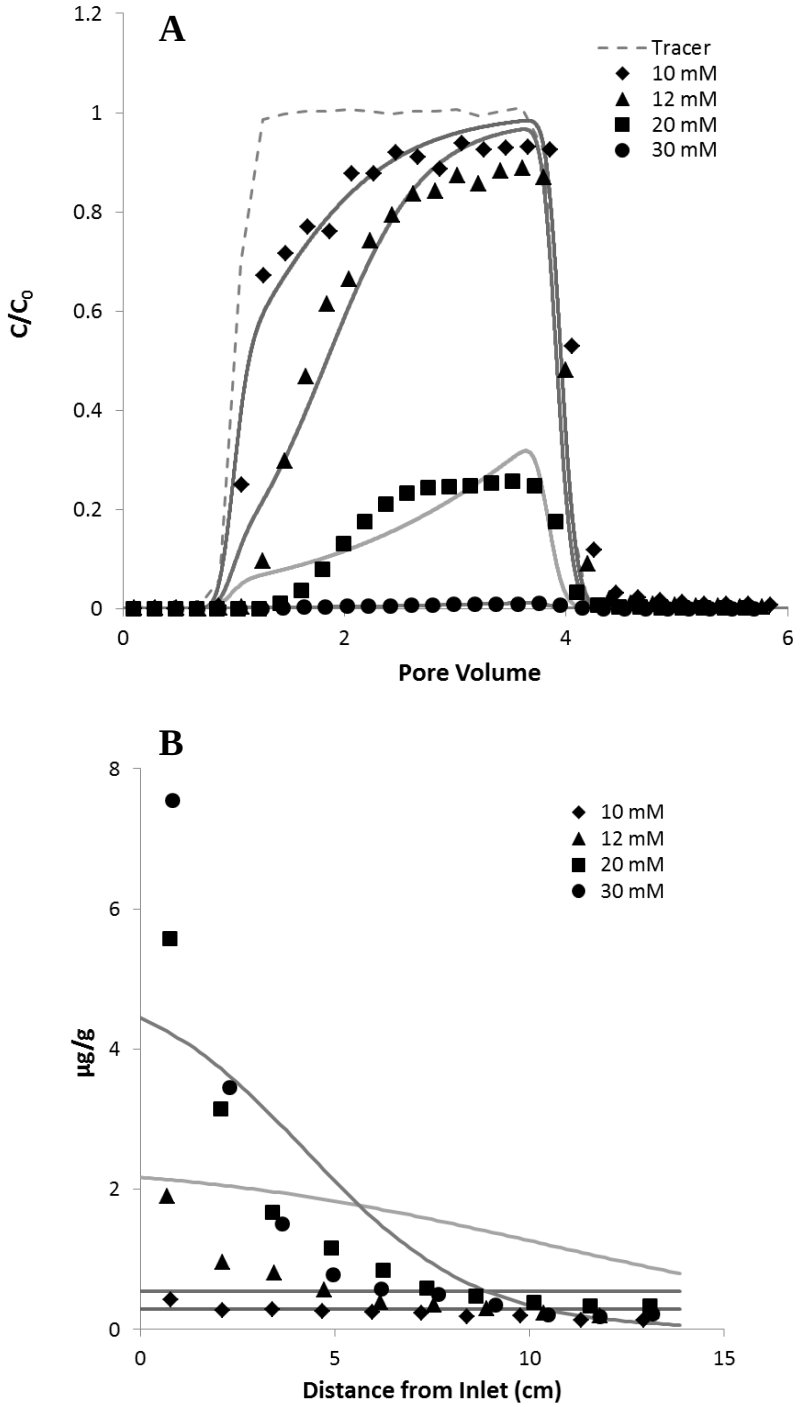

Figure 59. Effect of ionic strength on nAg effluent breakthrough and retention in unwashed 40-50 mesh Ottawa sand at 1 mL/min (7.6 m/d). Modified filtration theory was fit to the data.

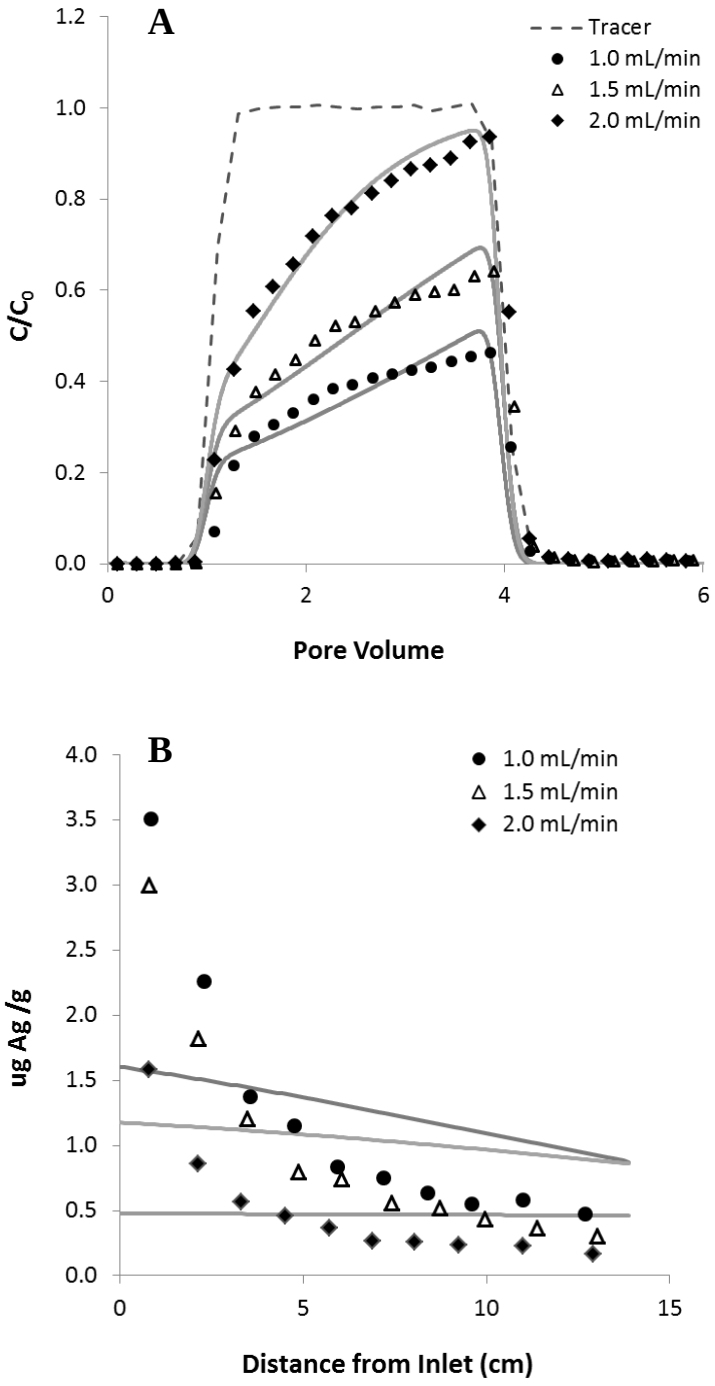

Figure 60. Effect of flow rate on nAg effluent breakthrough and retention in washed 40-50 mesh Ottawa sand at 40 mM $NaNO_3$. Modified filtration theory was fit to the data.

Table 17. Column conditions and fitted attachment parameters for nAg column studies

Expt. #	Ionic Strength ($NaNO_3$)	Linear Velocity (m/d)	Porous Media	% Retained	% Mass Balance	katt (1/h)	Smax (ug/g)
1	10 mM	7.6	40-50 mesh OS	9.9	92.4	0.71	0.46
2	20 mM	7.6	40-50 mesh OS	26.6	96.2	2.50	0.64
3	40 mM	7.6	40-50 mesh OS	60.6	98.8	3.47	2.10
4	40 mM	11.4	40-50 mesh OS	45.9	98.5	4.28	1.38
5	40 mM	15.1	40-50 mesh OS	25.8	103.3	4.78	0.48
6	10 mM	7.6	40-50 mesh OS*	11.7	100.2	1.57	0.29
7	12 mM	7.6	40-50 mesh OS*	33.9	103.4	4.58	0.55
8	20 mM	7.6	40-50 mesh OS*	76	93.4	6.68	2.41
9	30 mM	7.6	40-50 mesh OS*	97.7	98.3	15.1	5.05

*indicates unwashed sand

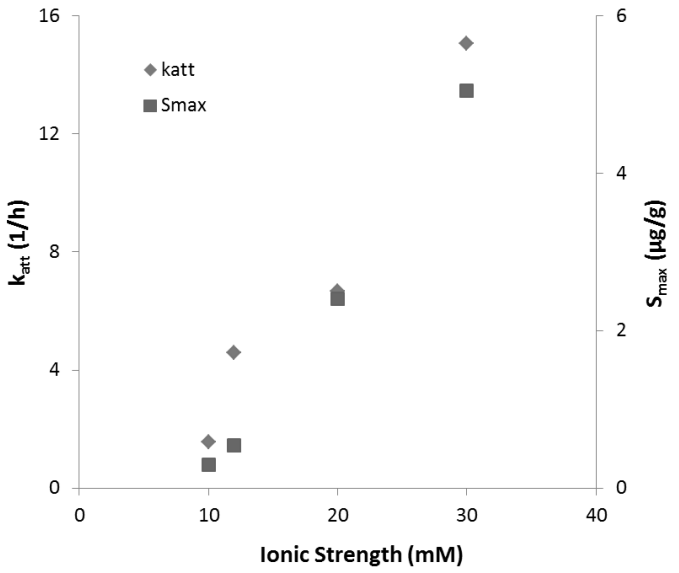

Figure 61. Variation in fitted k_{att} and S_{max} with ionic strength for nAg columns with unwashed Ottawa sand

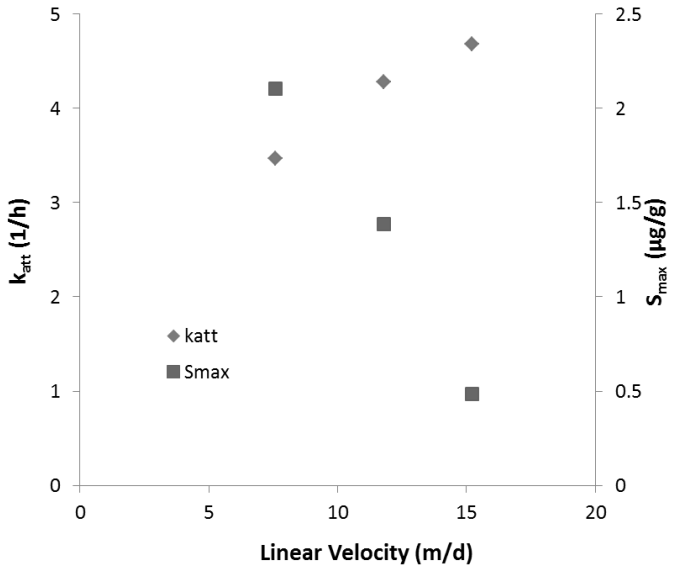

Figure 62. Variation in fitted k_{att} and S_{max} with flow rate for nAg columns with washed Ottawa sand

No nAg deposition occurred on silica sensors in QCM experiments under conditions identical to those used in sand columns (Table 18). Deposition on silica was only observed at very high ionic strengths (above 200 mM in $NaNO_3$, above 400 mM in NaCl, and above 5 mM in $CaCl_2$). Deposition also occurred on sensors coated with the positively charged polymer, poly-L-lysine (PLL, data not shown); however, deposition rate was not sensitive to ionic strength, with rates of ca. 0.55 Hz/min measured at 10, 20, and 40 mM $NaNO_3$ on PLL sensors. The lack of nAg deposition onto silica is consistent with results presented by Thio et al. (2011) in which no significant deposition occurred except at low pH (4-5) and very high ionic strength (100 mM $CaCl_2$) where repulsive forces between nAg and silica were effectively neutralized.

Table 18. Deposition rates of nAg on silica sensor measured by QCM

Ionic Strength	k_{QCM} (Hz/min)
10 mM $NaNO_3$	n/d
20 mM $NaNO_3$	n/d
40 mM $NaNO_3$	n/d
100 mM $NaNO_3$	n/d
200 mM $NaNO_3$	0.018
300 mM $NaNO_3$	0.011
400 mM $NaNO_3$	0.011
400 mM NaCl	0.082
600 mM NaCl	0.123
5 mM $CaCl_2$	0.128

Fullerene (nC_{60}) Nanoparticles

Transport and deposition behavior of nC_{60} was evaluated in QCM (silica sensors) and sand columns (washed 40-50 mesh Ottawa sand) in NaCl and $CaCl_2$. The

mean diameter of nC_{60} and zeta potential of nC_{60} and collector surfaces were measured or estimated as a function of electrolyte concentration (Table 19).

Table 19. Size and zeta potentials of nC_{60}, Ottawa sand, and SiO_2 sensors in NaCl and $CaCl_2$ used in DLVO calculations

Ionic Strength	Size* (nm)	Zeta Potential (mV)		
		nC_{60}	Ottawa Sand	Sensor
3 mM NaCl	92.7	-55	-55	-67
10 mM NaCl	94.8	-48	-45	-59
30 mM NaCl	225	-44	-35	-54
3 mM $CaCl_2$	121	-21	-30	-35
10 mM $CaCl_2$	273	-15	-27	-31
30 mM $CaCl_2$	817	-11.9	-22	-26

*Mean diameter in injection suspension. Primary particle size was 92-95 nm.

Interaction energy barriers for nC_{60} deposition on Ottawa sand and silica sensors in NaCl (Figure 63) and $CaCl_2$ (Figure 64) show the presence of strong repulsive interactions for all tested conditions. Very large energy barriers to deposition were predicted for nC_{60} interactions with Ottawa sand (100-160 k_BT) and silica sensors (140-275 k_BT) in NaCl solutions (Table 20). In $CaCl_2$, smaller energy barriers ranging in height from 30-60 k_BT and 40-50 k_BT were predicted for nC_{60} deposition on sand and SiO_2 sensors, respectively. Relatively shallow secondary energy minima were also present, with the strongest interactions predicted at 30 mM (-0.4 k_BT and -2.1 k_BT in NaCl and $CaCl_2$, respectively).

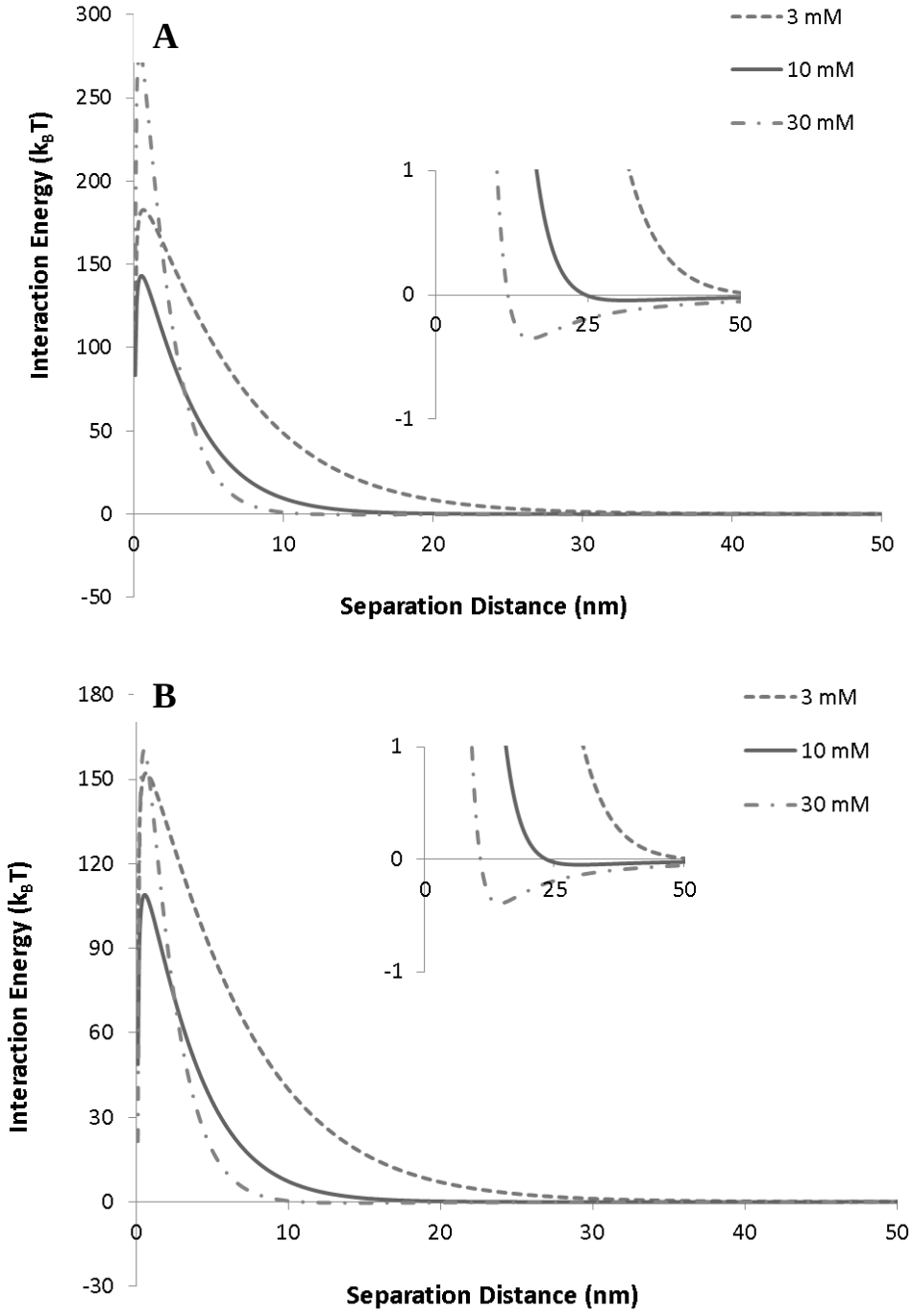

Figure 63. DLVO interaction energy profiles for nC_{60} interactions with (a) sand and (b) SiO_2 sensor in NaCl solutions

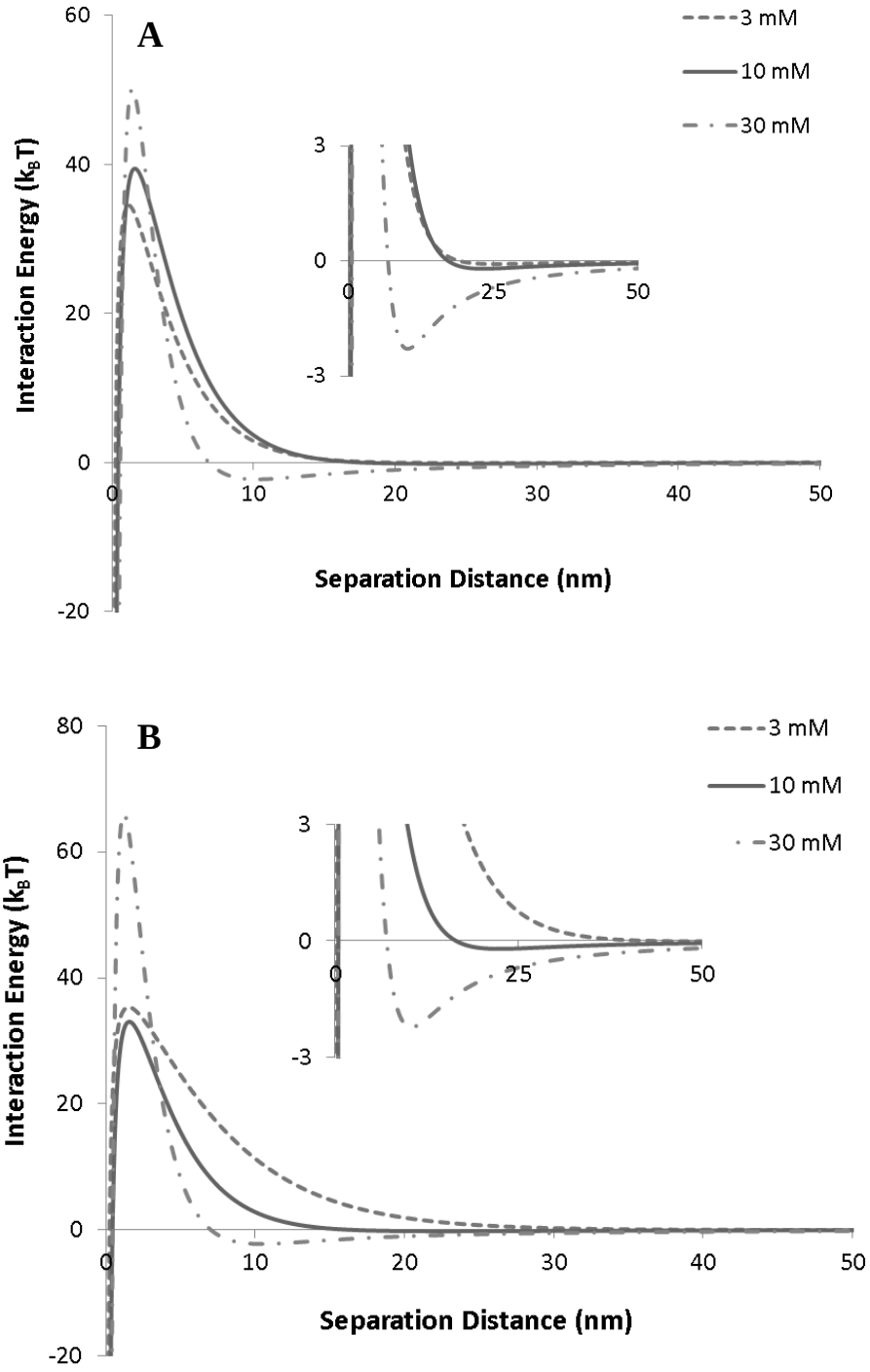

Figure 64. DLVO interaction energy profiles for nC60 interactions with (a) sand and (b) SiO_2 sensor in $CaCl_2$ solutions

Table 20. Height of primary energy barrier and depth of secondary energy minima (k_BT) for nC_{60} interactions with Ottawa sand or SiO_2 sensor in NaCl and $CaCl_2$

	Sand		Sensor	
Ionic Strength	Φ_{prim}	Φ_{sec}	Φ_{prim}	Φ_{sec}
3 mM NaCl	152.9	-0.01	250	-0.01
10 mM NaCl	108.2	-0.04	142	-0.04
30 mM NaCl	160.5	-0.39	277	-0.34
3 mM $CaCl_2$	35.4	-0.02	38.2	-0.07
10 mM $CaCl_2$	33.2	-0.21	43.3	-0.17
30 mM $CaCl_2$	66.1	-2.18	49.7	-2.1

The largest energy barriers were predicted at 30 mM in both electrolytes on the sand and sensor surfaces, indicative of the increased aggregation observed at higher ionic strengths (Table 19). These findings suggest that nC_{60} will be more mobile in both QCM and sand columns at 30 mM due to reduced diffusive transport of large aggregates to the collector surface and a net decrease in particle number concentration (Chen and Elimelech 2006; Liu et al. 2012). Neglecting potential contributions of aggregation, straining, and surface heterogeneity, the mobility of nC_{60} is expected to occur in the following order based on DLVO calculations: 30 mM > 3 mM > 10 mM.

A total of 8 nC_{60} experiments were conducted at different ionic strengths (NaCl or $CaCl_2$; 3, 10, 30 mM) and flow rates (1.0, 1.5, 2.0 mL/min).The following column experiments were performed by Dr. Yonggang Wang (Wang et al. 2008): 3 mM and 30 mM NaCl (1 mL/min) and 3 mM and 30 mM CaCl2 (1 mL/min). In columns conducted at different NaCl concentrations and 1 mL/min (7.6 m/d), the percentage of retained mass was observed to increase from 0.04 to 24.3 to 95.4 as

ionic strength was increased from 3 to 10 to 30 mM NaCl (Figure 65). A similar trend was observed in columns with $CaCl_2$ solutions (Figure 66). Retention profiles became increasingly hyper-exponential in shape as ionic strength was increased in both NaCl and $CaCl_2$. The nC_{60} suspensions aggregated considerably during injection at higher ionic strengths (e.g., from ca. 95 nm up to 225 nm and 800+ nm in 30 mM NaCl and $CaCl_2$, respectively). Increased compression of the electrical double layer surrounding particles and surfaces, as well as larger aggregate sizes, likely contributed to increased retention at higher ionic strengths. Physical straining may have also occurred, particularly at 30 mM $CaCl_2$, where the ratio of particle diameter to grain size is nearly equal to the reported threshold for straining (Xu et al., 2006). The modified filtration theory model was able to capture the shape of all effluent breakthrough curves, as well as retention profiles at lower ionic strengths. The model could not simulate the higher-than-expected retention at the inlet. Fitted model parameters (k_{att} *and* S_{max}) increased with increasing ionic strength in NaCl and $CaCl_2$ (Table 21).

In columns conducted at different flow rates (Figure 67), the percentage of nC_{60} mass retained in sand columns decreased from 95.4 to 55.6 to 38.1 as flow rate was increased from 1.0 to 1.5 to 2.0 mL/min. The fitted values of k_{att} and S_{max} were not particularly sensitive to flow rate (Table 21). The attachment rate was ca. 8 h^{-1} at the three tested flow rates, while S_{max} was ca. 4 µg/g at 1.0 and 1.5 mL/min and increased to 36 µg/g at 2.0 mL/min.

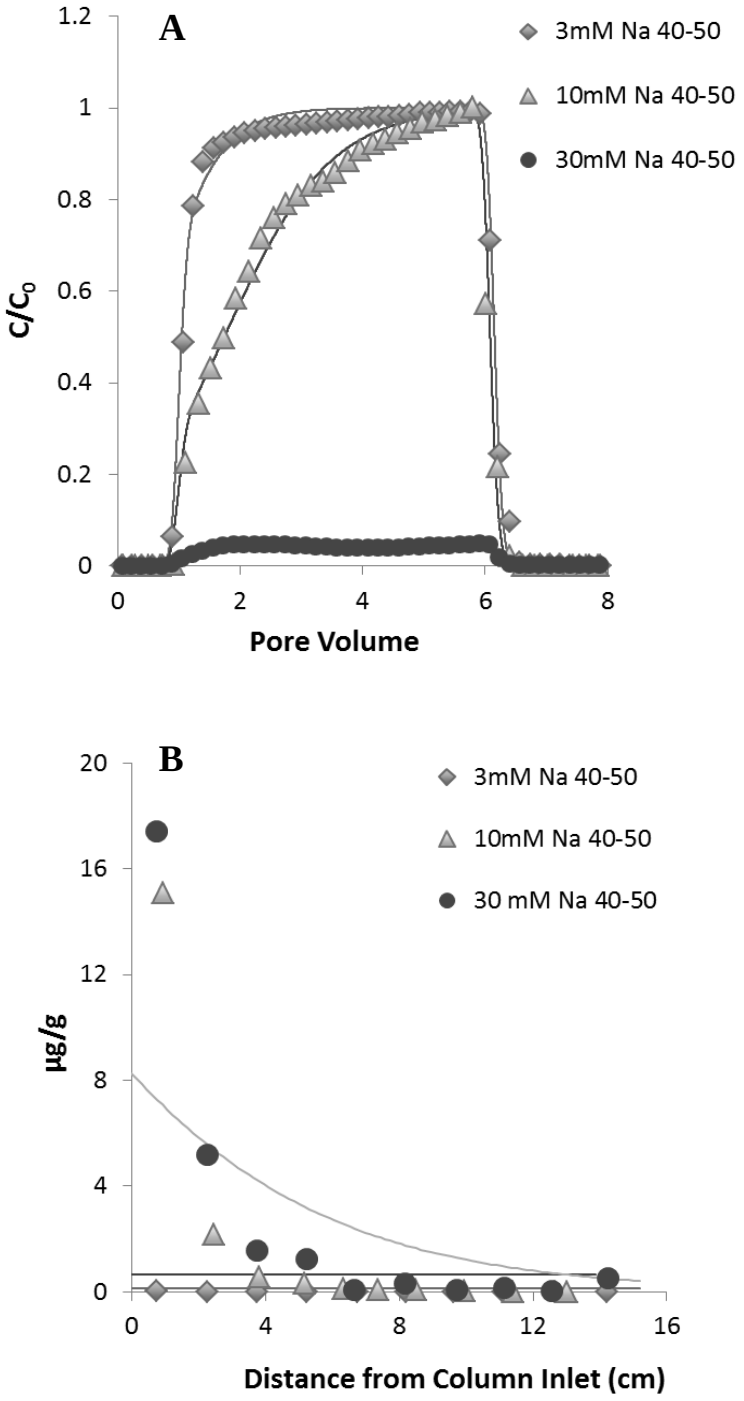

Figure 65. nC_{60} transport in washed 40-50 mesh Ottawa sand in NaCl at 1 mL/min (7.6 m/d). Modified filtration theory was fit to the data.

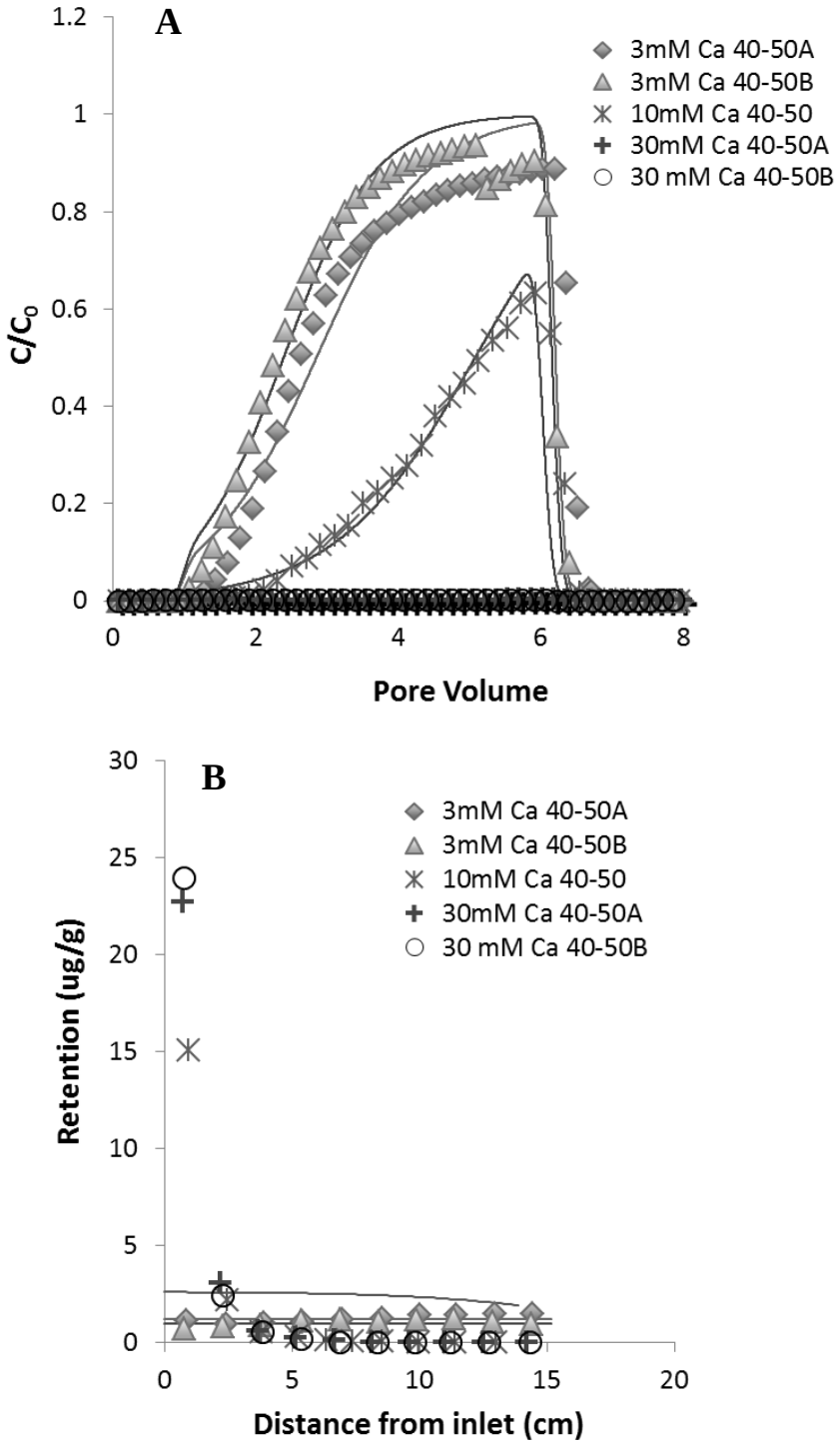

Figure 66. nC_{60} transport in washed 40-50 mesh Ottawa sand in $CaCl_2$ at 1 mL/min (7.6 m/d). Modified filtration theory was fit to the data.

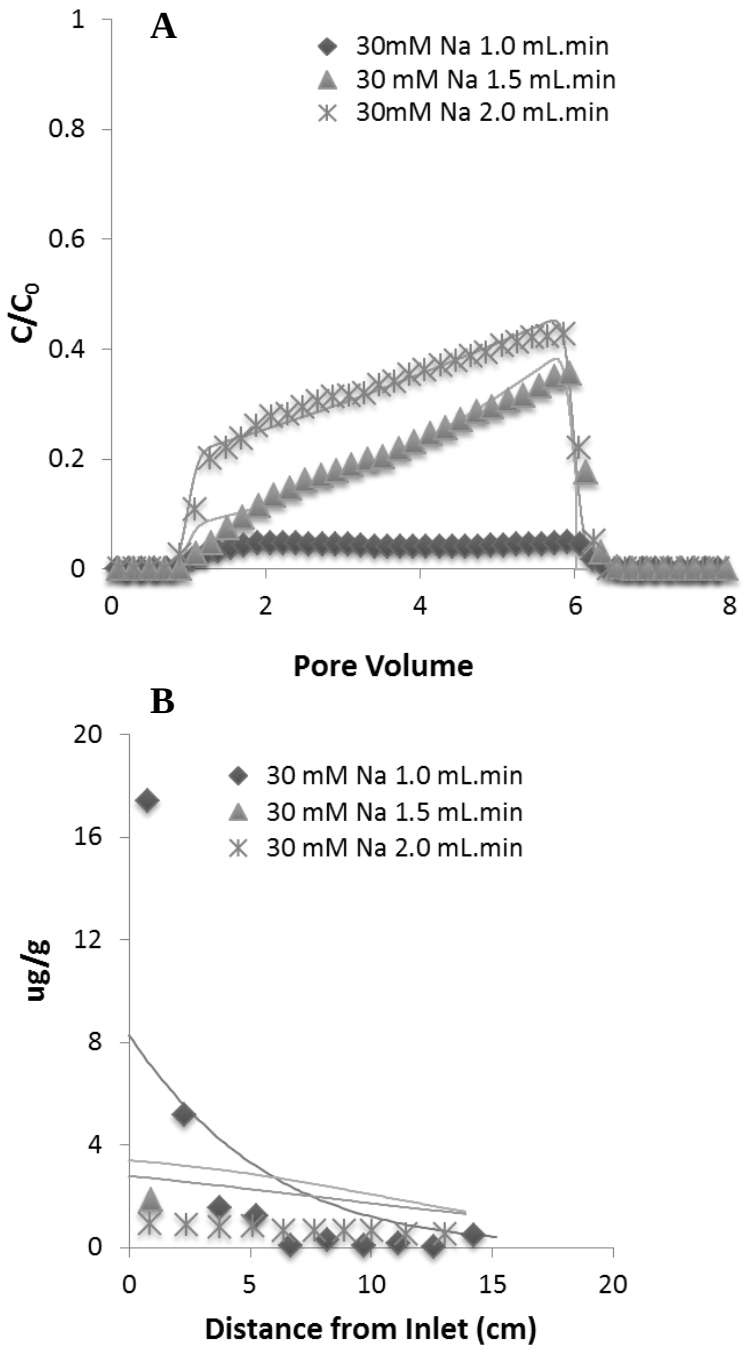

Figure 67. nC_{60} transport in washed 40-50 mesh Ottawa sand in 30 mM NaCl at 1.0, 1.5, and 2.0 mL/min (7.6, 11.8, 15.2 m/d). Modified filtration theory was fit to the data.

Table 21. Experimental and modeling parameters for nC_{60} column experiments in NaCl and $CaCl_2$

Ionic Strength	Velocity (m/d)	% Retained	% Mass Balance	k_{att} (1/h)	S_{max} (ug/g)
3.065 mM NaCl	7.6	0.04	98.4	0.77	0.12
10.065 mM NaCl	7.6	24.3	102.8	2.8	0.64
30.065 mM NaCl	7.6	95.4	99.9	7.29	36.38
30.065 mM NaCl	11.8	55.6	95.9	8.85	3.87
30.065 mM NaCl	15.2	38.1	94.6	7.17	3.99
3.065 mM $CaCl_2$	7.6	36.2	103.8	7.46	1.13
10.065 mM $CaCl_2$	7.6	72.3	99.5	10.06	2.62
30.065 mM $CaCl_2$	7.6	99.7	93.9	n/a	n/a

No deposition was measured on silica sensors in QCM under conditions identical to sand column experiments. Minimal deposition (0.03-0.04 Hz/min) was observed when ionic strength was increased to 100 mM NaCl or $CaCl_2$. The lack of nC_{60} deposition in QCM may be attributed to the highly repulsive interactions (large energy barriers) predicted for all tested conditions. In the one prior QCM study with nC_{60}, Chen and Elimelech (2006) observed increasing deposition as ionic strength was increased from 1 to 30 mM NaCl and from 0.1 to 0.5 mM $CaCl_2$. The mean diameter of primary nC_{60} was 50-60 nm in this study, nearly half the diameter of the nC_{60} used in the current study. Smaller particles have to overcome considerably lower energy barriers, which may have allowed for deposition on silica in the previous study. It is also likely that the presence of large aggregates at 10 mM and 30 mM hindered deposition in QCM. This is consistent with the enhanced transport of large aggregates reported in previous studies (Quevedo et al. 2014; Chen and Elimelech 2006) and with DLVO theory predictions.

Summary and Conclusions

The deposition behavior of nMag, nAg and nC_{60} were evaluated in a series of corresponding sand column and QCM-D experiments. This study presents the first QCM experiments to date conducted at linear velocities equivalent to those used in traditional column transport studies. All previous QCM-nanoparticle studies used flow rates in the range of 0.1-0.4 mL/min, which is equivalent to ca. 40-160 m/d, well above velocities realistically encountered in environmental or engineered porous media (e.g., water treatment filters). Current QCM experiments were conducted at flow rates of 0.02-0.04 mL/min (lowest feasible flow in the Q-Sense system), equivalent to approximately 7.5-15 m/d.

Deposition occurred with all three tested nanoparticles in sand columns, while only nMag deposited in QCM under equivalent conditions. Deposition rates obtained from QCM experiments with nMag were scaled by the specific surface area of the porous media and compared with fitted column attachment rates. QCM data was able to reasonably predict k_{att} in Ottawa sand columns with NaCl, but over-predicted k_{att} in sand columns with $CaCl_2$ and in glass bead columns. In the case of nAg, the observed lack of deposition is consistent with results from a previous QCM study with citrate-coated nAg, and may also be attributed to presence of repulsive conditions between nAg and collector surfaces under tested conditions. In current experiments with nMag and in previous QCM experiments, deposition generally occurred only under favorable conditions (no primary energy

barrier). The lack of nC_{60} deposition on silica was attributed to the presence of large aggregates and very high primary interaction energy barriers.

Discrepancies between nanoparticle deposition behavior in sand columns and QCM likely resulted from differences in surface charge, roughness, and heterogeneity, as well as the role of straining in porous media. Sensor surfaces which are more representative of the sand surfaces are currently being explored. In all tested electrolytes, the surface potential difference between the quartz sand and pure silica-coated sensor were 20-25 mV, suggesting that a sensor surface with a less negative charge may be more appropriate for evaluating nanoparticle deposition in porous media. Possible surface coatings (sold as prefabricated sensors by Q-Sense) include hydroxyapatitie, borosilicate glass, and iron/aluminum oxide. Deposition of a positive-charged salt (e.g., CaCl2) or positively charged polymer (e.g., poly-L-lysine, PLL) on the pure silica surface may provide an alternative method for reducing negative sensor charge. Streaming potential measurements can be used to determine the surface charge of these various coatings and applications relative to the quartz sands used in column experiments. Modifications to the roughness of sensors may also produce a more representative surface.

The surface roughness of the pure silica sensors is ca. 3 nm (atomic force microscopy measurements by Q-Sense), while the average roughness of Ottawa sand is approximately 100 nm (Larrahondo and Burns 2014). It may be possible to physically or chemically etch the smooth silica to introduce greater roughness. For example, potassium hydroxide, hydrofluoric acid, and nitric acid, as well as

laser techniques are used to etch silica used in semi-conductors (Buhler et al. 1997; Ding et al. 2002).

This research suggests that QCM-D experiments conducted with silica-coated sensors may be used to establish general trends for nanoparticle deposition in porous media as a function of solution chemistry. However, the lack of deposition in QCM-D observed with some nanomaterials poses a challenge in obtaining useful data. Sensor surfaces with more realistic charge and roughness characteristics should be evaluated to fully determine the applicability of QCM-D data to nanoparticle transport behavior in porous media.

CHAPTER 8: CONCLUSIONS AND RECOMMENDATIONS

The research presented herein focuses on the physical and chemical transformations of nanoparticles in aqueous environments and the influence of these transformations on fate and transport behavior in natural and engineered porous media.

Three publications were prepared based on this PhD research:

1. Mittelman, A.M., Lantagne, D.S., Pennell, K.D. Impact of water chemistry on silver dissolution and release in ceramic water filters. (Submitted to: *Environmental Science & Technology*)
2. Mittelman, A.M., Fortner, J.D., Pennell, K.D. Effects of UV light aging on silver nanoparticle transport and dissolution in water-saturated porous media. (Submitted to: *Environmental Science: Nano*)
3. Mittelman, A.M., Li, W., Becker, M.D., Fortner, J.D., Abriola, L.M., Pennell, K.D. A comparison of nanoparticle deposition behavior in sand columns and quartz crystal microbalance. (In preparation)

The key findings of this work are highlighted below.

UV Light Exposure and Nanoparticle Transport

i. Iron oxide (magnetite) nanoparticles exposed to UV light were 30-40% more strongly retained in water-saturated porous media compared with freshly prepared materials due to changes in particle size and surface

chemistry. These results suggest that metal oxide nanomaterials may be less mobile in the subsurface and water treatment filters following surface aging.

ii. Effluent breakthrough curves of fresh magnetite nanoparticles were asymmetrical in shape, suggesting a limited capacity for attachment in porous media, while breakthrough of aged nanoparticles displayed evidence of filter ripening (preferential deposition of aggregates onto already-deposited nanoparticles).

iii. UV light exposure caused oxidative surface aging of silver nanoparticles, resulting in up to 20-fold increases in particle size, 60-fold increases in dissolution, shifts in UV-vis spectra towards the red region, and 10-15 mV reductions in surface charge.

iv. UVB-aged silver nanoparticles were more prone to aggregation and dissolution in electrolyte solutions compared with UVA-aged particles, presumably due to the higher energy of shorter UVB wavelengths.

v. UV-aged silver nanoparticles were up to 50% more strongly retained in water-saturated Ottawa sand compared with freshly prepared particles and exhibited filter ripening behavior due to aggregation in the porous media.

vi. UV-aged silver nanoparticles were more prone to dissolution in sand columns, with Ag^{+} effluent concentrations as high as 1.2 mg/L. These results indicate that residues from aged nanomaterials may exhibit enhanced mobility following exposure to different aging scenarios, which may in turn increase the likelihood for more widespread contamination of groundwater resources.

i. Non-reactive tracer data and mercury porosimetry measurements indicated that ceramic filter disks contain heterogeneous pore structures with regions of immobile water capable of influencing solute transport

ii. Differences between total and dissolved silver release from filters were minimal (< 0.05 mg/L), indicating that the majority of silver eluted from the disks as Ag^{+}, rather than as nanoparticles (nAg)

iii. Silver release from ceramic disks was highly sensitive to changes in ionic strength, cation species, and pH, with release rates governed by competitive exchange of Ag^{+} for Na^{+}, Ca^{2+}, and Mg^{2+}, and H^{+}. Increasing influent ionic strength from 10 to 50 mM, decreasing pH from 7 to 5, and changing from a monovalent to divalent electrolyte resulted in effluent silver concentrations 5-10 times above international drinking water standards.

iv. When disks were painted with $AgNO_3$ or nAg on only the upper surface, silver release was reduced up to 10-fold compared with disks painted on both surfaces, indicating that the lower surface contributed the majority of the silver observed in the effluent

v. These data support the recommendation of a regular replacement schedule for filter element to ensure ongoing efficacy and a recommendation to not use the CWF in areas with acidic, high salinity, or high hardness water supplies.

Nanoparticle Deposition in QCM-D and Porous Media

i. Magnetite nanoparticles deposited in both QCM-D and sand columns under identical chemical and flow conditions. Rates obtained QCM-D experiments were scaled by the specific surface area available for deposition in porous media and provided fairly good predictions of fitted attachment rates derived from Ottawa sand columns.

ii. Although nC_{60} and silver nanoparticles readily deposited in sand columns, minimal deposition occurred on silica sensors in corresponding QCM-D experiments. Discrepancies in nanoparticle transport behavior between the two systems were attributed to differences in surface heterogeneity, flow geometry, and the contribution of physical straining in porous media.

iii. The development of QCM-D sensor surfaces which are more representative of porous media (e.g., quartz sand) with regards to surface charge and roughness may allow for a more accurate comparison of deposition behavior in QCM-D and sand column experiments.

Recommendations for Future Research

Based upon the experimental results described in Chapters 4-7, the following areas of research related to nanomaterial aging in natural and engineered porous media are recommended for future study.

Two separate studies with magnetite nanoparticles and silver nanoparticles conclusively showed that UV light aging can affect the transport, retention, and

dissolution of nanomaterials in water-saturated porous media. Although this research greatly expands upon our knowledge of the transport and retention of aged nanomaterials, it would be beneficial to evaluate transport behavior in a two-dimensional system, such as an aquifer cell. It is also important to consider heterogeneous porous media, including the presence of low-permeability lenses or soils with varying amounts of organic matter or metal oxides. Additionally, the impact of other surface aging mechanisms on nanoparticle fates and transport, such as biodegradation or reducing conditions, should be evaluated in future studies. Although this work centered on nanomaterial fate and transport in the subsurface, outcomes are also applicable to engineered porous media, particularly filters used in water and wastewater treatment. Further evaluation of the effects of nanomaterial surface transformations on nanomaterial transport in treatment systems is a natural extension of this research.

This research considerably expanded our knowledge regarding the impact of water quality on silver nanoparticle retention and dissolution in ceramic water filters. Future studies should consider the influence of additional water quality parameters, particularly natural organic matter and chlorine, and also include a wider range of filter recipes. Although the ceramic disk format allowed for less timely and higher-throughput experiments, similar silver release studies should also be conducted in full-sized filters to more closely mimic field conditions.

Results from complementary QCM-D and sand column experiments suggest that QCM-D data should be regarded with caution, as it may not be directly applicable to nanomaterial behavior in water-saturated porous media. Additional studies

which consider a wider range of nanoparticle types, chemical conditions, collector surfaces, and flow rates are required before QCM-D can be substituted for more intensive transport studies.

REFERENCES

Ahern, A. M.; Garrell, R. L. In situ photoreduced silver nitrate as a substrate for surface-enhanced raman spectroscopy. Anal. Chem. 1987, 2813–2816.

Arbab, A. S., Bashaw, L. A., Miller, B. R., Jordan, E. K., Lewis, B. K., Kalish, H., & Frank, J. A. (2003). Characterization of Biophysical and Metabolic Properties of Cells Labeled with Superparamagnetic Iron Oxide Nanoparticles and Transfection Agent for Cellular MR Imaging1. Radiology, 229(3), 838-846.

Auffan, M.; Pedeutour, M.; Rose, J.; Masion, A.; Ziarelli, F.; Borschneck, D.; Chaneac, C.; Botta, C.; Chaurand, P.; Labille, J.; et al. Structural degradation at the surface of a TiO2-based nanomaterial used in cosmetics. Environ. Sci. Technol. 2010, 44, 2689–2694.

Becker, M. D.; Wang, Y.; Pennell, K. D.; Abriola, L. M. A multi-constituent site blocking model for nanoparticle and stabilizing agent transport in porous media. Environ. Sci. Nano 2015.

Bergstrm, L. Hamaker constants of inorganic materials. Adv. Colloid Interface Sci. 1997, 70, 125–169.

Bhattacharjee, S., & Elimelech, M. (1997). Surface element integration: A novel technique for evaluation of DLVO interaction between a particle and a flat plate. Journal of colloid and interface science, 193(2), 273-285.

Bielefeldt, A. R., Kowalski, K., Schilling, C., Schreier, S., Kohler, A., & Summers, S. R. (2010). Removal of virus to protozoan sized particles in point-of-use ceramic water filters. Water research, 44(5), 1482–8.

Bielefeldt, A. R.; Kowalski, K.; Summers, R. S. Bacterial treatment effectiveness of point-of-use ceramic water filters. Water Res. 2009, 43, 3559–3565.

Bielefeldt, A. R.; Stewart, M. W.; Mansfield, E.; Summers, S.R.; Ryan, J. N. (2013). Effects of chlorine and other water quality parameters on the release of silver nanoparticles from a ceramic surface. Water Res. 47, 4032–4039.

Bloem, S.C., van Halem, D., Sampson, M.L., Huoy, L.S., Heijman, B. Silver impregnated ceramic pot filter: flow rate versus the removal efficiency of pathogens. In International Ceramic Pot Filter Workshop; 2009.

Bradford, S. A., Torkzaban, S., & Simunek, J. (2011). Modeling colloid transport and retention in saturated porous media under unfavorable attachment conditions. Water Resources Research, 47(10), n/a–n/a.

Bradford, S. A.; Torkzaban, S.; Walker, S. L. (2007). Coupling of physical and chemical mechanisms of colloid straining in saturated porous media. Water Res. 41, 3012–3024.

Brown, J., & Sobsey, M. D. (2007). Use of Ceramic water filters in Cambodia. Water and Sanitation Program, Cambodia Country Office.

Brown, J., Sobsey, M. D., & Loomis, D. (2008). Local drinking water filters reduce diarrheal disease in Cambodia: a randomized, controlled trial of the ceramic water purifier. Am J Trop Med Hyg, 79(3), 394-400.

Bühler, J., Steiner, F. P., & Baltes, H. (1997). Silicon dioxide sacrificial layer etching in surface micromachining. *Journal of Micromechanics and Microengineering*, *7*(1), R1.

Caron G, Suffet IH and Belton T. (1985). Effect of dissolved organic carbon on the environmental distribution of nonpolar organic compounds. Chemosphere 14, 993-1000.

Ceramics Manufacturing Working Group (CMWG) (2011). Best Practice Recommendations for Local Manufacturing of Ceramic Pot Filters for Household Water Treatment, Ed. 1. Atlanta, GA, USA: CDC.

Chen, G., Liu, X., & Su, C. (2011). Transport and retention of TiO2 rutile nanoparticles in saturated porous media under low-ionic-strength conditions: measurements and mechanisms. *Langmuir*, 27(9), 5393–402.

Chen, G.; Liu, X.; Su, C. (2012). Distinct effects of humic acid on transport and retention of TiO2 rutile nanoparticles in saturated sand columns. Environ. Sci. Technol. 2012, 46, 7142–7150.

Chen, K. L.; Elimelech, M. (2006). Aggregation and deposition kinetics of fullerene (C60) nanoparticles. *Langmuir* 117, 10994–11001.

Chen, M., Wang, L.-Y., Han, J.-T., Zhang, J.-Y., Li, Z.-Y., & Qian, D.-J. (2006). Preparation and study of polyacryamide-stabilized silver nanoparticles through a one-pot process. *J. Phys. Chem. B*, 110(23), 11224–31.

Cheng, Y.; Yin, L.; Lin, S.; Wiesner, M.; Bernhardt, E.; Liu, J. (2011). Toxicity reduction of polymer-stabilized silver nanoparticles by sunlight. *J. Phys. Chem. C* 115, 4425–4432.

Choi, O., Deng, K. K., Kim, N.-J., Ross, L., Surampalli, R. Y., & Hu, Z. (2008). The inhibitory effects of silver nanoparticles, silver ions, and silver chloride colloids on microbial growth. Water research, 42(12), 3066–74.

Chowdhury, I., Cwiertny, D. M., & Walker, S. L. (2012). Combined factors influencing the aggregation and deposition of nano-TiO2 in the presence of humic acid and bacteria. Environmental science & technology, 46(13), 6968–76.

Chowdhury, I.; Hong, Y.; Honda, R. J.; Walker, S. L. (2011). Mechanisms of TiO2 nanoparticle transport in porous media: role of solution chemistry, nanoparticle concentration, and flowrate. *J. Colloid Interface Sci.* 360, 548–555.

Coutris, C., Joner, E. J., & Oughton, D. H. (2012). Aging and soil organic matter content affect the fate of silver nanoparticles in soil. *Sci. Tot. Environ.* 420, 327–33.

Darby, J. L.; Lawler, D. F. Ripening in Depth Filtration : Effect of Particle Size on Removal and Head Loss. Environ. Sci. Technol. 1990, 24, 1069–1079.

Dasari, T. P., & Hwang, H. M. (2010). The effect of humic acids on the cytotoxicity of silver nanoparticles to a natural aquatic bacterial assemblage. Sci Tot Environ, 408(23), 5817-5823.

Derjaguin B. V. and Landau L. (1941) Theory of the stability of strongly charged lyophobic sols and the adhesion of strongly charged particles in solutions of electrolytes. Acta Physiochim. URSS 14, 633–662

Ding, X., Kawaguchi, Y., Niino, H., & Yabe, A. (2002). Laser-induced high-quality etching of fused silica using a novel aqueous medium. *Applied physics A, 75*(6), 641-645.

Di Palma, L., & Mecozzi, R. (2007). Heavy metals mobilization from harbour sediments using EDTA and citric acid as chelating agents. Journal of hazardous materials, 147(3), 768-775.

El Badawy, A. M.; Luxton, T. P.; Silva, R. G.; Scheckel, K. G.; Suidan, M. T.; Tolaymat, T. M. (2010). Impact of environmental conditions (pH, ionic strength, and electrolyte type) on the surface charge and aggregation of silver nanoparticles suspensions. *Environ. Sci. Technol.* 44, 1260–1266.

Elimelech, M, Gregory J, Jia X, William J (1995) Particle Deposition & Aggregation: Measurement, Modelling and Simulation. Butterworth-Heinemann.

Fatisson, J.; Domingos, R. F.; Wilkinson, K. J.; Tufenkji, N. (2009). Deposition of TiO2 nanoparticles onto silica measured using a quartz crystal microbalance with dissipation monitoring. *Langmuir* 25, 6062–6069.

French, RA., Jacobson, A. R., Kim, B., Isley, S. L., Penn, R. L., & Baveye, P. C. (2009). Influence of Ionic Strength, pH, and Cation Valence on Aggregation Kinetics of Titanium Dioxide Nanoparticles. Environmental Science & Technology, 43(5), 1354–1359.

Fritz, G., Scha, V., Willenbacher, N., & Wagner, N. J. (2002). Electrosteric Stabilization of Colloidal Dispersions. Society, (8), 6381–6390.

Fortner, J. D., Lyon, D. Y., Sayes, C. M., Boyd, A. M., Falkner, J. C., Hotze, E. M. & Hughes, J. B. (2005). C60 in water: nanocrystal formation and microbial response. *Environmental Science & Technology*, *39*(11), 4307-4316.

Gamerdinger, A. P.; Wagenet, R. J. (1989). Application of two-site/two-region models for studying simultaneous nonequilibrium transport and degradation of pesticides. *Soil Sci. Soc. Am. J.* 54, 957–963.

Gao, J., Powers, K., Wang, Y., Zhou, H., Roberts, S. M., Moudgil, B. M. & Barber, D. S. (2012). Influence of Suwannee River humic acid on particle properties and toxicity of silver nanoparticles. Chemosphere, 89(1), 96-101.

Garoma, T., & Gurol, M. D. (2004). Degradation of tert-butyl alcohol in dilute aqueous solution by an O3/UV process. *Environmental Science & Technology*,*38*(19), 5246-5252.

Godinez, I. G., & Darnault, C. J. (2011). Aggregation and transport of nano-TiO2 in saturated porous media: Effects of pH, surfactants and flow velocity. Water research, 45(2), 839-851.

Godinez, I. G.; Darnault, C. J. G.; Khodadoust, A. P.; Bogdan, D. (2013). Deposition and release kinetics of nano-TiO2 in saturated porous media: effects of solution ionic strength and surfactants. *Environ. Pollut.* 174, 106–113.

Gorham, J. M.; MacCuspie, R. I.; Klein, K. L.; Fairbrother, D. H.; Holbrook, R. D. (2012). UV-induced photochemical transformations of citrate-capped silver nanoparticle suspensions. *J. Nanoparticle Res.* 14, 1139.

Gunawan, C.; Teoh, W. Y.; Marquis, C. P.; Lifia, J.; Amal, R. (2009). Reversible antimicrobial photoswitching in nanosilver. *Small* 5, 341–344.

Gupta, A. K., & Gupta, M. (2005). Synthesis and surface engineering of iron oxide nanoparticles for biomedical applications. Biomaterials, 26(18), 3995-4021.

Guzman, K. A. D., Finnegan, M. P., & Banfield, J. F. (2006). Influence of surface potential on aggregation and transport of titania nanoparticles. Environmental science & technology, 40(24), 7688–93.

Hardman, R. (2006). A Toxicologic Review of Quantum Dots: Toxicity Depends on Physicochemical and Environmental Factors. Environmental Health Perspectives, 114(2), 165–172.

Henglein, A. (1998). Colloidal silver nanoparticles: photochemical preparation and interaction with O2, CCl4, and some other ions. *Anal. Chem*. 2, 444–450.

Hiemenz, P.; Rajagopalan, R. Principles of Colloid and Surface Chemistry; 3rd ed.; CRC Press, 1997.

Holt, K. B.; Bard, A. J. (2005) Interaction of silver(I) ions with the respiratory chain of Escherichia coli: an electrochemical and scanning electrochemical microscopy study of the antimicrobial mechanism of micromolar Ag+. *Biochemistry 44*, 13214–13223.

Honig, E. P., & Introduction, I. (1971). Effect of Hydrodynamic Interaction on the Coagulation Rate of Hydrophobic Colloids. Interface, 36(1).

Hou, W.; Jafvert, C. T. Photochemical transformation of aqueous 60 clusters in sunlight. Environ. Sci. Technol. 2009, 43, 362–367.

Hubaux, A.; Vos, G. (1970). Decision and detection limits for linear calibration curves. *Anal. Chem.* 42, 849–855.

Hunter, R. J. Zeta potential in colloid science; Academic Press: London, 1981.

Huynh, K. A., & Chen, K. L. (2011). Aggregation kinetics of citrate and polyvinylpyrrolidone coated silver nanoparticles in monovalent and divalent electrolyte solutions. Environmental science & technology, 45(13), 5564–71.

Israelachvili J. (1992) Intermolecular and Surface Forces. Academic Press, London

Jaisi, D. P., Saleh, N. B., Blake, R. E., & Elimelech, M. (2008). Transport of single-walled carbon nanotubes in porous media: filtration mechanisms and reversibility. Environmental science & technology, 42(22), 8317–23.

Jeng HA, Swanson J (2006) Toxicity of metal oxide nanoparticles in mammalian cells. J Environ Sci Health A 41:2699–2711

Jiang, X., Tong, M., Li, H., & Yang, K. (2010). Deposition kinetics of zinc oxide nanoparticles on natural organic matter coated silica surfaces. Journal of colloid and interface science, 350(2), 427-434.

Johnson, P. R., Sun, N., & Elimelech, M. (1996). Colloid Transport in Geochemically Heterogeneous Porous Media: Modeling and Measurements. Environmental Science & Technology, 30(11), 3284–3293.

Johnson, W. P., & Li, X. (2005). Comment on breakdown of colloid filtration theory: role of the secondary energy minimum and surface charge heterogeneities. *Langmuir* 21(23), 10895

Johnson, S. E., & Loeppert, R. H. (2006). Role of organic acids in phosphate mobilization from iron oxide. *Soil Science Society of America Journal*, *70*(1), 222-234.

Johnson, S. M., Peletz, R. L., & Murcott, S. (2008). Results from household ceramic filter evaluation in northern Ghana. In *33rd WEDC International Conference Accra, Ghana* (Vol. 463).

Joo, S. H., Al-Abed, S. R., & Luxton, T. (2009). Influence of carboxymethyl cellulose for the transport of titanium dioxide nanoparticles in clean silica and mineral-coated sands. Environmental science & technology, 43(13), 4954–9.

Kallman, E. N., Oyanedel-Craver, V.A, Smith, J.A. (2011). Ceramic Filters Impregnated with Silver Nanoparticles for Point-of-Use Water Treatment in Rural Guatemala. Glass, (June), 407–415.

Kasel, D.; Bradford, S. A; Šimůnek, J.; Heggen, M.; Vereecken, H.; Klumpp, E. (2013).Transport and retention of multi-walled carbon nanotubes in saturated porous media: effects of input concentration and grain size. Water Res. 47, 933–944.

Kaya, A., & Yukselen, Y. (2005). Zeta potential of soils with surfactants and its relevance to electrokinetic remediation. Journal of hazardous materials, 120(1-3), 119–26.

Keller, A. a, Wang, H., Zhou, D., Lenihan, H. S., Cherr, G., Cardinale, B. J., Miller, R., et al. (2010). Stability and aggregation of metal oxide nanoparticles in natural aqueous matrices. Environmental science & technology, 44(6), 1962–7.

Kim, H.-J., Phenrat, T., Tilton, R. D., & Lowry, G. V. (2009). Fe0 nanoparticles remain mobile in porous media after aging due to slow desorption of polymeric surface modifiers. Environmental science & technology, 43(10), 3824–30.

Kim, S., Choi, J. E., Choi, J., Chung, K.-H., Park, K., Yi, J., & Ryu, D.-Y. (2009). Oxidative stress-dependent toxicity of silver nanoparticles in human hepatoma cells. *Toxicology in vitro* 23(6), 1076–84.

Kocbek, P., Teskač, K., Kreft, M. E. and Kristl, J. (2010), Toxicological Aspects of Long-Term Treatment of Keratinocytes with ZnO and TiO_2 Nanoparticles. Small, 6: 1908–1917.

Kühn, K. P., Chaberny, I. F., Massholder, K., Stickler, M., Benz, V. W., Sonntag, H. G., & Erdinger, L. (2003). Disinfection of surfaces by photocatalytic oxidation with titanium dioxide and UVA light. Chemosphere, 53(1), 71-77.

Labille, J., Feng, J., Botta, C., Borschneck, D., Sammut, M., Cabie, M., Auffan, M., et al. (2010). Aging of TiO(2) nanocomposites used in sunscreen. Dispersion and fate of the degradation products in aqueous environment. *Environ. Pol.* 158(12), 3482–9.

Lantagne, D. S. (2001). Investigation of the potters for peace colloidal silver impregnated ceramic filter. Report 2: Field Investigations. Alethia Environmental.

Lantagne, D. S. (2001). Investigation of the Potters for Peace Colloidal Silver Impregnated Ceramic Filter Report 1: Intrinsic Effectiveness. Alethia Environmental.

Larrahondo, J. M., & Burns, S. E. (2013). Laboratory-Prepared Iron Oxide Coatings on Sands: Surface Characterization and Strength Parameters. *Journal of Geotechnical and Geoenvironmental Engineering*, *140*(4).

Leaist DG (1991) Coupled tracer diffusion coefficients of solubilizates in ionic micelle solutions from liquid chromatography. Journal of Solution Chemistry 20:175-186.

Lecoanet, H. F., Bottero, J.-Y., & Wiesner, M. R. (2004). Laboratory assessment of the mobility of nanomaterials in porous media. Environmental science & technology, 38(19), 5164–9.

Lee, J.; Cho, M. I. N.; Fortner, J. D.; Hughes, J. B. (2009). Transformation of aggregated C60 in the aqueous phase by UV irradiation. Environ. Sci. Technol. 43, 4878–4883.

Lee, J.; Fortner, J. D.; Kim, J. (2007). Photochemical production of reactive oxygen species by C60 in the aqueous phase during UV irradiation. Environ. Sci. Technol. 41, 2529–2535.

Lee, J.; Ji, K.; Kim, J.; Park, C.; Lim, K. H.; Yoon, T. H.; Choi, K. Acute toxicity of two CdSe/ZnSe quantum dots with different surface coating in daphnia magna under various light conditions. Environ. Toxicol. 2009, 593–600.

Lewinski, N., Colvin, V., & Drezek, R. (2008). Cytotoxicity of nanoparticles. Small, 4(1), 26-49.

Li, W.-R.; Xie, X.-B.; Shi, Q.-S.; Zeng, H.-Y.; Ou-Yang, Y.-S.; Chen, Y.-B. (2010). Antibacterial activity and mechanism of silver nanoparticles on Escherichia coli. Appl. Microbiol. Biotechnol. 85, 1115–1122.

Li, X., Lenhart, J. J., & Walker, H. W. (2010). Dissolution-accompanied aggregation kinetics of silver nanoparticles. *Langmuir* 26(22), 16690–8.

Li, X., Lenhart, J. J., & Walker, H. W. (2012). Aggregation kinetics and dissolution of coated silver nanoparticles. *Langmuir* 28(2), 1095–104.

Li, X.; Lenhart, J. J. (2012). Aggregation and dissolution of silver nanoparticles in natural surface water. Environ. Sci. Technol. 46, 5378–5386.

Li, X.; Lin, C.-L.; Miller, J. D.; Johnson, W. P. Role of grain-to-grain contacts on profiles of retained colloids in porous media in the presence of an energy barrier to deposition. Environ. Sci. Technol. 2006, 40, 3769–3774.

Li, Y., Wang, Y., Pennell, K. D., & Abriola, L. M. (2008). Investigation of the transport and deposition of fullerene (C60) nanoparticles in quartz sands under varying flow conditions. Environmental science & technology, 42(19), 7174-7180.

Li, Z., Sahle-Demessie, E., Hassan, A. A., & Sorial, G. A. (2011). Transport and deposition of CeO2 nanoparticles in water-saturated porous media. Water research, 45(15), 4409–18.

Liang, Y.; Bradford, S. A; Simunek, J.; Vereecken, H.; Klumpp, E. Sensitivity of the transport and retention of stabilized silver nanoparticles to physicochemical factors. Water Res. 2013, 47, 2572–2582.

Lin, D., Tian, X., Wu, F., & Xing, B. (2010). Fate and Transport of Engineered Nanomaterials in the Environment. Journal of Environment Quality, 39(6), 1896.

Liu, J., & Hurt, R. H. (2010). Ion release kinetics and particle persistence in aqueous nano-silver colloids. Environmental science & technology, 44(6), 2169-2175.

Liu, X.; Chen, G.; Su, C. Effects of material properties on sedimentation and aggregation of titanium dioxide nanoparticles of anatase and rutile in the aqueous phase. J. Colloid Interface Sci. 2011, 363, 84–91.

Liu, X.; Chen, G.; Su, C. Influence of Collector Surface Composition and Water Chemistry on the Deposition of Cerium Dioxide Nanoparticles: QCM-D and Column Experiment Approaches. 2012.

Liufu, S., Xiao, H., & Li, Y. (2005). Adsorption of poly(acrylic acid) onto the surface of titanium dioxide and the colloidal stability of aqueous suspension. Journal of colloid and interface science, 281(1), 155–63.

Lok, C.; Ho, C.; Chen, R.; He, Q.; Yu, W.; Sun, H.; Tam, P. K.; Chiu, J.; Che, C. Proteomic analysis of the mode of antibacterial action of silver. J. Proteome Res. 2006, 916–924.

Lomer, M. C. E., Thompson, R. P. H., Commisso, J., Keen, C. L., & Powell, J. J. (2000). Determination of titanium dioxide in foods using inductively coupled plasma optical emission spectrometry. The Analyst, 125(12), 2339–2343.

Long, T. C., Saleh, N., Tilton, R. D., & Gregory, V. (2006). Titanium Dioxide (P25) Produces Reactive Oxygen Species in Implications for Nanoparticle, 40(14).

Lu, W., Senapati, D., Wang, S., Tovmachenko, O., Singh, A. K., Yu, H., & Ray, P. C. (2010). Effect of surface coating on the toxicity of silver nanomaterials on human skin keratinocytes. Chemical Physics Letters, 487(1-3), 92–96.

Lu, X.; Rycenga, M.; Skrabalak, S. E.; Wiley, B.; Xia, Y. Chemical synthesis of novel plasmonic nanoparticles. Annu. Rev. Phys. Chem. 2009, 60, 167–192.

Lux Research. (2014). Nanotechnology Update: Corporations Up Their Spending as Revenues for Nano-enabled Products Increase. http://portal.luxresearchinc.com/

Mahendra, S., Zhu, H., Colvin, V. L., & Alvarez, P. J. (2008). Quantum Dot Weathering Results in Microbial Toxicity Quantum Dot Weathering Results in Microbial Toxicity, 42(November), 9424–9430.

Maillard, M.; Huang, P.; Brus, L. Silver nanodisk growth by surface plasmon enhanced photoreduction of adsorbed [Ag +]. Nano Lett. 2003, 3, 1611–1615.

McGown DNL, Parfitt GD. (1967). Improved theoretical calculation of the stability ratio for colloidal systems. J. Phys. Chem 71(2):449-50

Metz, K. M., Mangham, A. N., Bierman, M. J., Jin, S., Hamers, R. J., & Pedersen, J. a. (2009). Engineered nanomaterial transformation under oxidative environmental conditions: development of an in vitro biomimetic assay. Environmental science & technology, 43(5), 1598–604.

Mittelman, A. M.; Taghavy, A.; Wang, Y.; Abriola, L. M.; Pennell, K. D. (2013). Influence of dissolved oxygen on silver nanoparticle mobility and dissolution in water-saturated quartz sand. J. Nanoparticle Res. 2013, 15, 1765.

Morones-Ramirez, J. R., Winkler, J. A., Spina, C. S., & Collins, J. J. (2013). Silver Enhances Antibiotic Activity Against Gram-Negative Bacteria. Science Translational Medicine, 5(190).

Mudunkotuwa, I. a, Pettibone, J. M., & Grassian, V. H. (2012). Environmental implications of nanoparticle aging in the processing and fate of copper-based nanomaterials. Environmental science & technology, 46(13), 7001–10.

Mueller, N. C., & Nowack, B. (2008). Exposure modeling of engineered nanoparticles in the environment. Environmental science & technology, 42(12), 4447–53.

Mulvaney, P., Linnert, T., & Henglein, A. (1991). Surface Chemistry of Colloidal Silver in Aqueous Solution : Observations on, 7843–7846.

Navarro, E., Piccapietra, F., Wagner, B., Marconi, F., Kaegi, R., Odzak, N., Sigg, L., et al. (2008). Toxicity of Silver Nanoparticles to Chlamydomonas reinhardtii. Environmental Science & Technology, 42(23), 8959–8964.

Ninham, B. W. (1999). On progress in forces since the DLVO theory. Advances in Colloid and Interface Science, 83, 1–17.

Oyanedel-Craver, V. A, & Smith, J. A. (2008). Sustainable colloidal-silver-impregnated ceramic filter for point-of-use water treatment. Environmental science & technology, 42(3), 927–33.

Pennell, K. D.; Rhue, R. D.; Harris, W. G. (1991). The effects of heat treatments on the total charge and exchangeable cations of Ca-, Na-, and Li- saturated kaolinite. Clays Clay Miner. 39, 306–315.

Phenrat, T., Saleh, N., Sirk, K., Kim, H. J., Tilton, R. D., & Lowry, G. V. (2008). Stabilization of aqueous nanoscale zerovalent iron dispersions by anionic polyelectrolytes: adsorbed anionic polyelectrolyte layer properties and their effect on aggregation and sedimentation. Journal of Nanoparticle Research,10(5), 795-814.

Phenrat, T., Long, T. C., Lowry, G. V., & Veronesi, B. (2009a). Partial Oxidation ("Aging") and Surface Modification Decrease the Toxicity of Nanosized Zerovalent Iron. Environmental Science & Technology, 43(1), 195–200.

Phenrat, T.; Kim, H.-J.; Fagerlund, F.; Illangasekare, T.; Tilton, R. D.; Lowry, G. V. (2009b). Particle size distribution, concentration, and magnetic attraction affect transport of polymer-modified Fe(0) nanoparticles in sand columns. Environ. Sci. Technol. 43, 5079–5085.

Pignatello, J. J., Oliveros, E., & MacKay, A. (2006). Advanced Oxidation Processes for Organic Contaminant Destruction Based on the Fenton Reaction and Related Chemistry. Environmental Science and Technology, 36(1), 1–84.

QSense. (2013). QCM-D Technology. http://www.q-sense.com/qcm-d-technology

Quevedo, I. R.; Olsson, A. L. J.; Clark, R. J.; Veinot, J. G. C.; Tufenkji, N. (2014). Interpreting Deposition Behavior of Polydisperse Surface-Modified Nanoparticles Using QCM-D and Sand-Packed Columns. Environ. Eng. Sci. 31, 326–337.

Rayner, J. (2009). Current Practices in Manufacturing of Ceramic Pot Filters for Water Treatment. Unpublished Thesis, Loughborough University.

Rayner, J., Skinner, B., Lantagne, D. (2013a) Current practices in manufacturing locally-made ceramic pot filters for water treatment in developing countries. J. Water, Sanit. Hyg. Dev. 3.

Rayner, J., Zhang, H., Schubert, J., Lennon, P., Lantagne, D., & Oyanedel-craver, V. (2013b). Laboratory Investigation into the Effect of Silver Application on the Bacterial Removal Efficacy of Filter Material for Use on Locally Produced Ceramic Water Filters for Household Drinking Water Treatment.

Reinsch, B. C.; Forsberg, B.; Penn, R. L.; Kim, C. S.; Lowry, G. V. Chemical transformations during aging of zerovalent iron nanoparticles in the presence of common groundwater dissolved constituents. Environ. Sci. Technol. 2010, 44, 3455–3461.

Ren, D.; Smith, J. A. (2013). Proteinate-capped silver nanoparticle transport in water-saturated sand. J. Environ. Eng. 139, 781–787.

Sahoo, S. K., & Labhasetwar, V. (2003). Nanotech approaches to drug delivery and imaging. Drug discovery today, 8(24), 1112-1120.

Saleh, N. B., Pfefferle, L. D., & Elimelech, M. (2008). Aggregation kinetics of multiwalled carbon nanotubes in aquatic systems: measurements and environmental implications. Environmental science & technology, 42(21), 7963–9.

Sarathy, V.; Tratnyek, P. G.; Nurmi, J. T.; Baer, D. R.; Amonette, J. E.; Chun, C. L.; Penn, R. L.; Reardon, E. J. (2013). Aging of Iron Nanoparticles in Aqueous Solution: Effects on Structure and Reactivity. J. Phys. Chem. C 112, 2286–2293.

Sauerbrey, G. Z. (1959). Use of quartz vibration for weighing thin films on a microbalance. *J. Physik, 155*, 206-212.

Scheckel, K. G., Luxton, T. P., El Badawy, A. M., Impellitteri, C. a, & Tolaymat, T. M. (2010). Synchrotron speciation of silver and zinc oxide nanoparticles aged in a kaolin suspension. Environmental science & technology, 44(4), 1307–12.

Schmidt, M., Masson, a., & Bréchignac, C. (2003). Oxygen and Silver Clusters: Transition from Chemisorption to Oxidation. Physical Review Letters, 91(24), 1–4.

Sharama MM, Kuo JF, Yen TF (1986). Further investigation of the surface charge properties of oxide surfaces in oil-bearing sands and sandstones. J Colloid Interf Sci 115:9-15.

Solovitch, N., Labille, J., Rose, J., Chaurand, P., Borschneck, D., Wiesner, M. R., & Bottero, J.-Y. (2010). Concurrent aggregation and deposition of TiO2 nanoparticles in a sandy porous media. Environmental science & technology, 44(13), 4897–902.

Song, L.; Johnson, P. R.; Elimelech, M. (1994). Kinetics of colloid deposition onto heterogeneously charged surfaces in porous media. Environ. Sci. Technol. 28, 1164–1171.

Song, W., Zhang, J., Guo, J., Zhang, J., Ding, F., Li, L., & Sun, Z. (2010). Role of the dissolved zinc ion and reactive oxygen species in cytotoxicity of ZnO nanoparticles. Toxicology letters, 199(3), 389–97.

Taghavy, A.; Mittelman, A.; Wang, Y.; Pennell, K. D.; Abriola, L. M. (2013). Mathematical Modeling of the Transport and Dissolution of Citrate- Stabilized Silver Nanoparticles in Porous Media. Environ. Sci. Technol. 47, 8499–8507.

Tang, Z.; Kotov, N. A.; Giersig, M. (2002). Spontaneous organization of single CdTe nanoparticles into luminescent nanowires. Science 297, 237–240.

Taylor, R. K. Cation exchange in clays and mudrocks by methylene blue. J. Chem. Tech. Biotechnol. 1985, 35, 195–207.

Thio, B. J. R., Zhou, D., & Keller, A. A. (2011). Influence of natural organic matter on the aggregation and deposition of titanium dioxide nanoparticles. Journal of hazardous materials, 189(1-2), 556–63.

Thio, B. J. R.; Montes, M. O.; Mahmoud, M. A; Lee, D.-W.; Zhou, D.; Keller, A. (2012). Mobility of capped silver nanoparticles under environmentally relevant conditions. *Environ. Sci. Technol. 46*, 6985–6991.

Tian, Y., Gao, B., Silvera-Batista, C., & Ziegler, K. J. (2010). Transport of engineered nanoparticles in saturated porous media. Journal of Nanoparticle Research, 12(7), 2371–2380.

Tolaymat, T. M.; El Badawy, A. M.; Genaidy, A.; Scheckel, K. G.; Luxton, T. P.; Suidan, M. (2010). An evidence-based environmental perspective of manufactured silver nanoparticle in syntheses and applications: a systematic review and critical appraisal of peer-reviewed scientific papers. Sci. Total Environ. 408, 999–1006.

Tong, M.; Johnson, W. P. (2006). Excess colloid retention in porous media as a function of colloid size, fluid velocity, and grain angularity. Environ. Sci. Technol. 40, 7725–7731.

Toride, N., Leij, F. J., & Van Genuchten, M. T. (1995). The CXTFIT Code for Estimating Transport Parameters from Laboratory Or Filed Tracer Experiments. Riverside: US Salinity Laboratory.

Torkzaban, S., Kim, Y., Mulvihill, M., Wan, J., & Tokunaga, T. K. (2010). Transport and deposition of functionalized CdTe nanoparticles in saturated porous media. Journal of contaminant hydrology, 118(3-4), 208–17.

US EPA (2014). Current Drinking Water Regulations http://water.epa.gov/lawsregs/rulesregs/sdwa/currentregulations.cfm#two

US EPA (2013). Nanotechnology and Nanomaterials Research. http://www.epa.gov/nanoscience/

Van Genuchten, M. T.; Wagenet, R. (1989). Two-site/two-region models for pesticide transport and degradation: theoretical development and analytical solutions. Soil Sci. Soc. Am. J. 53, 1303–1310.

Van Halem, D.; van der Laan, H.; Heijamn, S. G. H.; van Dijk, J. C.; Amy, G. L. (2009). Assessing the sustainability of the silver-impregnated ceramic pot filter for low-cost household drinking water treatment. Phys. Chem. Earth, Parts A/B/C 34, 36–42.

Verwey E. J. W. and Overbeek J. T. G. (1948) Theory of the Stability of Lyophobic Colloids. Elsevier, Amsterdam

Virkutyte, J., Al-Abed, S. R., & Dionysiou, D. D. (2012). Depletion of the protective aluminum hydroxide coating in TiO2-based sunscreens by swimming pool water ingredients. Chemical Engineering Journal, 191, 95–103.

Voinov, M. A., Sosa Pagán, J. O., Morrison, E., Smirnova, T. I., & Smirnov, A. I. (2011). Surface-mediated production of hydroxyl radicals as a mechanism of iron oxide nanoparticle biotoxicity. Journal of the American Chemical Society, 133(1), 35–41.

Wang, Y., Li, Y., Fortner, J. D., Hughes, J. B., Abriola, L. M., & Pennell, K. D. (2008). Transport and retention of nanoscale C60 aggregates in water-saturated porous media. Environmental science & technology, 42(10), 3588–94.

Wang, Y., Li, Y., Kim, H., Walker, S. L., Abriola, L. M., & Pennell, K. D. (2010). Transport and Retention of Fullerene Nanoparticles in Natural Soils. Journal of Environment Quality, 39(6), 1925.

Wang, L.; Fortner, J. D.; Hou, L.; Zhang, C.; Kan, A. T.; Tomson, M. B.; Chen, W. (2013). Contaminant-mobilizing capability of fullerene nanoparticles (nC60): Effect of solvent-exchange process in nC60 formation. *Environ. Toxicol. Chem. 32*, 329–336.

WHO & UNICEF. Progress on sanitation and drinking-water 2013 update: Joint Monitoring Programme for Water Supply and Sanitation. http://www.who.int/water_sanitation_health/publications/2013/jmp_report/en/index.html

WHO (1997) Guidelines for drinking-water quality, 2nd Edition: Volume 3; Surveillance and control of community supplies: Geneva, Switzerland.

WHO (2011). Evaluating household water treatment options: health-based targets and microbiological performance specifications. http://whqlibdoc.who.int/publications/2011/9789241548229_eng.pdf

WHO (2013a). 10 Facts on Sanitation. http://www.who.int/features/factfiles/sanitation/facts/en/index9.html

WHO (2013b). Water Resources: Water Sanitation and Health. http://www.who.int/water_sanitation_health/resources/en/

WHO (2013c). Water supply, sanitation and hygiene development. http://www.who.int/water_sanitation_health/hygiene/en/

WHO and UNICEF (2013). Progress on sanitation and drinking-water 2013 update: Joint Monitoring Programme for Water Supply and Sanitation. http://www.who.int/water_sanitation_health/publications/2013/jmp_report/en/index.html

Xia, T., Kovochich, M., Liong, M., Mädler, L., Gilbert, B., Shi, H., Yeh, J. I., et al. (2008). Comparison of the mechanism of toxicity of zinc oxide and cerium oxide nanoparticles based on dissolution and oxidative stress properties. ACS nano, 2(10), 2121–34.

Yang, X., Gondikas, A. P., Marinakos, S. M., Auffan, M., Liu, J., Hsu-Kim, H., & Meyer, J. N. (2011). Mechanism of silver nanoparticle toxicity is dependent on dissolved silver and surface coating in Caenorhabditis elegans. *Environmental science & technology*, *46*(2), 1119-1127.

Yao, K. M., Habibian, M. T., & O'Melia, C. R. (1971). Water and waste water filtration. Concepts and applications. Environmental Science & Technology,5(11), 1105-1112.

Zhang, H., Lv, X., Li, Y., Wang, Y., & Li, J. (2009). P25-graphene composite as a high performance photocatalyst. ACS nano, 4(1), 380-386.

Zhang, H., Smith, J. A., & Oyanedel-Craver, V. (2012). The effect of natural water conditions on the anti-bacterial performance and stability of silver nanoparticles capped with different polymers. Water research, 46(3), 691-699.

Zhang, H.; Oyanedel-Craver, V. A. (2012). Evaluation of the disinfectant performance of silver nanoparticles in different water chemistry conditions. J. Environ. Eng. \ 138, 58–66.

Zhang, Wen, Yao, Y., Sullivan, N., & Chen, Y. (2011). Modeling the primary size effects of citrate-coated silver nanoparticles on their ion release kinetics. Environmental science & technology, 45(10), 4422–8.

Zhang, W-X. (2003). Nanoscale iron particles for environmental remediation : An overview. J. Nano. Res. 5: 323–332

Zhang, Y., Chen, Y., Westerhoff, P., & Crittenden, J. (2009). Impact of natural organic matter and divalent cations on the stability of aqueous nanoparticles. Water research, 43(17), 4249–57.

Zhang, Y., Chen, Y., Westerhoff, P., Hristovski, K., & Crittenden, J. C. (2008). Stability of commercial metal oxide nanoparticles in water. Water research, 42(8-9), 2204–12.